Jet behaviour in longitudinal deepening shallow flows

A case study to the Eastern Scheldt storm surge barrier

B.J. van de Zande

September 2018

Delft University of Technology

TU Delft

Jet behaviour in longitudinal deepening shallow flows

A case study to the Eastern Scheldt storm surge barrier

by

B.J. van de Zande

to obtain the degree of Master of Science

at the Delft University of Technology,

to be defended publicly on Wednesday September 12, 2018 at 9:00 AM.

Student number:	4160207	
Project duration:	November, 2017 – September, 2018	
Thesis committee:	Prof. dr. ir. W.S.J. Uijttewaal,	TU Delft
	Dr. ir. R.J. Labeur,	TU Delft
	Dr. ir. C.J. Sloff,	TU Delft and Deltares
	Ir. Y.B. Broekema,	TU Delft

An electronic version of this thesis is available at `http://repository.tudelft.nl/`.

Cover image: Quantitative measurements of the surface flow by means of particle image velocimetry
Source: Photograph taken by Valerio Vincenzo ©

TU Delft Delft University of Technology

Preface

This thesis is submitted as final part of the Master study Hydraulic Engineering at Delft University of Technology. The research focusses on jet behaviour in longitudinal deepening shallow flows and includes a case study to the scour development near the Eastern Scheldt storm surge barrier. The research was carried out at the faculty of Civil Engineering and Geosciences and its Fluid Mechanics Laboratory.

First of all, I would like to thank the members of my graduation committee prof. dr. ir. W.S.J. Uijttewaal, dr. ir. R.J. Labeur and dr. ir. C.J. Sloff for their guidance and advice during the progress meetings. Our discussions have given me new insights that improved the quality of my research. Furthermore, I especially want to thank Yorick Broekema for answering all my questions and his help during the last months of my studies.

In addition, I would like to thank the staff of the Fluid Mechanics Laboratory Sander de Vree, Jaap van Duin, Arno Doorn, Rob van Dijk and Frank Kalkman for their technical support during the laboratory experiments. Without their help it would not have been possible to set up the experiment.

Finally, I would like to thank my parents, brother, sister, Lysanne and friends for their unconditional support and distraction when I needed it the most.

B.J. van de Zande
Delft, September 2018

Summary

In the proximity of the Eastern Scheldt storm surge barrier (ES-SSB), one of the largest hydraulic structures of the Dutch Delta Works, scour holes have developed that potentially threaten the stability of the structure. Although, these scour holes were anticipated in the design phase recent bathymetry measurements show that they are growing deeper than initially predicted. Uncertainties in the predictions of the equilibrium dimensions partially arise from the presence, thickness and erodibility of clay layers, but first and foremost from a lack of understanding of the flow conditions in the vicinity of the scour holes. High flow velocities are still observed near the bed in the scour holes, that can be associated with high bed shear stresses. This implies that an equilibrium state has not yet been reached and that the scour holes still become deeper. The presence of these high flow velocities is not fully understood, making predictions on the development of the scour holes and mitigation strategies difficult. As a result, the risk of geotechnical instabilities increases, which may potentially endanger the stability of the ES-SSB.

In literature, empirical equations have been suggested that estimate the final dimensions of scour holes for specific configurations. These empirical equations often include velocity scales, but do not account for all hydrodynamic processes in a scour hole. Furthermore, studies to scour predominantly considered a two-dimensional vertical situation in which the flow velocity is assumed uniform in the lateral direction. Field observations near the ES-SSB show that large velocity differences are present along the width of the barrier. The horizontal length scales of the flow phenomena are much larger than the vertical length scales, so the flow can be classified as a shallow flow. Therefore, a two-dimensional vertical framework is not satisfactory and a more suitable approach might be to consider a two-dimensional horizontal situation to describe the flow field near the ES-SSB.

The objective of this master thesis is to obtain more fundamental understanding of the flow patterns and turbulence structure in the vicinity of tidal barriers, such as the Eastern Scheldt storm surge barrier, and how these may contribute to ongoing scour. In this thesis, we experimentally investigate the development of a shallow jet that experiences a streamwise increase in depth, with and without the effect of grid turbulence. The aim of this thesis is to obtain additional insights into the fundamental processes in scour holes using experimental results, that can contribute to the improvement of equations and models that estimate scour near hydraulic structures.

The hydrodynamic conditions near the ES-SSB can be characterised as complex, as various elements and processes influence the local flow field. A field campaign by Rijkswaterstaat, the Dutch ministry of public works, and a data analysis of the obtained velocity by Broekema (2016) have identified the following flow properties near the inlet sections of the barrier: a contraction of the flow at the downstream end of the bed protection, the presence of large-scale gyres, a jet-like streamwise velocity profile, both vertical flow attachment and separation in the downstream scour hole and grid turbulence. Broekema (2017b) has shown that an additional acceleration through conservation of potential vorticity may suppress vertical flow separation on downward slopes and therefore the formation of a vertical recirculation zone. This process could be crucial in the scour holes near the ES-SSB where vertical flow attachment at the relatively steep upstream scour slope is still observed during certain stages in the tidal cycle. The relative shallowness of the flow may have a large impact, since shallow flows can contain large-scale coherent structures that can significantly contribute to the transverse exchange of mass and momentum. Therefore, the development of large-scale gyres and the generation of turbulence in the shear layers may be a key component of the flow.

Scale experiments were conducted in the Fluid Mechanics Laboratory at Delft University of Technology to systematically investigate certain flow characteristics that are observed near the ES-SSB. A schematisation of the field situation was required to investigate the essential hydrodynamic processes in the scour holes near the barrier in a physical scale model. Necessary flow conditions in a scale model were:

a lateral velocity gradient, a local uniform depth increase, relative shallowness and grid turbulence. In the scale experiments, only the upstream slope of a scour hole was simulated, the side slopes were left out of consideration. The upstream scour slope was modelled by a straight, linearly sloping, downward slope. The conducted experiments can be considered to be an extension to previous experiments by Broekema (2017a). Particle image velocimetry (PIV) and acoustic Doppler velocimetry (ADV) were used to obtain the flow velocity at the water surface level and at multiple points near the downward slope, respectively.

In the scale experiments, two types of vertical flow states were observed at the location of the downward slope: vertical flow attachment along the full width of the jet flow, and vertical flow separation at the jet centre. In the latter, it was found that the flow remained vertically attached in the horizontal shear layers of the jet. Besides a lateral velocity gradient, it was found that a mild slope steepness and a relatively low ratio of the upstream flow width over the width of the lateral expansion contribute to vertical flow attachment. The horizontal structure of the flow revealed that a contraction of the flow at the location of the downward slope was observed in all experimental runs. It was concluded that convergence of the surface flow near the slope is not necessarily a characteristic for vertical attachment of a jet flow, but may also be observed in case of vertical flow separation of the jet centre. This is different from results of previous experiments by Broekema (2017a). For five experimental runs, it was expected that vertical flow attachment could result from an additional acceleration through conservation of potential vorticity. This could, however, not be proven from velocity measurements that were obtained with PIV. Possibly other hydrodynamic processes are of importance that contribute to vertical flow attachment in longitudinal deepening shallow flows. No significant differences were found in the horizontal structure of the mean surface flow between experiments with vertical attachment and vertical separation of the jet centre.

The added effect of grid turbulence on the flow structure was investigated in the scale experiments. ADV measurements in the centerline of the flume show no significant differences for the vertical flow conditions between a corresponding experiment without grid turbulence, provided that the grid is not located directly at the start of the slope. The PIV measurements only show small differences in the mean structure of the streamwise surface flow, namely a reduction of the jet centre velocity in the case of grid turbulence. When the grid is positioned directly at the upstream edge of the slope, large deviations in the velocity field are found compared to a case without the added effect of grid turbulence. All these experiments resulted in vertical attachment at the location of the downward slope. As the pillars of the barrier are located at a certain distance from the scour hole, it is expected that the experiments in which the grid is positioned directly upstream of the slope are not representative for the situation near the ES-SSB.

Two methods were used to relate the measured flow conditions in the scale experiments to bed shear stresses: the Reynolds shear stress τ_{xz} and the turbulence kinetic energy (TKE). Comparing the estimations for the bed shear stresses between experiments with vertical flow attachment and separation shows that higher bed shear stresses are expected for attached flows. This strengthens the expectation that vertical flow attachment in the scour holes of the ES-SSB can enhance scour development. Lastly, it was found that, based on higher intensities of the TKE, grid turbulence could contribute to higher bed shear stresses in the horizontal mixing layers of the jet. This may have an impact on the side slope development, and side slope stability.

Contents

List of Figures

List of Tables

Nomenclature

Abbreviations

Abbreviation	Description
2DCS	Two-Dimensional Coherent Structure
ADCP	Acoustic Doppler Current Profiler
ADV	Acoustic Doppler Velocimetry
BFS	Backward Facing Step
CP	Camera position
DCC	Direct Cross-Correlation
DFT	Discrete Fourier Transform
ES-SSB	Eastern Scheldt Storm Surge Barrier
HPL	High Pressure Laminate
LDA	Laser Doppler Anemometry
MAD	Median Absolute Deviation
MWL	Mean Water Level
NAP	Dutch reference level (Normaal Amsterdams Peil)
PIV	Particle Image Velocimetry
PTV	Particle Tracking Velocimetry
ROI	Region of interest
RWS	Dutch ministry of public work (Rijkswaterstaat)
SLE	Shallow Lateral Expansion
SML	Shallow Mixing Layer
TKE	Turbulent Kinetic Energy
ZOAF	Zone Of Attached Flow
ZOSF	Zone of Separated Flow

Greek symbols

Symbol	Description	Unit
α	Entrainment coefficient	[-]
β	Upstream scour slope	[°]
δ_0	initial mixing layer width	[m]
Δ	Relative density	[-]
γ	Coefficient in scour formulas	[-]
λ	Characteristic length scale	[m]

Symbol	Description	Unit
	or scale factor	[-]
ν	Kinematic viscosity	[m^2/s]
ν_t	Turbulent viscosity	[m^2/s]
ω	Vorticity vector	[1/s]
ϕ	Angle of repose	[°]
ψ_c	Critical mobility parameter	[-]
ρ_s	Density of sediment	[kg/m^3]
ρ_w	Density of water	[kg/m^3]
τ	Wall shear stress	[N/m^2]
τ_c	Critical bed shear stress	[N/m^2]
τ_{xz}	Reynolds shear stress	[N/m^2]

Roman symbols

Symbol	Description	Unit
$\overline{u_c}$	Depth average critical flow velocity	[m/s]
$\overline{u}$	Mean flow velocity	m/s]
$\vec{u} = (u, v, w)$	Flow velocity components	[m/s]
a	Height of the false bottom	[m]
B	Width of the slot (jet)	[m]
$B1$	Upstream flow width	[m]
C	Chézy coefficient	[$m^{1/2}/s$]
c_f	Friction coefficient	[-]
D	Diameter of the object, height of the sill	[m]
	or width of the contracting elements	[m]
d	Centre-to-centre distance, grain diameter	[m]
	or bottom level w.r.t. the mean sea level	[m]
D_e	Channel expansion width	[m]
E	Turbulent kinetic energy	[J/m^3]
Fr	Froude number	[-]
g	Gravitational acceleration	[m/s^2]
G_*	Dimensionless grain diameter	[-]
h	Water depth	[m]
h_0	Initial water depth	[m]
i, j	Dimensional indices	[-]
K	Reduction factor for stability of grains on a slope	[-]
K_W	Inlet Strouhal number	[-]
L	Characteristic length scale	[m]
L_b	Bed protection length	[m]

Symbol	Description	Unit
$L_{b,m}$	Bed protection length in the model	[m]
$L_{b,p}$	Bed protection length in the prototype	[m]
L_R	Reattachment length	[m]
$\mathcal{L}$	Length of the domain	[m]
p	Pressure	[Pa]
Q	Discharge	[m^3/s]
q	Recirculation flow rate per unit width	[m^2/s]
Re	Reynolds number	[-]
S	Bed friction number or shallow wake parameter	[-]
s_{ij}	Rate-of-strain tensor	[1/s]
So	Grid solidity	[-]
T	Tidal period	[s]
t	Time level	[s]
t_1	Characteristic time scale	[s]
U	Characteristic velocity scale	[m/s]
u	Flow velocity in streamwise direction	[m/s]
$u1$	Upstream average flow velocity	[m/s]
u_m	Mean flow velocity	[m/s]
u_0	Mean inlet flow velocity	[m/s]
u_{*c}	Critical bed shear velocity	[m/s]
v	Flow velocity in lateral direction	[m/s]
W	Inlet width	[m]
$\mathcal{W}$	Width of the domain	[m]
x	Coordinate in streamwise direction	[m]
x_{lat}	Downstream distance from the lateral expansion	[m]
x_m	Longitudinal coordinate of the maximum scour depth	[m]
x_R	Longitudinal coordinate of the reattachment zone	[m]
y	Coordinate in lateral direction	[m]
y_m	Maximum scour depth	[m]
$y_{m,e}$	Equilibrium scour depth	[m]
z	Coordinate in vertical direction	[m]

1

Introduction

1.1. Scour development near the ES-SSB

The Eastern Scheldt (Dutch: *Oosterschelde*) is an estuary located in the province of Zeeland in the southwestern part of The Netherlands (Figure 1.1). The estuary is surrounded by Schouwen-Duiveland, Tholen, Zuid-Beveland and Noord-Beveland and has a surface area of approximately 351 km^2 (Smaal and Nienhuis, 1992). With the completion of the Eastern Scheldt storm surge barrier (ES-SSB) in 1986, the Eastern Scheldt is nowadays in partially open connection with the North Sea.

Figure 1.1: Location of the Eastern Scheldt including the floodplains of the North Sea flood (Wikipedia, 2011).

The construction of the ES-SSB has led to a significant reduction of the cross-sectional area of the inlet of the estuary. As a consequence, high local flow velocities can be observed in the vicinity of the barrier. The high flow velocities enhance the erosion of bed material and have resulted in scour holes on both sides of the barrier's inlets. Although the scour holes were anticipated in the design phase, continuous monitoring of the bathymetry shows that they are becoming deeper than initially predicted. Also, it seems that the development of the scour holes does not tend towards an equilibrium yet.

After the North Sea flood of 1953, which led to 1863 casualties and the evacuation of nearly 100,000 inhabitants (Visser, 2013), the Dutch government decided to revise the national coastal defence plan. In 1958 the parliament agreed upon the Delta Law, a plan with measures to ensure that a disastrous event as occurred in 1953 would not happen again. The Deltaplan included the construction of the Delta works, a series of dams, sluices and storm surge barriers which aimed to shorten the Dutch coastline. The largest structure of the Delta Works is the ES-SSB.

The initial design of the ES-SSB involved an impermeable dam that would completely isolate the Eastern Scheldt from the North Sea and thereby turn the estuary into a freshwater lake. An intensive political

debate to protect the ecological and economic value of the tidal marine system resulted in the adjustment of the storm surge barrier's design to a semi-open structure (Steenepoorte, 2016). The Eastern Scheldt maintained a salt-water habitat and a tidal character, although the latter under more moderate conditions. The main hydrodynamic characteristics of the Eastern Scheldt estuary before and after the completion of the ES-SSB are listed in Table 1.1.

Description	Unit	Pre-barrier	Post-barrier
Total surface	[km^2]	452	351
Water surface area (MWL)	[km^2]	362	304
Tidal flats area	[km^2]	183	118
Cross-sectional area mouth estuary	[m^2]	80,000	17,900
Mean vertical tidal range at Yerseke	[m]	3.70	3.25
Mean tidal volume	[$m^3 \times 10^6$]	1,230	880
Mean fresh water load	[m^3/s]	70	25

Table 1.1: Flow characteristics before and after the completion of the ES-SSB. Data provided by Tidal Waters Devision, Middelburg (Nienhuis and Smaal, 1994).

The ES-SSB is located in the mouth of the Eastern Scheldt and connects Schouwen-Duiveland to Noord-Beveland. The barrier has a total length of 9 km and includes two artificial islands as well as three operable sections, namely: Hammen, Schaar van Roggenplaat and Roompot (Figure 1.2). In these sections concrete pillars equipped with steel gates are installed to allow in- and outflow of water due to the tidal movement to and from the Eastern Scheldt estuary. During normal (tidal) conditions the steel gates are in open position. Only when a water level of +3.00 m above Normaal Amsterdams Peil (NAP) is predicted, the steel gates close thereby forming an impermeable barrier to protect the hinterland. The ES-SSB is designed to withstand a water level that statistically occurs once every 4000 years (Steenepoorte, 2016).

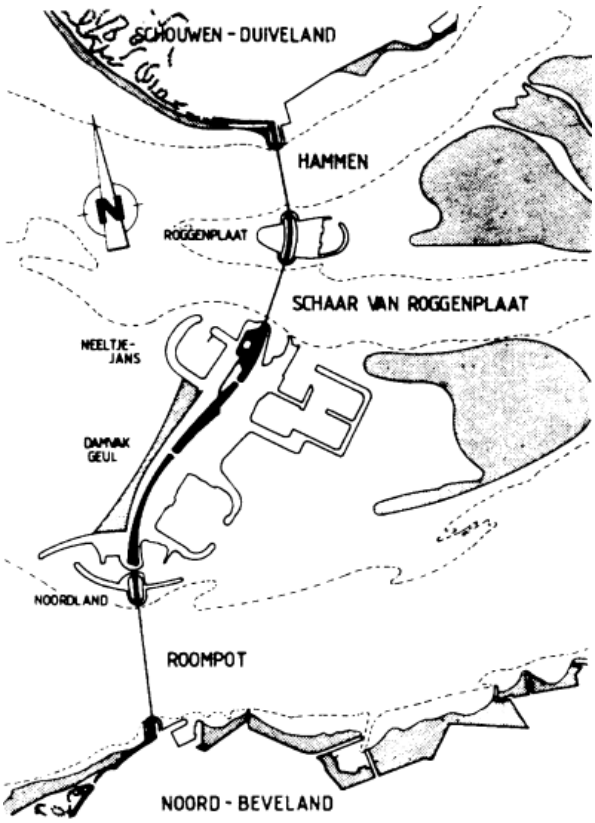

Figure 1.2: Overview of the different inlet sections and artificial islands of the ES-SSB (van Noortwijk and Klatter, 1999).

Scour can form a potential danger to the stability of hydraulic structures as steeper bed slopes in scour holes enlarge the risk of geotechnical instabilities. To prevent failure of the structure by shear failure or flow slides, a bed protection is often applied (Hoffmans and Verheij, 1997). A bed protection relocates the scour hole such that it develops at a safe distance from the hydraulic structure. In the case of the ES-SSB, a bed protection with a length of 550-650 m has been applied on each side of the barrier's inlets. This bed protection consists of asphalt mats, stone-asphalt mats, block mats and an edge beam (Visser, 1991). A schematic representation of the ES-SSB, its bed protection and the developed scour holes is illustrated in Figure 1.3.

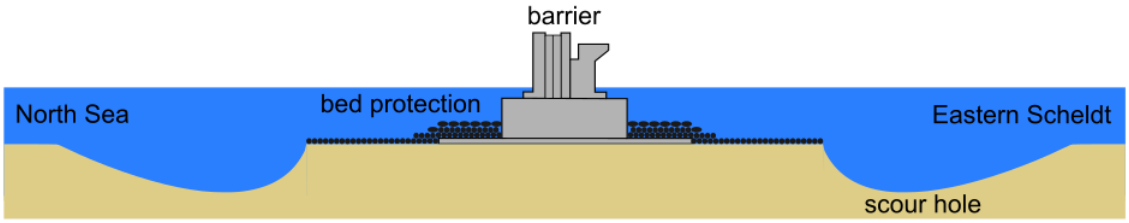

Figure 1.3: Schematic representation of a longitudinal cross-section of the scour hole development near the ES-SSB.

Based on literature (Hoffmans and Verheij, 1997), it is expected that the conveyance cross-sectional area increases during the development of scour holes. This leads to a deceleration of the flow, and subsequently to a decrease in the erosion capacity, such that an equilibrium state can be reached for a large enough increase in flow area. Despite a large increase in water depth, high flow velocities are still observed near the bed in the scour holes of the ES-SSB (Broekema, 2017b) which are in contradiction to continuity. This implies that the scour holes have not yet reached an equilibrium state and erosion is still ongoing.

A remarkable observation at the downstream side of the ES-SSB is that a recirculation zone on the upstream slope of the scour hole only appears periodically during a tidal cycle. In such a vertical recirculation zone the near-bed velocities are more moderate compared to a situation in which the flow remains attached to the bed. Flow attachment results in higher bed shear stresses and therefore promotes erosion. Experiments by Broekema (2017a) have shown that the presence of a lateral velocity gradient in a flow can counteract flow separation on a downward slope and thus suppresses the formation of a recirculation zone. This could explain why high flow velocities still reach the bottom and scour development near the ES-SSB has not come to a stop.

1.2. Problem statement

Due to a lack of knowledge of the fundamental processes that cause local scour, current predictions for the equilibrium dimensions of the scour near the ES-SSB show a wide range of the maximum scour depth (see for instance van Velzen et al., 2015). Uncertainties in the predictions arise partially from the presence, thickness and erodibility of clay layers, but first and foremost from a lack of understanding of the flow conditions. Studies investigating scour near hydraulic structures have, for practical purposes, often focused on the equilibrium condition of scour holes. Empirical equations have been suggested that estimate the final dimensions of scour holes for specific configurations. These empirical equations usually include velocity scales, but do not account for all hydrodynamic processes in a scour hole. Additionally, scour studies have predominantly considered a two-dimensional vertical situation in which a uniform velocity profile in the lateral direction is assumed. At the ES-SSB large horizontal velocity differences are present in the flow, accompanied by large-scale gyres adjacent to the scour holes. On top of that, grid turbulence induced by the pillars of the barrier itself and the contracting behaviour of the flow are likely to affect the hydrodynamic conditions in the scour holes. As the flow near the ES-SSB can be characterised as shallow, i.e. the horizontal length scales of the domain are much larger than the water depth, a two-dimensional vertical framework is not satisfactory. Although not all-encompassing, a two-dimensional horizontal approach would be more suitable to describe the flow field near the ES-SSB. In order to fully understand the development of three-dimensional scour holes, more insight is required in the fundamental hydrodynamic processes and how these can contribute to the scour hole development.

1.3. Objective and research questions

The objective of this master thesis is to obtain more fundamental understanding of the flow patterns and turbulence structure in the vicinity of tidal barriers, such as the Eastern Scheldt storm surge barrier, and how these may contribute to ongoing scour. Detailed information on the flow conditions is of importance in understanding the formation and development of scour holes near open structure tidal barriers. This thesis aims to investigate the effect of horizontal uniformities in the flow upstream of a scour hole and how these influence the hydrodynamic conditions in the scour hole's proximity. Insight into the flow conditions could help to improve the equations and models that estimate scour near hydraulic structures. The main research question of this master thesis is:

What are the effects of a lateral velocity gradient and grid turbulence on the flow conditions in and near a downstream scour hole of an open structure tidal barrier, and how may this affect scour development?

The following sub-questions are formulated in order to answer the research question:

1. How can the hydrodynamic conditions that are characteristic for the flow field near the ES-SSB be reproduced in a scale experiment?
2. How does a lateral velocity gradient in the base flow affect the vertical structure of the flow field, and what is the effect of the vertical flow state on the horizontal structure of the flow?
3. How does grid turbulence influence the flow field in the model?
4. How can the flow conditions observed in the scale experiment be related to scour development?

1.4. Methodology

In order to answer the main research question and sub-questions, this master thesis first focuses on the current knowledge of the flow field near the ES-SSB and the literature that describes the observed scour and flow patterns in this region. The second part of this study consists of physical scale experiments that are conducted in the Fluid Mechanics Laboratory at Delft University of Technology.

The aim of the physical experiments is to systematically investigate the influence of a lateral velocity gradient and grid turbulence on the flow conditions in the vicinity of a downward slope. The experimental setup is based on a strongly simplified geometry of one of the inlet sections of the ES-SSB in which the downward slope simulates the upstream part of the downstream scour hole. The experimental variables that are tested are the steepness of the downward slope, the location of the horizontal expansion, the width of the jet and the presence of grid elements. The planned experiments are a follow-up on previous experiments by Broekema (2017a) and can also be considered to build upon the work of Talstra (2011) and van Prooijen and Uijttewaal (2002).

1.5. Report outline

Chapter 2 starts with a description of the topography and flow characteristics that are observed in the proximity of the ES-SSB. Additionally, chapter 2 addresses the current literature on the development and flow conditions in scour holes, a selection of relevant consequences of shallow flow dynamics and includes an introduction to vertical flow separation. Chapter 3 discusses the experimental setup, the scaling parameters, the experimental variables and the measurement techniques that were used. Results of the conducted experiments are given chapter 4. The obtained results are further discussed in chapter 5. Finally, chapter 6 gives the conclusions and recommendations for further research.

2

Literature study

The hydrodynamic conditions near the ES-SSB can be characterised as complex, as various elements and processes influence the local flow field. A lack of understanding of the flow pattern near the barrier complicates the prediction of scour. This literature review starts with an overview of the topographic and hydrodynamic observations near the ES-SSB that are considered to be important in the development of the scour holes. Additionally, to get a grip on the ongoing erosion this literature study addresses the basics of sediment transport and the current knowledge of hydraulic processes in two- and three-dimensional scour holes. Then, the effect of the shallow conditions and a selection of flow characteristics observed near the ES-SSB will be treated. At last, flow separation will be discussed in more detail as the formation of recirculation zones in the scour holes is expected to significantly influence the scour process.

2.1. Topography and flow characteristics near the ES-SSB

The most dominant tidal constituent in the North Sea is the M2 -tide, which causes the Dutch coastline to have two high waters and two low waters per day. Under normal circumstances, the steel gates of the ES-SSB are in open position enabling the exchange of water between the North Sea and the Eastern Scheldt. Since the flow through the gate's of the ES-SSB experiences resistance, the water levels of the North Sea and the Eastern Scheldt predominantly differ. This results in a maximum head loss over the barrier of approximately 1 m and flow velocities through the gates of the inlet sections that can reach up to 4 m/s and higher (Bijlsma et al., 2017).

A consequence of keeping the tidal system intact in the design of the ES-SSB is that relatively high local flow velocities now persist in the vicinity of the barrier compared to the velocities in the mouth of the estuary prior the construction of the barrier. Additionally, the barrier results in an outflow that is highly turbulent. Both flow properties enhance the erosion of bed material and thereby give an explanation for the development of the scour holes near the inlet sections on both sides of the ES-SSB. Although a bed protection was applied to secure the stability of the barrier, scour holes on each side of the inlet sections have grown to a significant depth.

Figure 2.1 shows an overview of bathymetry measurements taken near the mouth of the Eastern Scheldt estuary in 2013. In the bathymetry data, one can recognise the tidal channels that direct the in- and outgoing flow of the estuary towards the barrier's inlet sections. Additionally, the effectiveness of the bed protection can be observed as the scour holes developed at a desired distance from the ES-SSB.

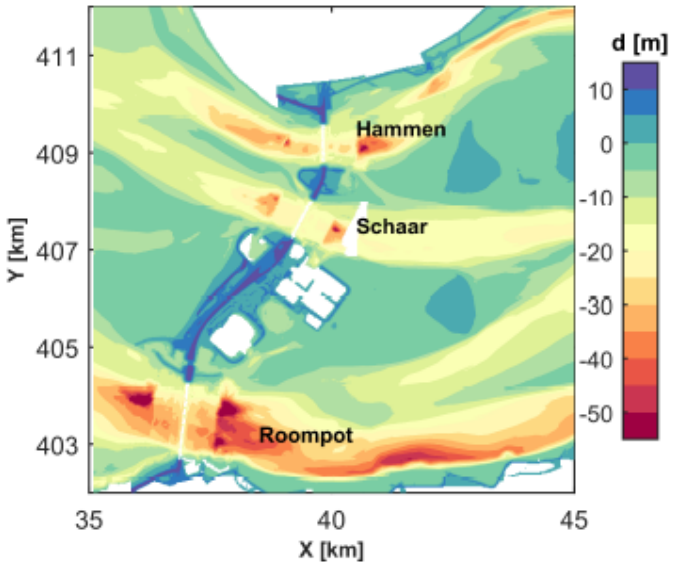

Figure 2.1: Bathymetry measurements taken in 2013 in the vicinity of the ES-SSB with Schouwen-Duiveland and Noord-Beveland situated in the top and bottom of the figure, respectively. The colour bar on the right indicates bottom level with respect to the mean sea level. The geometry of the barrier can be recognised by the blue coloured curved line. The axes indicate the position in RD-coordinates (*Dutch: Rijksdriehoekscoördinaten*) (Broekema, 2017b).

The development of the scour holes near the ES-SSB has been closely monitored since the end of the construction phase. Bathymetry measurements near the ES-SSB are taken between two and four times per year. These show that scour holes are present at both sides of the barrier's inlets. The deepest scour hole, with a depth of 34 m (2012), is located on the east side of Roompot inlet (Roompot-East). The bathymetry data also indicates that several geotechnical instabilities have occurred. The largest of these instabilities dates from 2005 when a volume of approximately 850.000 m^3 was eroded from the northern scour hole of Roompot-East. Some of the geotechnical instabilities have caused undermining of the bed protection resulting in subsidence of the edge beam (van Velzen et al., 2015).

In order to understand the local flow conditions near the ES-SSB and their role in the scour process, Broekema (2016) has performed a data analysis on flow velocities measured in the proximity of the scour holes. The velocity data were collected by Rijkswatersaat (RWS), the Dutch ministry of public works, between January 2014 and July 2016 using several Acoustic Doppler Current Profilers (ADCP) during a field campaign that was intended to map the flow conditions near the barrier. In addition to the data analysis, aerial and satellite footage were used in an attempt to qualitatively describe the flow conditions near the barrier's inlet sections, see Figure 2.2.

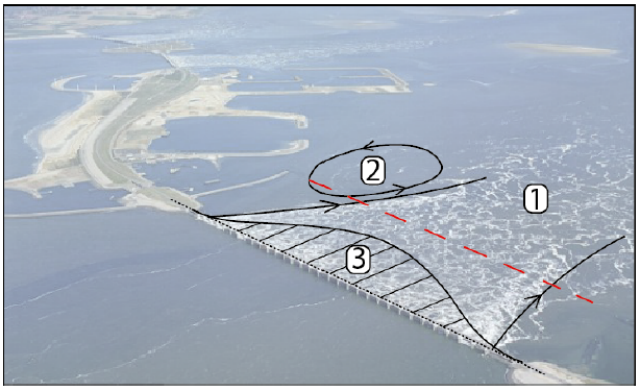

Figure 2.2: Aerial image of the Roompot inlet section during flood conditions. The flow shows a contracting behaviour downstream of the barrier with a maximum contraction near the deepest part of the scour (1). Large-scale gyres are present adjacent to the flow downstream of the inlet section (2). The relative strength of the flow varies along the inlet section and shows characteristics of a tidal jet (3). The red dotted line indicates the end of the bed protection (Broekema, 2016).

Although small differences in streamlines and flow velocities can be observed between the inlet sections, the flow structures are considered to be similar. The following hydrodynamic flow properties were observed by Broekema (2016, 2017b) downstream of the barrier's inlets:

1. *Contracting flow.* Based on the foamy top layer it can be seen that, for certain stages in the tidal cycle, the flow converges downstream of the inlet section. This is indicated by number 1 in Figure 2.2. After low water, the streamlines downstream of the barrier are approximately straight or even diverging. As the water level difference between the sea and basin-side becomes larger, velocities increase and the flow starts to show a contracting behaviour towards the deepest part of the scour hole. The contraction of the flow reaches a maximum approximately one hour after maximum flood conditions. The flow contraction was explained from conservation of potential vorticity (Broekema, 2017b) which will be further discussed in subsection 2.2.5.
2. *Large-scale gyres.* Depending on the local geometry near the inlet sections, one or two small eddies start to form adjacent to the flow downstream of the barrier after low water. These eddies grow into large-scale gyres, represented by number 2 in Figure 2.2, as flow velocities increase during a tidal cycle. Simultaneously with the increasing contracting behaviour of the flow, the large-scale gyres tend to move towards the centre of the tidal channel. As a consequence of this displacement, the discharge carrying cross-sectional area is reduced leading to higher flow velocities above the scour hole. Figure 2.3 depicts the streamlines of the depth-averaged interpolated flow field for three distinct moments in the tidal cycle, in which the growth and movement of the large-scale gyre towards the central axis of the tidal channel can be recognised.

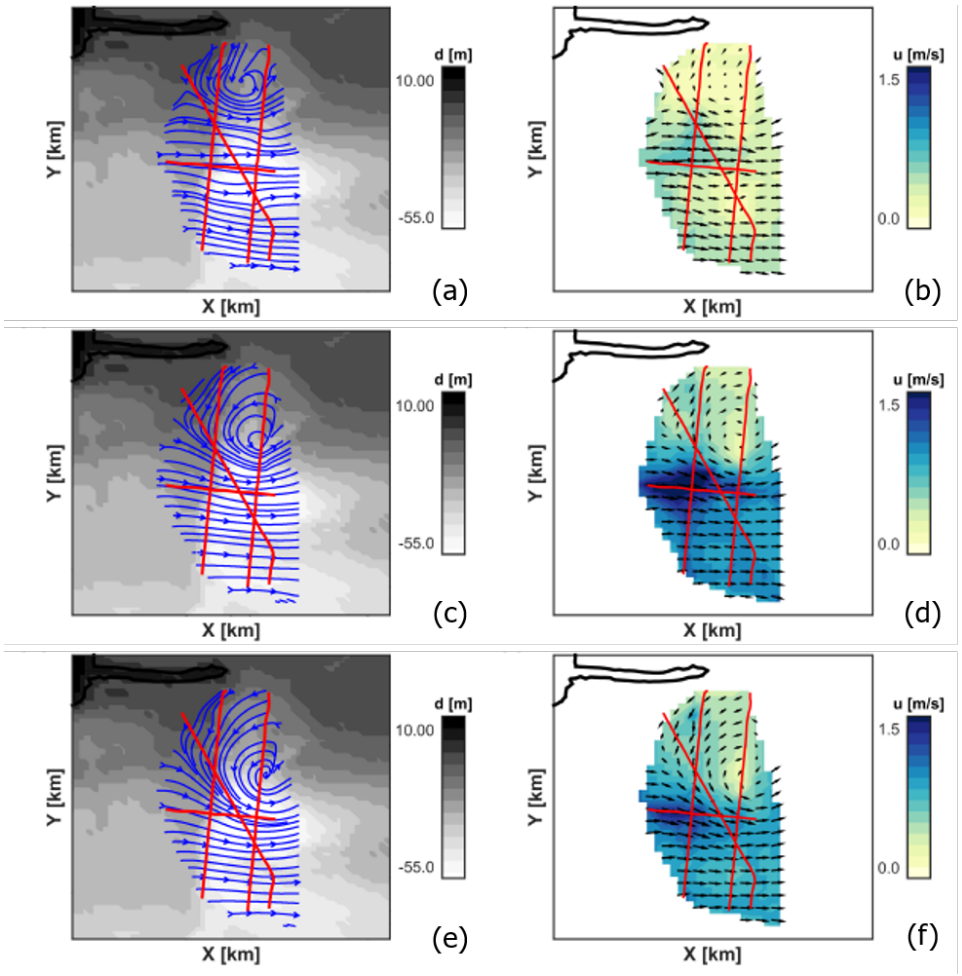

Figure 2.3: Interpolated depth-averaged flow field streamlines (left) and the velocity magnitude (right) of the Roompot inlet section for three moments in the tidal cycle: (a-b) 1.5 hours past low water, (c-d) maximum flood and (e-f) 1 hour past maximum flood. The red lines indicate the sailed trajectories of the vessel. The grey-scale and colour bar on the right of the figures show the bathymetry and flow velocity, respectively (Broekema, 2017b).

3. *Jet-like flow structure.* Velocity measurements near the ES-SSB show that after low water the streamwise velocity is more or less uniform along the inlet sections, see Figure 2.3. Slightly higher flow velocities are observed above the scour holes, which can possibly be explained by the larger local flow depth and thus a reduced influence of friction. The streamwise velocity along the inlet sections becomes more non-uniform in lateral direction towards maximum flood conditions. The flow velocities at the edges of the inlet sections are smaller compared to the flow in the middle of the inlet sections. The flow thus shows characteristics of a jet-like structure, as indicated by the curved profile (number 3) in Figure 2.2 for the Roompot section. Due to this lateral velocity gradient, the flow is internally sheared and has the tendency to rotate. A larger background vorticity due to an increase of the lateral velocity gradient could be another trigger that causes the large-scale gyres to grow during the tidal cycle.

4. *Vertical flow separation.* Data obtained from stationary ADCP's in the scour holes of the ES-SSB have indicated that return currents are present at certain stages in the tidal cycle. When flow velocities at the end of the bed protection are moderate, i.e. in the order 1 m/s, a clear return flow can be observed on the upstream slope of the scour hole. When velocities increase further, vertical flow separation is suppressed and the flow remains attached to the bed. This is not expected for steep slopes, where an abrupt deceleration of the flow normally leads to vertical separation of the boundary layer. In Broekema (2017b) it is hypothesised that through conservation of potential vorticity, the flow may experience an additional acceleration that counteracts the adverse pressure gradient which would normally result in vertical flow separation. Figure 2.4 depicts the velocity vectors for a streamwise cross-section of Roompot East during two stages in the tidal cycle. Remarkable is that that high flow velocities can still be observed in the near-bottom layer during maximum flood conditions (lower panel Figure 2.4). High momentum and turbulence therefore find its way to the bed of the scour hole. The associated higher bed shear stresses could explain why the scour process is still ongoing and no equilibrium for the bathymetry has been reached yet.

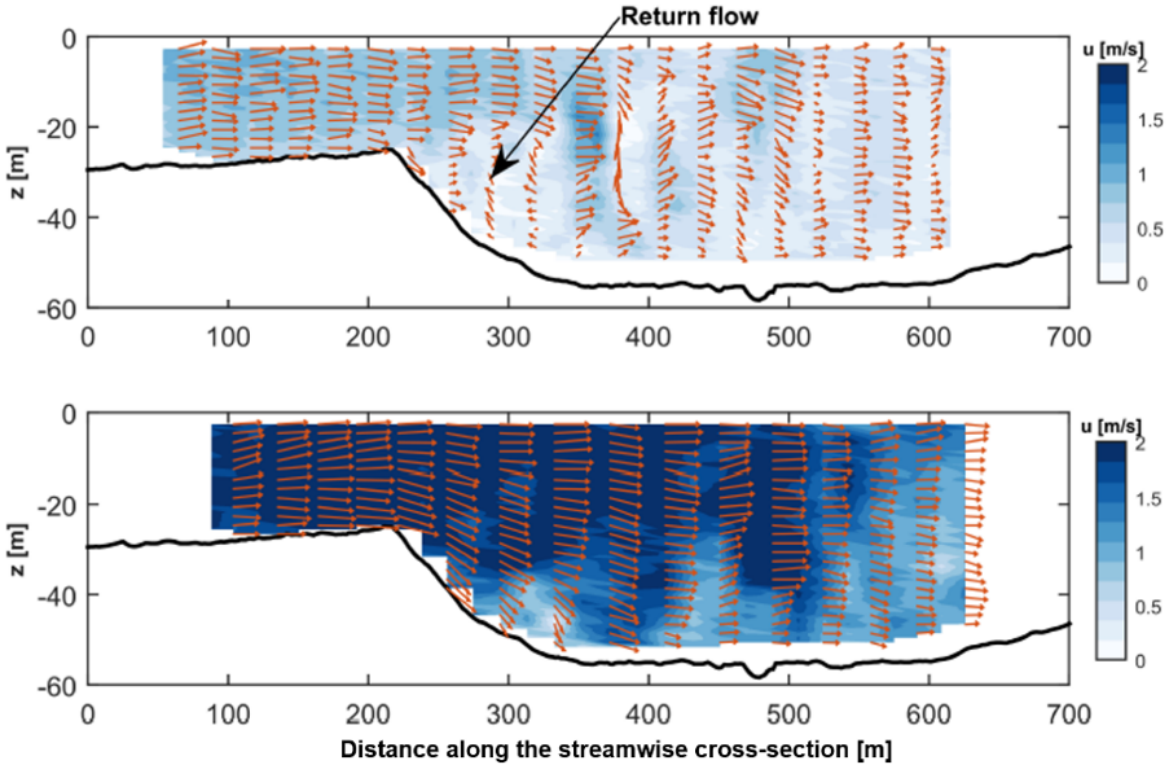

Figure 2.4: Velocity vectors along a streamwise cross-section of Roompot East through the scour hole. In the upper panel can be seen that a return current is present at the upstream scour slope after slack tide. The lower panel depicts the same transect for maximum flood conditions. The flow remains attached and high velocities can be observed near the bed. The colour bar on the right depicts the magnitude of the flow velocity (Broekema, 2017b).

5. *Grid turbulence.* Directly downstream of the inlet sections it can be observed that the flow is disturbed by the pillars of the barrier, as indicated in Figure 2.5. The wake structures which are formed show a systematic pattern as the pillars are all evenly spaced along the inlet sections. The spatial scales of the flow features in the wakes gradually grow in the downstream direction until tens of meters downstream of the barrier where the individual wakes possibly interact with one another. It remains unknown if the turbulence structures merge and grow into large coherent structures or damp out in downstream direction. The observed flow pattern shows a strong relation with grid turbulence which for instance is described by Uijttewaal and Jirka (2003).

Figure 2.5: Flow structure downstream of the barrier that shows characteristics of grid turbulence (VVV Zeeland, 2018).

From the collected field data near the ES-SSB can be concluded that several hydrodynamic processes play a role in shaping the flow structure near the barrier and its scour holes. An important property of the flow near the ES-SSB is that the horizontal dimensions largely exceed the water depth. This significantly affects the structures that can be observed near the barrier. It was found that high velocities reach the near the bed layer of the scour holes, suggesting that scour is still ongoing and that no new equilibrium for the bathymetry has been reached. How and to what extent the identified hydrodynamic processes contribute to the ongoing erosion near the ES-SSB still remains unknown.

2.2. Scour holes

Before addressing the effects of shallow flow dynamics, this literature study will first discuss the current knowledge on the development and flow conditions of scour holes. To further understand the development of scour holes downstream of a bed protection, as is the case at the ES-SSB, this section will start with a short introduction to the basics of sediment transport and the stability of grains on a slope. Then, the scour development near the ES-SSB will be discussed from a two-dimensional vertical point of view. Expressions that describe the development of two-dimensional vertical scour holes will be discussed as well as the prevailing flow conditions. Lastly, the section addresses the flow conditions observed in three-dimensional scour holes and previous scale experiments of Broekema (2017a).

2.2.1. An introduction to sediment transport

Hydraulic structures that form an obstruction in a flow may give rise to local erosion or scour. Changes in local flow characteristics, such as the flow velocity or turbulence intensity, can significantly affect the sediment transport capacity of a flow. A local imbalance between the actual sediment transport and the capacity of the flow to transport sediment then results in the deformation of the bed. This deformation of the bed, and with it the adjustment of the hydraulic conditions, continues until a new equilibrium is eventually reached (Hoffmans and Verheij, 1997).

A well-known criterion for the initiation of movement of uniform granular material on a horizontal bed is given by Shields (Schiereck, 2003). Under the assumptions of a uniform flow and a domain in which the width is much larger that the depth, Shields proposed the so-called critical mobility parameter:

$$\psi_c = \frac{\text{critical load}}{\text{strength}} = \frac{\tau_c}{(\rho_s - \rho_w)gd} = \frac{u_{*c}^2}{\Delta g d} = \frac{\overline{u_c}^2}{C^2 \Delta d} \tag{2.1}$$

where τ_c is the critical shear stress, ρ_s the sediment density, ρ_w the density of water, g the gravitational acceleration, d the grain diameter, u_{*c} the critical bed shear velocity, Δ the relative density, $\overline{u_c}$ the depth average critical flow velocity and C the Chézy coefficient. As there are various degrees of incipient motion, the Shields diagram does not contain one single curve but a broad belt that represents the initiation of particle movement. The belt is divided into several stages that are described in Figure 2.6.

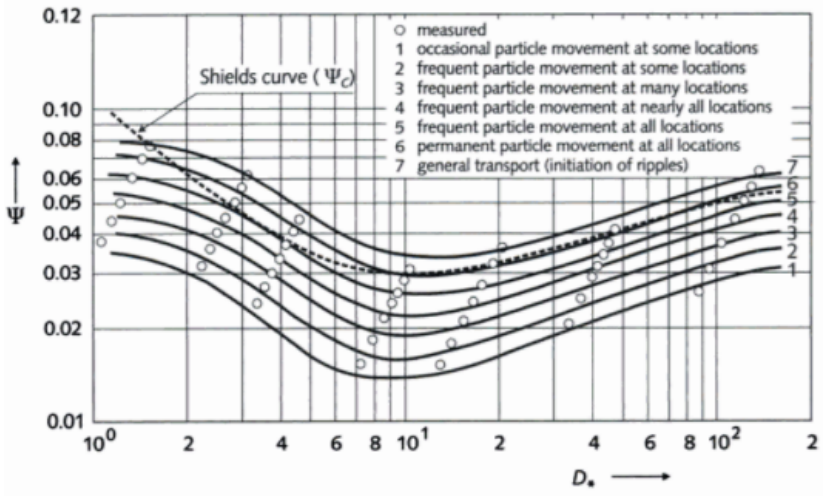

Figure 2.6: Modified Shields diagram by Van Rijn (Hoffmans and Verheij, 1997).

The stability of grains on a slope, for instance in a scour hole, differs from the initiation of movement of particles on a horizontal bed. When the angle of a slope is equal to the angle of repose, then nearly any load will induce movement of the particles. According to Schiereck (2003), a reduction factor for the strength has to be included when considering the stability of grains on a slope. In the case of a slope with angle β that is smaller than the angle of repose ϕ, then the reduction factor for the strength of a flow in the direction of a downward slope $K(\beta_\parallel)$ is given by:

$$K(\beta_\parallel) = \frac{F(\beta_\parallel)}{F(0)} = \frac{\sin(\phi - \beta)}{\sin\phi} \tag{2.2}$$

where $F(\beta_\parallel)$ is the strength of a slope in the direction of the flow and $F(0)$ the strength of a horizontal bed. Furthermore, a reduction factor for the strength of slope that experiences a parallel flow is given by:

$$K(\beta_\perp) = \frac{F(\beta_\perp)}{F(0)} = \sqrt{1 - \frac{\sin^2\beta}{\sin^2\phi}} \tag{2.3}$$

in which $F(\beta_\perp)$ is the strength of a side slope. An exception should be made when the flow is in the direction of an upward slope. The grains may then experience an additional force that stabilises the particles. The reduction factors stated in Equation 2.2 and Equation 2.3 are applied as correction for the sediment diameter (Schiereck, 2003).

2.2.2. 2DV expressions for scour near the ES-SSB

Several studies have proposed expressions that describe the equilibrium dimensions and time development of scour holes near hydraulic structures (Hoffmans and Verheij, 1997). Scour studies have predominately considered a two-dimensional vertical situation from which expressions are derived that estimated the maximum scour depth, thereby assuming a uniform velocity profile in the lateral direction. These expressions are mainly used for practical purposes such as in the design of a bed protection. A bed protection is applied to ensure the safety of hydraulic structures and relocates the scour hole to a

desired distance from the structure. Figure 2.7 depicts a representation of a scour hole downstream of a sill with bed protection and includes the parameters that are often used in expressions that describe scour development.

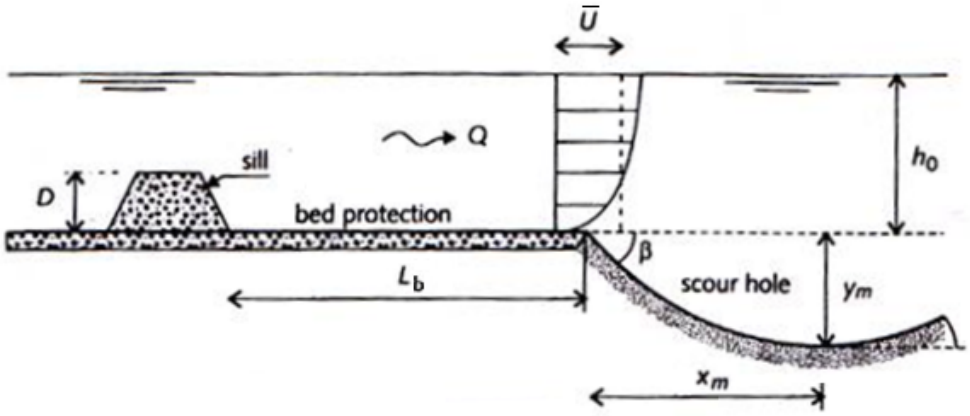

Figure 2.7: Schematic overview of the development of a scour hole downstream of a sill with bed protection. The parameters indicate: the height of the sill D, the length of the bed protection L_b, the discharge Q, the mean flow velocity U, the upstream scour slope β, the horizontal length of the end of the bed protection to the maximum scour depth x_m, the maximum scour depth y_m and the water depth h_0. After Hoffmans and Verheij (1997).

One of the expressions that is commonly used to describe the time development of the maximum scour depth downstream of a bed protection is given by:

$$\frac{y_m}{y_{m,e}} = 1 - e^{\ln\left(1-\frac{\lambda}{y_{m,e}}\right)\left(\frac{t}{t_1}\right)^{\gamma}} \tag{2.4}$$

in which $y_{m,e}$ is the equilibrium scour depth, γ a coefficient, t the time, λ a characteristic length scale and t_1 a characteristic timescale for which $y_m = \lambda$. Various definitions for λ can be found in the literature. In case of shallow turbulent flows, the characteristic length scale can be chosen as the size of the largest eddies which is in the order of the water depth (Hoffmans and Verheij, 1997). Equation 2.4 is most accurate when the equilibrium scour depth is larger than the initial water depth. Several studies have proposed values for the coefficient γ that best fit their experimental results (Breusers, 1966, Dietz, 1969, van der Meulen and Vinjé, 1975).

According to Breusers (1966), Equation 2.4 can for the development phase, that is when $t < t_1$, be reduced to the following expression:

$$\frac{y_m}{h_0} = \left(\frac{t}{t_1}\right)^{\gamma}. \tag{2.5}$$

2.2.3. Flow conditions in 2DV scour holes

In order to understand the ongoing erosion process in scour holes, insight is required in the hydrodynamic conditions that prevail in scour holes. As a first step, this literature study will address the regions that can be observed in a two-dimensional vertical scour hole where the upstream scour slope has (nearly) reached its geometric equilibrium state. In a mathematical modelling approach, Hoffmans and Booij (1993) have distinguished the following characteristic zones in two-dimensional scour holes: a transient zone, a mixing layer, a recirculation zone, a relaxation zone, and a new wall-boundary layer (Figure 2.8).

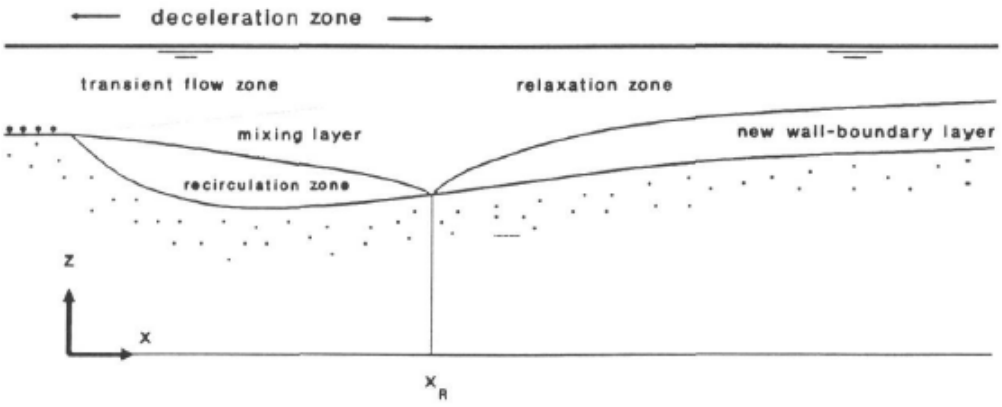

Figure 2.8: Characteristic zones in a two-dimensional scour hole. The location of the reattachment zone is indicated by x_R (Hoffmans and Booij, 1993).

Due to a velocity difference between the transient flow zone and the recirculation zone, a mixing layer originates at the transition point from the fixed bed (bottom protection) to the erodible bed. The flow in this mixing layer location is highly turbulent and expanding in downstream direction. The centre of the mixing layer shows an increased curvature towards the bottom layer with distance from the bed protection. The region where the bottom part of the mixing layer comes in contact with the bed is defined as the reattachment zone. The flow in the reattachment zone can be characterised by small flow velocities and is considerably turbulent (Guan et al., 2013). Downstream of the reattachment point a new wall-boundary layer develops. This new wall-boundary layer grows in the relaxation zone where the streamwise velocity restores to a logarithmic profile. An example of the flow conditions in a two-dimensional vertical erodible scour hole behind a submerged weir is presented in Figure 2.9.

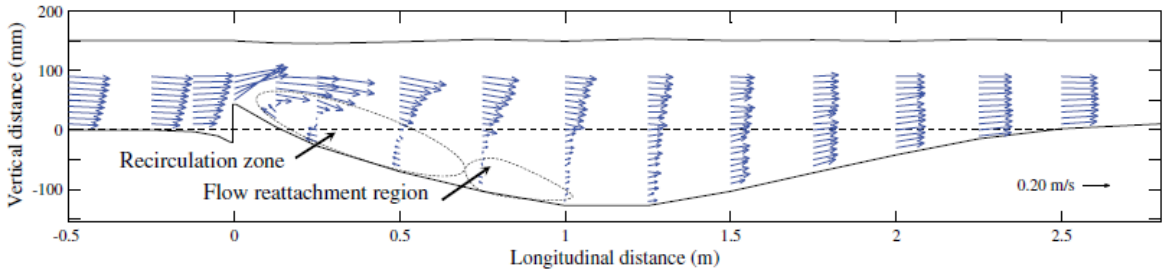

Figure 2.9: Flow conditions in a two-dimensional vertical scour hole behind a submerged weir. The clear water experiment by Guan et al. (2013) shows a vertical recirculation zone and a flow reattachment region at the upstream scour slope.

2.2.4. Flow conditions in three-dimensional scour holes

Although there are similarities between observed flow characteristics between two- and three-dimensional scour holes, the flow pattern in three-dimensional scour holes can be characterised as more complex. Research on the development of three-dimensional scour holes in heterogeneous subsoils, that are subjected to a uniform incoming flow, has been the topic of several graduation theses in the past few years. To investigate the scour holes in the Rhine-Meuse delta, Koopmans (2017) and Stenfert (2017) have both performed physical experiments with three-dimensional scour holes including a poorly erodible top layer. In collaboration with the physical experiments of Stenfert (2017), the graduation thesis of Bom (2017) contains a numerical study on the hydrodynamic processes in three-dimensional scour holes.

An important finding through the experimental pilot-study by Uijttewaal et al. (2016) and Koopmans (2017) is that a three-dimensional scour hole results in a deeper and faster growing scour hole compared to a quasi-two-dimensional scour hole as experimentally observed by van Zuylen (2016). Additionally, it is stated that three-dimensional effects can enhance the local scour hole development. In her experiments, Koopmans (2017) used a sand bed that was covered by a concrete top layer with an

oval recess to simulate a scour hole in a poorly erodible layer, see Figure 2.10a. A qualitative sketch of geometric characteristics and observed hydrodynamic processes is depicted in Figure 2.10b.

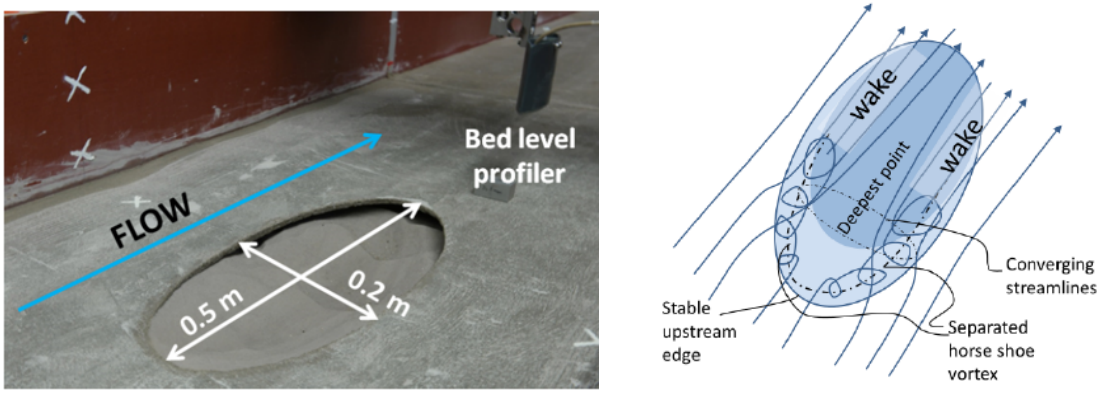

(a) (b)

Figure 2.10: Physical experiments with a three-dimensional scour hole geometry. (a) Photograph of the experimental setup by Koopmans (2017). (b) Qualitative sketch of the identified characteristics in the scour hole (Uijttewaal et al., 2016).

From the work of Uijttewaal et al. (2016), Koopmans (2017), Stenfert (2017) and Bom (2017) several hydrodynamic processes can be distinguished that could play a role in the development of three-dimensional scour holes. The above studies have in common that the considered scour holes were all subjected to a uniform incoming flow. The observed flow conditions will be discussed briefly below.

1. *Recirculation zone on the upstream scour slope.* Similar to two-dimensional scour holes, the above-stated studies all describe a recirculation zone at the upstream scour slope. Through a parameter study, Bom (2017) concludes that a recirculation zone will form in a three-dimensional scour hole if the upstream slope has an angle of 20° or larger. According to Stenfert (2017), the size of the recirculation region varies in time as the reattachment point is not fixed but shows deviations in both longitudinal and lateral direction.

2. *Contraction of the flow.* Bom (2017) gives two possible explanations for the convergence of the streamlines in the upstream part of scour holes. First, the scour hole causes a redistribution of momentum at the location of the scour hole. This results in larger local discharge in the area above the scour hole and thus converging streamlines. A second explanation is given by the principle of conservation of potential vorticity. This will be explained in more detail in subsection 2.2.5. At the downstream part of the scour hole, all studies describe the divergence of streamlines.

3. *Horseshoe vortex shape.* Flow separation at the upstream slope continues partly along the side slopes of the scour hole. This results in the formation of a horseshoe-shaped vortex, see Figure 2.10b. The horseshoe vortex has an outward directed flow near the bed at the sides slopes. This results in the transport of sediment out of the scour hole. Additionally, the horseshoe vortex contributes to the contraction of the flow towards the scour hole. Downstream of the deepest point of the scour hole the vortex disintegrates into less structured wakes (Bom, 2017, Koopmans, 2017, Uijttewaal, 2018). It should be noted that the horseshoe-shaped vortex is an effect of the geometry of the scour hole and does not result from upstream horizontal variations in the flow as will be discussed in subsection 2.2.5.

In addition to the above-described flow phenomena, another flow characteristic can be identified from studies by Vermeulen et al. (2015) and Bhuiyan et al. (2007).

4. *Recirculation zones in the horizontal plane.* The formation of horizontal recirculation zones adjacent to a scour hole was observed in a river bend (Vermeulen et al., 2015) and near a W-weir (Bhuiyan et al., 2007). Besides to formation of the recirculation zones, it was found that the upstream flow converged towards the scour holes leading to a jet-like streamwise velocity profile.

2.2.5. Characteristics of a lateral non-uniform flow over a bed topography

Besides the observations of hydrodynamic phenomena in two- and three-dimensional scour holes described above, another influence on the flow conditions may originate from horizontal non-uniformities, such a lateral velocity gradient, in the flow upstream of scour holes (Broekema, 2017b). As results of previous experiments by Broekema (2017a) have been promising in explaining the observed vertical structure of the flow near the ES-SSB and were thereby the main incentive for this master thesis, his work will be discussed in more detail in this section.

A lateral velocity gradient is present in a flow when the streamwise velocity varies in the lateral direction normal to the flow. This is, for example, the case in the inlet sections of the ES-SSB, where the flow shows characteristics of a tidal jet with high streamwise flow velocities in the middle of the tidal channels and low streamwise flow velocities on the sides. In his study Broekema (2017b) states that a lateral velocity difference in the flow upstream of a scour hole, if sufficiently large, can cause ongoing scour. This statement is supported by physical experiments described in Broekema (2017a).

Broekema (2017b) suggests that a flow with a lateral velocity gradient experiences an additional acceleration for an increased water depth in streamwise direction. This is explained by the principle of conservation of potential vorticity. For a two-dimensional horizontal flow, the vertical vorticity can be described by:

$$\omega_z = \frac{\partial v}{\partial x} - \frac{\partial u}{\partial y}. \tag{2.6}$$

An expression for conservation of potential vorticity can be derived from the two-dimensional shallow water equations, when ignoring Coriolis forces, and is displayed in Equation 2.7,

$$\frac{D}{Dt}\left(\frac{\omega}{h}\right) = \frac{\nu_t}{h}\nabla^2\omega - \frac{c_f}{2h^2}\left[\omega\sqrt{u^2+v^2} + u\frac{\partial}{\partial y}\sqrt{u^2+v^2} - v\frac{\partial}{\partial x}\sqrt{u^2+v^2}\right] \tag{2.7}$$

where h is the local water depth, ν_t the turbulent viscosity, c_f the bed friction coefficient, u the streamwise velocity in the x-direction and v the lateral velocity in y-direction. Potential vorticity along a fluid trajectory is a conserved quantity if no other vorticity inputs are present (Pietrzak, 2015) and if the vertical structure of the flow is more or less depth uniform. The concept of conservation of potential vorticity for an eddy that experiences an increasing water depth in streamwise direction is illustrated in Figure 2.11.

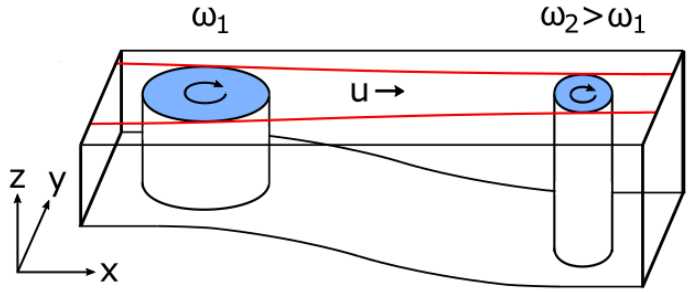

Figure 2.11: The concept of conservation of potential vorticity. Due to an increasing water depth, an eddy will stretch in vertical direction and rotate faster. The convergence of streamlines at the surface is indicated by the red lines. After Pietrzak (2015).

Under the assumption that the lateral velocity is much smaller than the streamwise velocity, a condition that approximately holds at the ES-SSB, inviscid flow and low friction Broekema (2017b) shows that Equation 2.7 can be reduced to:

$$u\frac{\partial}{\partial x}\left(\frac{\omega}{h}\right) = 0. \tag{2.8}$$

From Equation 2.8 it follows that if the water depth in the y-direction is assumed to be uniform, vorticity increases proportionally to the relative depth increase. If the lateral velocity is assumed to be small, the

vorticity is mainly determined by the lateral gradient of the streamwise flow velocity. A depth increase will, therefore, result in a larger streamwise gradient and thus to a more concentrated flow.

In Broekema (2017b) it is hypothesised that the additional acceleration resulting from conservation of potential vorticity, if large enough, may counteract the adverse pressure gradient that causes flow separation at locations with a (sudden) longitudinal depth increase, such as a straight downward slope. Experiments by Broekema (2017a) have shown that a lateral velocity gradient, obtained by a horizontal contraction in the flow, can indeed counteract flow separation on downward slopes up to 1:2 .

The presence of a lateral gradient in the flow upstream of a scour hole, which is also observed near the ES-SSB, is likely to have an impact on the ongoing scour process. The work of Broekema (2017a) shows that through conservation of potential vorticity, a flow with a lateral velocity gradient will be further squeezed for an increasing depth. Also, the additional acceleration of the flow can counteract flow separation and thus the formation of a recirculation zone on the upstream scour slope. As a consequence, high streamwise momentum can be advected to the bed resulting in high bed shear stresses that promote scour development.

In the case of the ES-SSB, the water depth is much smaller compared to the horizontal dimensions of the domain. This may significantly affect the structures in the flow. It was concluded from field observations that lateral velocity gradients are present in the flow. Therefore, a two-dimensional vertical framework may not correctly present the flow conditions that are observed near the ES-SSB. A two-dimensional horizontal approach could be more suitable. Unanswered from the work of Broekema (2017a,b) remains what the effect is of a limited water depth. All experiments by Broekema (2017a) were executed in a 40 cm wide flume with a water depth of approximately 55 cm. The flume's width to water depth ratio was therefore relatively large ($W/h_0 \approx 0.7$). The next section will elaborate on the properties and characteristics patterns of shallow flows.

2.3. Shallow flow dynamics

The flow near the ES-SSB can be characterised as a shallow flow. As a consequence of the unrestricted horizontal dimensions of the domain and a relatively small water depth, instabilities in horizontal mixing layers are able to develop into large-scale coherent structures. A closer look at the bathymetry of for example Roompot East shows that the deepest points of the scour hole are observed near the sides of the inlet section where horizontal mixing layers are present (Figure 2.1). This raises the suspicion that coherent structures in the mixing layer contribute to the ongoing scour. How the observed flow structures near the ES-SSB such as the jet flow, the large-scale gyres and grid turbulence influence the scour hole development is currently still unknown. To investigate these effects a two-dimensional horizontal approach is more suitable than the two-dimensional vertical framework that was discussed in subsection 2.2.3.

2.3.1. The effect of shallowness on turbulent flows

Shallow flows can be characterised as bounded, layered turbulent flows in a domain in which the two horizontal dimensions largely exceed the vertical dimension (Jirka and Uijttewaal, 2004). In case of hydraulic flows, the vertical dimension is in general limited as the water depth is bounded by the water surface and the bottom boundary. The horizontal dimensions then define the extent of the flow domain. Typical examples of swallow flows are low-land rivers, shallow lakes and coastal waters. The flow near the ES-SSB can also be characterised as a shallow flow as the horizontal dimensions near the ES-SSB, that are in the order of kilometres, are far larger than the local water depth ($h \approx$25 m).

An effect of the shallowness is that the vertical restriction strongly constrains vortex stretching, an important dissipation mechanism in three-dimensional flows. Shallow flows, therefore, show a strongly two-dimensional character and can contain large coherent structures that persist over longer time and length scales compared to fully three-dimensional flows. A schematic overview of the vortex stretching mechanism and its limitations due to the number of dimensions is depicted in Figure 2.12.

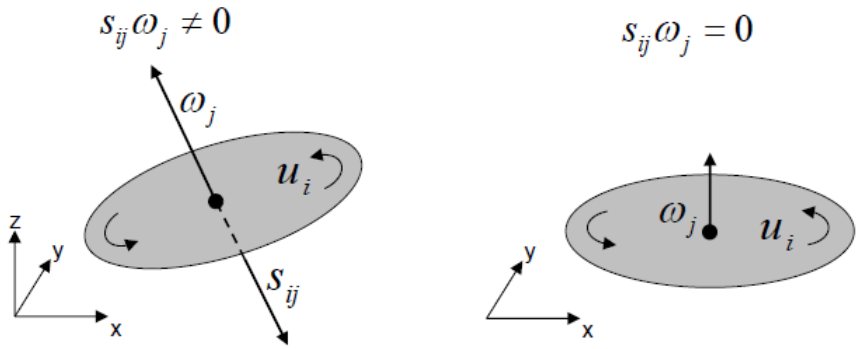

Figure 2.12: The dependence of the vortex stretching mechanism on the number of dimensions for: (a) a three-dimsenional space and (b) a two-dimensional space. The symbols in this figure represent the dimensional indices $i, j \in \{1, 2, 3\}$, the flow velocity component u_i, the vorticity vector ω and the rate-of-strain tensor s_{ij} (Talstra, 2011).

Figure 2.12a shows that in a three-dimensional space vortices can stretch in the direction perpendicular to the plane of rotation. In this transformation, energy is transferred from large to smaller length scales. Eventually, energy will be converted into heat when the length scales of the turbulent motions become so small, at the so-called Kolmogorov scales, that molecular viscosity starts to dominate. The transition of energy from the largest length scales to the eddies with the smallest length scales is known as the energy cascade (Uijttewaal, 2018). In case of a two-dimensional space, vortices cannot be stretched and energy will prolong in larger length scales, see Figure 2.12b. It should be noted that even though shallow flows show a strong two-dimensional character, they are affected by three-dimensional turbulence which will finally result in the breakdown of coherent structures.

Shallow flows can be subject to transverse disturbances that evolve into large two-dimensional coherent structures (2DCS) such as shallow jets, shallow wakes and shallow mixing layers. Two-dimensional coherent structures are by Jirka (2001) defined as: "connected large-scale turbulent fluid masses that extend uniformly over the full water depth and contain a phase-correlated vorticity, with the exception of a thin near-bottom boundary layer". These flow structures significantly contribute to the transverse exchange of mass and momentum and are thus of importance in sediment transport and the dispersion of pollutants in shallow waters.

The growth of 2DCS is governed by processes such as the entrainment of non- or weakly turbulent fluid and the pairing of individual vortices, known as vortex pairing or vortex merging. The pairing of several vortical cores is illustrated in Figure 2.13. Two-dimensional coherent structures grow in size as they propagate in the downstream direction until the structures grow so large that bed friction finally results in a breakdown.

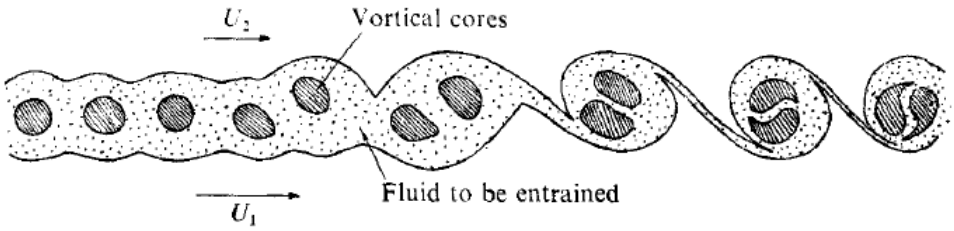

Figure 2.13: Growth of vortical cores in a mixing layer with $U_1 > U_2$ (Winant and Browand, 1974).

2.3.2. Categorisation of 2DCS

Jirka (2001) has identified three mechanisms that can generate 2DCS, namely: topographical forcing, internal transverse shear stabilities and secondary instabilities in the base flow. A more detailed description of each of these generation mechanisms is given in this subsection.

1. *Type A: Topographical forcing.* The strongest generation mechanism that gives rise to 2DCS is the presence of obstacles in the flow field, see instance Figure 2.14a. Topographic features such as islands, headlands or jetties can cause local flow separation and result in return velocities in the lee of obstacles. Due to intense transverse shear, instabilities are able to grow into larger 2DCS. The Von Kárman vortex street is a well-known example of vortex shedding by topographic forcing.
2. *Type B: Internal transverse shear instabilities.* A less strong generation mechanism is driven by a lateral velocity difference in the base flow. These velocity differences create instabilities that gradually grow to 2DCS. In the field, this type of generation mechanisms can, for instance, be observed near a confluence in which the branches have unequal flow velocities (Figure 2.14b). Additionally, velocity variations in the transverse direction can originate from differences in water depth or roughness.
3. *Type C: Secondary instabilities in the base flow.* The weakest generation mechanism includes the emergence of 2DCS from three-dimensional turbulence structures in a uniform base flow. Due to ejection and sweep events caused by the bottom boundary, the base flow contains three-dimensional turbulence structures. This generation mechanism suggests that these structures are amplified by slight imbalances such as localised roughness zones, subtle bottom features or a gradual deceleration of the base flow resulting in the formation of 2DCS.

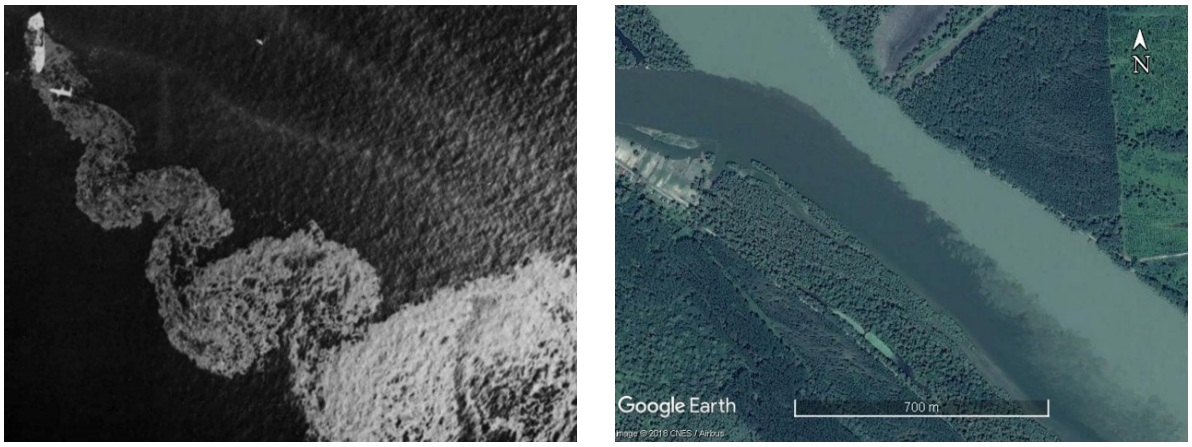

(a) (b)

Figure 2.14: Two examples of generation mechanisms of 2DCS. (a) Topographical forcing: the stranded oil tanker Argo Merchant on the Nantucket Shoals in 1976 (van Dyke, 1982). (b) Internal transverse shear instabilities: the confluence of the Drava and the Danube near Osijek, Croatia (source: Google Earth 2018).

Near the ES-SSB two types of generation mechanism of 2DCS can be recognised. First of all, topographical forcing can be observed as vortices are shed from the pillars of the barrier. The effect of the pillars of the barrier can be associated with grid turbulence and has been discussed before in section 2.1. Secondly, 2DCS are generated by internal transverse shear instabilities in the mixing layer between the jet flow and the ambient flow. Properties of the coherent structures that form near the inlet sections of the ES-SSB will be further discussed in subsection 2.3.3.

2.3.3. Shallow jets

As was described in section 2.1, the flow in the inlet sections of the ES-SSB can be characterised as a shallow jet with high streamwise velocities in the centre and lower velocities near the edges. To understand how shallow jets affect the flow, this subsection will discuss some important properties of shallow jets that have been described in the literature.

A shallow jet can be observed when a high-velocity discharge is injected through an opening (e.g. a slot, channel or nozzle) into a stagnant fluid in which the horizontal dimensions greatly exceeded the water depth. Due to the velocity difference between the interior of the jet and the ambient fluid, a free

shear layer develops on both sides of the opening, causing the ambient fluid to accelerate and the core of the jet to decelerate. As a result, the shear layers spread in lateral direction resulting in a growth of the shallow jet with increasing distance from the entrance Cohen (2012). Figure 2.15 depicts an example of a shallow turbulent jet.

Figure 2.15: Shallow turbulent jet: the outflow of the river IJssel, The Netherlands (source: Google Earth 2018).

Shallow plane jets

Dracos et al. (1992) have studied the meandering of plane turbulent jets in shallow flows. A subdivision into a near field, middle field and far field was proposed to describe the evolution of shallow jets in downstream direction. In the near field ($x/h \leq 2$), the jet is characterised by a regular development with significant influence of the boundaries. The middle field ($2 < x/h \leq 10$) is dominated by secondary currents and shows a strong three-dimensional velocity profile. The secondary currents are damped out in the far field ($x/h > 10$) where the flow starts to meander around its centre plane. Additionally, large counter-rotating vortices that alternate on both sides of the jet can be observed in this region. These flow features are nearly depth uniform and may thus be referred to as 2DCS. For a decreasing ratio of h/B, in which B is the width of a slot that extends over the full depth, it was found that the 2DCS start to develop closer to the jet entrance (Figure 2.16).

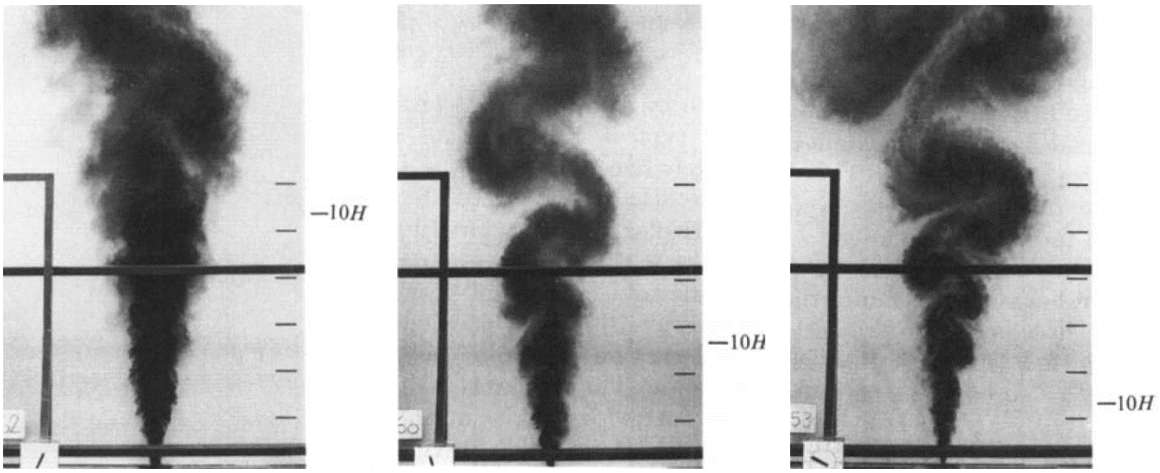

Figure 2.16: Dye visualisation of shallow jets produced by an exit velocity of 110 cm/s through a 1 cm wide slot for decreasing relative water depths: (a) $h/B = 16$, (b) $h/B = 8$ and (c) $h/B = 4$. The solid bars are the support structure of the Laser Doppler Anemometry (LDA). The spacing between the marks on the right side of each figure equals 30 cm. A distance of 10 times the water depth is indicated for each scenario (Dracos et al., 1992).

Shallow tidal jets

Del Roure et al. (2009) have investigated the evolution of starting jet vortices for various idealised tidal inlet layouts. In their study is stated that the most important non-dimensional parameter describing the character of the formed jet eddies (dipole) is the inlet Strouhal number K_W:

$$K_W = \frac{W}{UT} \tag{2.9}$$

in which W is the inlet width, U the maximum cross-sectionally averaged tidal velocity through the inlet over the tidal cycle and T the tidal period. In accordance with results obtained by Wells and van Heijst (2003), it was found that depending on the inlet Strouhal number three classes of starting vortices can be distinguished for tidal inlets. For a value of $K_W < 0.13$ the formed vortex dipole escapes the reversing tidal flow and propagates away from the tidal mouth. When K_W equals 0.13 it is found that the vortex dipole remains stationary during reverse tide, as the propagation velocity of the dipole matches the velocity of the sink flow (i.e. the flow towards the tidal inlet). In case $K_W > 0.13$, a large proportion of the starting jet formation is captured in the inlet channel when the flow reverses. As a consequence, these vortical structures interact with the newly formed jet vortices of subsequent tidal cycles.

For the ES-SSB, with a varying width of the inlet sections in the range of approximately 800 till 1500 m, a velocity scale of about 1.5 m/s and a tidal period of 44700 s, the inlet Strouhal number K_W varies between 0.012 till 0.022. In accordance with the above, the flow passing the ES-SSB can therefore be characterised by jet vortices that escape the reversing tide and do not interfere with starting jet vortices formed at subsequent tidal cycles.

2.3.4. Shallow mixing layers

Mixing layers are developing between the outflow of the barrier's inlet sections and the adjacent large-scale gyres. According to Talstra (2011) a mixing layer can be described as: "a region of lateral mixing and lateral shear, widening in downstream direction, containing a sequence of large-scale 2DCS that move downstream". In contrast to shallow jet or wake flows, the vertical vortices generated in mixing layers all have the same sign of rotation. Therefore, the vortices have the tendency to merge and form larger flow structures.

Two types of specific shallow flow geometries containing mixing layers that have been widely studied are the Shallow Mixing Layer (SML), where the flow geometry consists of a confluence with two parallel streams that have different flow velocities, and the Shallow Lateral Expansion (SLE) in which a uniform channel flow experiences an abrupt sideways widening. This literature study only addresses the SLE, as this geometry has most in common with the flow field that is observed near the ES-SSB. In his dissertation Talstra (2011) has investigated the influence of steady gyres on the development of 2DCS in shallow separating flows. A summary of the terminology and important processes that were used to describe the SLE will be given in the next paragraph.

As mentioned about the SLE before, the incoming flow experiences an abrupt sideways widening as depicted in Figure 2.17. In the lee of the channel expansion a recirculation zone forms that extends in downstream direction, qualitatively described by the reattachment length L_R. The downstream end of the recirculation zone is bounded by the reattachment point, i.e. the location where the main flow impinges on the solid wall again. The recirculation zone often contains a primary and secondary gyre, as indicated in Figure 2.17 by the larger and smaller gyre respectively. The occurrence of a secondary gyre is dependent on the local geometry and an adverse pressure gradient caused by the primary gyre. The location where the primary gyre (possibly) separates from the solid wall is named the secondary separation point. The lateral shear, that is caused by the difference in flow velocity between the main flow and recirculation zone, gives rise to the development of a mixing layer downstream of the primary separation point. In this mixing layer, disturbances grow from Kelvin-Helmholtz instabilities to large-scale 2DCS that are roughly proportional to the width of the mixing layer. The 2DCS are responsible for the transfer of streamwise momentum from the main flow towards the recirculation zone. The mixing layer central plane is shifted to the low-velocity side in downstream direction where the streamwise velocity difference becomes gradually smaller.

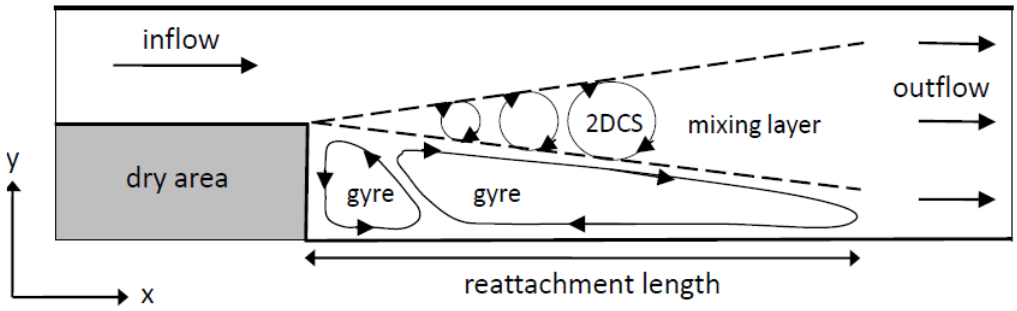

Figure 2.17: Top view of a Shallow Lateral Expansion (SLE) including the most important flow features (Talstra, 2011).

Babarutsi et al. (1989) have proposed the following expression for the bed friction number S that characterises the recirculation flow of SLE's:

$$S = c_f \frac{D_e}{2h} \tag{2.10}$$

where D_e is the width of the channel expansion. From their experiments Babarutsi et al. (1989) conclude that when $S < 0.05$, the reattachment length L is about eight times the expansions width and recirculation flow rate per unit width q approaches the relationship $q \simeq 0.08 u_0 D_e$ in which u_o is the mean velocity at the inlet. For larger values of the bed friction coefficient, both the reattachment length and recirculation flow rate decrease and become independent of the horizontal length scale. For $S > 0.1$ other expressions are stated that described characteristics of the recirculation flow.

2.3.5. Shallow wakes and grid turbulence

Downstream of the pillars of the ES-SSB the flow velocity is locally reduced resulting in the appearance of multiple wakes. A variation of shallow wakes when they occur downstream of obstacles has been considered by Ingram and Chu (1987), Chen and Jirka (1995) and Jirka (2001). The behaviour of wakes in the lee of an obstruction in a flow can be described by the bed friction number or shallow wake parameter S:

$$S = c_f \frac{D}{h} \tag{2.11}$$

in which c_f is a friction coefficient, D the diameter of the obstacle and h the water depth. The ratio expresses the stabilising effect of bed friction over the destabilising effect of the transverse shear (Chu et al., 1991). Three different wake flows downstream of a cylinder can be distinguished uniquely depending on the bed friction number: the vortex street pattern with an oscillating vortex shedding mechanism, the unsteady bubble wake in which instabilities grow from a recirculating bubble attached to the object, and the steady bubble including a turbulent wake without growing oscillations. Dye visualisations of the wake flow around a cylinder are shown in Figure 2.18.

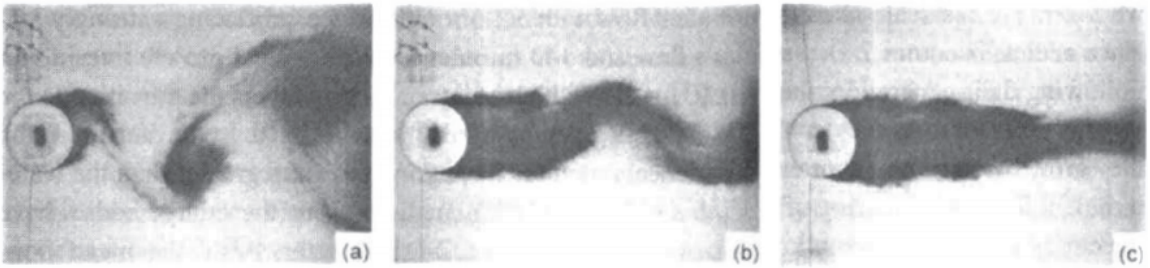

Figure 2.18: Flow patterns of shallow wakes produced by a cylinder: (a) Vortex street pattern $S \leq 0.2$, (b) Unsteady bubble wake $0.2 \leq S \leq 0.5$ and (c) Steady bubble wake $S \geq 0.5$ (Jirka, 2001).

Shallow grid turbulence is a special case of wake flow in which equally distributed grid elements cause several wakes to interact. The effects of grid turbulence on a shallow flow have been investigated by

Uijttewaal and Jirka (2003). In their experiments, a row of cylindrical grid elements with equal spacing has been deployed to disrupt an incoming shallow base flow, see Figure 2.19. The solidity of the grid So is defined as follows:

$$So = \frac{D}{d} \tag{2.12}$$

in which D is the diameter of the cylindrical elements and d the centre-to-centre distance between them. Results indicate that two-dimensional features are present in the flow downstream of the grid elements. These features have length scales in the order of, or larger than the water depth and grow in the downstream direction. It is stated that the decay of the features is determined by the size of the elements rather than the grid spacing.

Figure 2.19: Dye visualisation of grid turbulence (Uijttewaal and Jirka, 2003).

The concrete pillars of the ES-SSB can be interpreted as grid elements that disturb the in- and outgoing flow of the Eastern Scheldt estuary. Assuming a pillar width of 5.5 m and a centre-to-centre distance of 45 m, the ES-SSB can be characterised by a grid solidity of $So \approx 0.12$. For a low grid solidity, the eddies that are formed do not have the opportunity to fully merge before they are dissipated. It is therefore expected that the eddies which are shed from the barrier's pillars do not grow into large-scale flow structures. The grid turbulence, however, can have an effect on the background vorticity.

2.4. Vertical flow separation

Field observations in section 2.1 have shown that vertical flow separation occurs at the end of the bed protection at certain moments in the tidal cycle and that a recirculation zone then forms on the upstream scour slope, see Figure 2.4. The formation of the recirculation zone significantly affects the flow conditions in the scour hole and thereby the erosion process. The conditions that trigger flow separation are nowadays only partially understood.

The dissertation of Talstra (2011) describes that flow separation occurs when a boundary layer loses contact with its associated solid wall, as schematically represented in Figure 2.20. This is caused by an adverse pressure gradient, acting in the direction opposite to the local flow direction. This adverse pressure gradient can, for instance, be caused by a deceleration of the flow near a (sudden) widening or deepening of the flow.

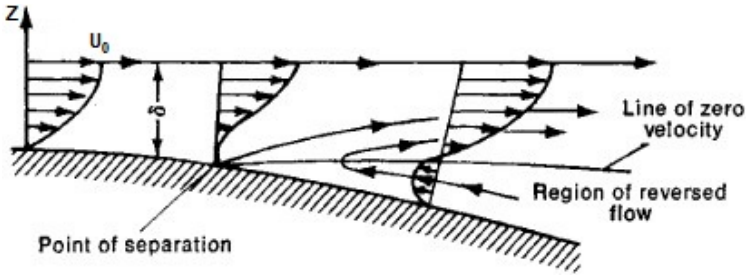

Figure 2.20: Representation of flow separation on a curved geometry in which δ indicates the boundary layer thickness. After Campbell (2016).

Under normal conditions, that is when the boundary layer remains attached, the wall shear stress τ and the favourable pressure gradient ($^{Dp}/_{Dx} > 0$) act in opposite direction enabling the existence of a boundary layer, see Figure 2.21a. When an adverse pressure gradient ($^{Dp}/_{Dx} < 0$) would act in the same direction as the wall friction, there cannot be an equilibrium between forces. Therefore, a sufficiently large adverse pressure gradient causes the flow to change sign such that the wall shear stress acts in the opposite direction, as represented in Figure 2.21b.

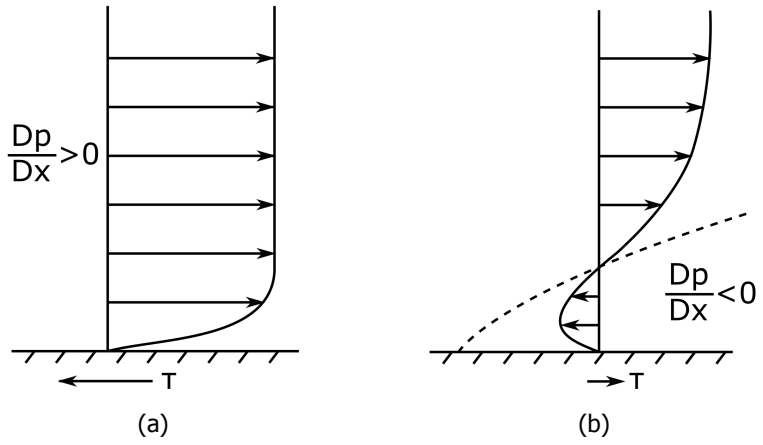

Figure 2.21: Effect of the pressure gradient on the boundary layer equilibrium. (a) A favourable pressure gradient results in a thin boundary layer with a large velocity gradient and high wall shear stress. (b) An adverse pressure gradient causes flow reversal in the near wall region. The dashed line indicates the of zero velocity.

The exact location of the point of separation is dependent on the flow geometry, local wall roughness and on the prevailing turbulence conditions. For curved and straight geometries, the separation point may oscillate along a solid boundary. In contrast to a variable location, the point of flow separation can in some cases also be observed at a fixed location, e.g. for the Backward Facing Step (BFS) where the surface geometry contains an abrupt increase in water depth. A more quantitative description of turbulent boundary layer separation is given by Simpson (1989). In his study it is stated that for streamlined geometries in a steady free-stream two-dimensional separation begins intermittently, i.e. backflow at a location only occurs periodically for short time intervals. The fraction of time that flow reversal can be observed then increases in the downstream direction.

2.5. Summary and discussion

The flow near the Eastern Scheldt storm surge barrier (ES-SSB) is highly complex as various processes influence the local flow field. A lack of understanding of the hydrodynamic conditions near the barrier has resulted in a wide range of predictions for the equilibrium scour dimensions (see for instance van Velzen et al., 2015). Observations of the flow near the ES-SSB at each of the inlet sections show similarities, namely: a contraction of the flow, the presence of large-scale gyres, a jet-like streamwise velocity profile, vertical flow separation and grid turbulence. Some of these phenomena are only observed at certain stages in the tidal cycle.

To get a grip on the ongoing scour process near the ES-SSB, this literature study has addressed the basic theory of sediment transport and studies that describe the flow conditions in two- and three-dimensional scour holes. Scale experiments with a three-dimensional scour hole geometry (Koopmans, 2017, Stenfert, 2017, Uijttewaal et al., 2016) and a numerical study (Bom, 2017) have identified hydrodynamic processes that are also observed near the ES-SSB. The work of Broekema (2017a,b) on the effects of lateral velocity gradients upstream of downward slopes has been discussed in more detail. It was shown that through conservation of potential vorticity a flow containing a lateral velocity gradient may experience an additional acceleration. This favourable pressure gradient can suppress vertical flow separation and therefore the formation of a recirculation zone on downward slopes. This process could be crucial in explaining the hydrodynamic conditions and scour development near the ES-SSB.

The water depth near the ES-SSB is significantly smaller than the horizontal dimensions of the domain. As a consequence of the shallow conditions, the flow shows a strongly two-dimensional character and can contain coherent structures that exist over longer periods and have larger length scales compared to fully three-dimensional flows. Two-dimensional coherent structures (2DCS) are of importance as they can significantly contribute to the transverse exchange of mass and momentum and may play an important role in sediment transport. Several shallow flow characteristics were discussed that have been observed near the ES-SSB.

The last topic that is addressed in this literature study is flow separation. Flow separation occurs when a boundary layer loses contact with its associated solid wall (Talstra, 2011). Vertical flow separation is of importance as it determines the direction and magnitude of the flow velocity near the bed in scour holes and therefore strongly affects the erosion process. It is expected that flow separation at the upstream scour slope has a large influence on the scour development near the ES-SSB. Nowadays, the exact conditions that cause vertical flow separation are still only partially understood.

So far, previous studies to scour have mainly considered a two-dimensional vertical framework. The effect of horizontal non-uniformities in the flow, as for instance can be observed near the ES-SSB, are therefore ignored. The work of Broekema (2017a,b) has revealed that the presence of a lateral velocity gradient in a base flow can significantly influence the vertical flow structure near a downward slope and thereby the load that is acting on the bed. In conclusion, horizontal variations in the base flow are likely to affect the development of scour holes and should be included in a model approach when studying scour near, for example, the ES-SSB.

In addition to the above, it remains unknown what the effect is of shallow flow conditions on the development of scour. As described in subsection 2.3.1, shallow flow conditions can significantly contribute to the persistence of coherent structures in a flow. To further investigate the influence of 2DCS's and grid turbulence, on the flow field and scour hole development near the ES-SSB, a scale experiment could be set up in which the length and width of the domain, $\mathcal{L}$ and $\mathcal{W}$ respectively, are large compared to the water depth ($\mathcal{L} >> h$ and $\mathcal{W} >> h$).

The shallow water flume in the Fluid Mechanics Laboratory at Delft University of Technology is a suitable option for follow-up experiments of Broekema (2017a). With this flume the criteria for horizontal flow non-uniformities and shallow flow conditions can be met.

3

Laboratory experiments

This chapter presents the laboratory experiments that were conducted to investigate the influence of a lateral velocity gradient and grid turbulence on flow separation at a downward slope in a shallow water flow. The experiments are a follow-up on previous experiments by Broekema (2017a). Knowledge of the hydrodynamic conditions in the chosen experimental setup will contribute to the understanding of the fundamental processes in the development of the scour holes near the ES-SSB. The physical experiments were conducted in the wide shallow flume of the Fluid Mechanics Laboratory at Delft University of Technology.

To understand the fundamental hydrodynamic processes that play a role near the ES-SSB, Broekema (2017a) has performed experiments with a base flow including a lateral velocity gradient that is subjected to a local uniform depth increase. Unknown from these experiments remains what the effect is of shallow flow conditions and grid turbulence, characteristics that can also be observed near the ES-SSB. The aim of the laboratory experiments is therefore to investigate the effect of a shallow flow with a lateral gradient that is subjected to a local uniform depth increase and a grid.

3.1. Experimental setup

Several key elements are of importance to systematically investigate the dependence of vertical flow separation, as observed in the scour holes near the ES-SSB, in a scaled model. Also, simplifications of the observed situation are required to isolate flow processes in an experiment. The schematisation of the ES-SSB and the experimental layout will be addressed in this section.

3.1.1. Schematisation of the ES-SSB

Essential elements that should be reproduced in a scale experiment are the presence of a lateral gradient in the flow and a local uniform depth increase. In addition, to simulate the effect of shallow flow conditions it is required that the horizontal dimensions of the flume are significantly larger than the water depth. Finally, a grid is needed to mimic the grid turbulence that is generated by the pillars of the barrier.

To isolate the flow processes observed near the ES-SSB in a scaled model a strongly simplified experimental setup was required. The used model contained the following simplifications:

- *Bathymetry.* The used experimental setup only simulated the flow through one of the inlet sections of the barrier including only its downstream scour hole. In the model, the local depth increase by the upstream scour slope was assumed to be uniform and was simulated by a straight downward slope. The downstream part of the scour hole was not taken into account in the experimental setup. The reduced water depth at the location of the bed protection was reproduced by a false bottom that was installed in the flume. The model ignores aspects such as the upstream scour hole, the complex geometry of the scour hole, tidal channels, bed protection elements and bedforms.

- *Constant and unidirectional flow.* In all experimental runs, a constant discharge was maintained that was directed from the inlet section towards the outlet section of the flume. The influence of the tidal movement, and with that the reversal of the flow direction, was therefore ignored.
- *Geometry of the barrier*. The grid elements that were used to reproduce the grid turbulence near the ES-SSB were more simplistic compared to the geometry of the pillars of the barrier. Additionally, the sills that are located on the bottom between the pillars were not included in the grid's design.
- *Fixed, non-erodible bottom.* The bottom of the flume consisted of smooth high-pressure laminate (HPL) plates. As the experiments purely focused on hydrodynamic processes, no sediment was added to the experimental setup. Transport of sediment and the changing shape due to development of the scour holes in time were thus not taken into account in the model.

3.1.2. Facility and experimental layout

The experiments were conducted in the wide shallow flume of the Fluid Mechanics Laboratory at Delft University of Technology. This flume has a flat bottom with an effective length of 19.2 m, a width of 3.0 m and glass side walls with a height of 20.0 cm. An overview of an experimental layout that satisfies the schematisation as described in subsection 3.1.1 is depicted in Figure 3.1. In the remainder of this subsection, the motivation for this experimental layout will be discussed in more detail. The preliminary experiments that are described in Appendix B have had an important role in the decision for the final experimental layout. The exact dimensions of the experimental setup will be determined after considering various scaling parameters in the next section.

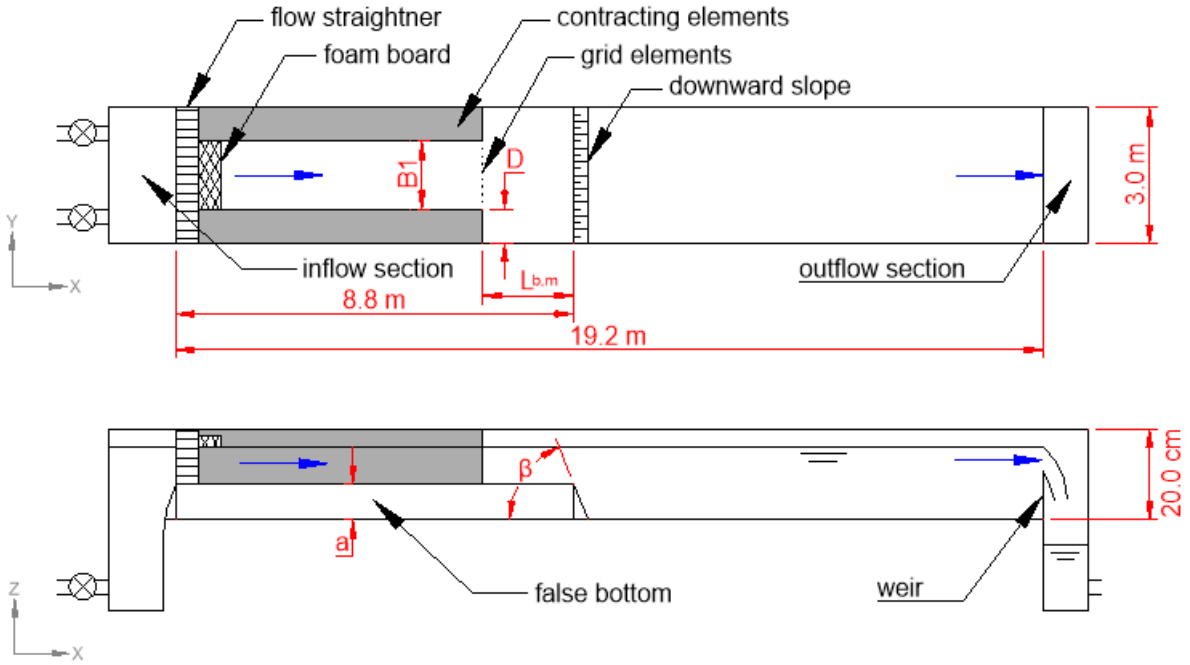

Figure 3.1: Top and side view of the experimental layout including the main dimensions of the shallow water flume. The variables indicate the upstream flow width $B1$, the width of a single contracting element D, the distance between the lateral expansion and the upstream end of the downward slope $L_{b,m}$ the height of the false bottom a and the upstream scour slope β. The blue arrows indicate the flow direction.

A false bottom with height a was installed in the flume to reproduce the difference in water depth caused by the scour holes near the ES-SSB. The false bottom was position in the upstream part of the flume and had a length of 8.8 m. This length was chosen as a compromise between the development length for the boundary layer and the distance downstream of the slope needed for measurements. The influence of the downstream scour hole was reproduced by a local uniform depth increase at the downstream end of the false bottom. A downward slope with steepness β was used to simulate the upstream slope of the scour hole.

To reconstruct the jet-like flow that can be observed near the ES-SSB in the experiment, contracting elements were placed on top of the false bottom along the glass side walls of the flume. At the location of the lateral expansion, a streamwise velocity difference is introduced as the fluid in the lee of contracting elements is less accelerated by the incoming flow. Higher flow velocities can therefore be found in the centerline of the flume that decreasing in sideways direction. This fulfils the requirement for a lateral gradient in the flow. The experimental layout can be classified as a shallow lateral expansion (SLE) as discussed in subsection 2.3.4 including a downstream local depth increase.

Considering a maximum water depth of 20.0 cm in the flume, a depth to width ratio is obtained of approximately 1:15 and depth to length ratio of about 1:96. As the horizontal dimensions are significantly larger than the maximum water depth, the flow in the flume is considered to be sufficiently shallow to simulate the hydrodynamic conditions near the ES-SSB. As a water level of 20.0 cm will result in overtopping of the flume, an even smaller water depth will be maintained in the experiment.

Grid turbulence generated by the pillars of the ES-SSB was simulated by an array of elements positioned at equal distance from one another. The complex geometry of a single pillar was simplified to a square beam.

To ensure that the flow upstream of the lateral expansion is more or less uniform and that streamlines are straight, a honeycomb grating was placed directly downstream of the inflow section. Behind the honeycomb, a foam board was installed to damp unwanted amplitude surface waves that are issued from the inlet section.

Lastly, a remark should be made on the inaccuracies in the experimental setup. During the period in which the experiments were conducted, a period of approximately two months, it was found that the material that was used to construct the geometry started to deform. As the deviations in the geometry remained less than 5 mm, corresponding to approximately 6 % of the minimum water depth, it was expected that the flow conditions were barely affected. Additional information is given in section A.5.

3.1.3. Coordinate system

Figure 3.2 illustrates the coordinate system that was used throughout the experiments. The x, y and z-axes indicate the longitudinal, lateral and vertical direction, respectively. The origin of the coordinate system was chosen at the bottom level of the upstream end of the downward slope on the right side of the flume. Furthermore, the flow velocity components corresponding to the x, y, and z-direction that were used in the representation of all measured data are expressed by u, v and w.

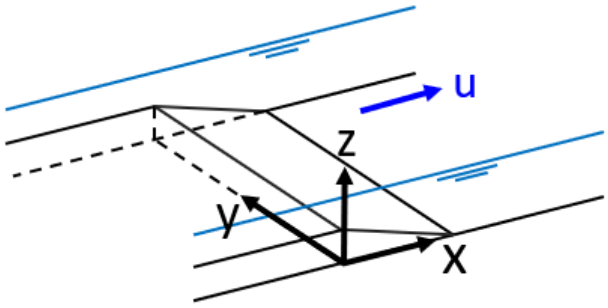

Figure 3.2: Definition of the coordinate system used in the experiments.

3.2. Scaling parameters

Four scaling parameters have been considered to correctly scale the flow conditions near the ES-SSB in the experiments. This section addresses these scaling parameters and the dissimilarities in the model.

3.2.1. Geometric scaling

A prototype and its physical scale model are geometrically similar if the ratios of all corresponding linear dimensions are equal (Vassalos, 1998). This ratio is named the scale factor λ and is given by:

$$\lambda = \frac{L_p}{L_m} \tag{3.1}$$

where L_p and L_m are characteristic length scales in the prototype (ES-SSB) and the model (experiment), respectively. As described above, several simplifications were made to simulate the flow conditions of the ES-SSB in an experiment in the shallow flume. Many of the simplifications cause that the geometry of the model deviates from the prototype and that a perfect geometric scaling cannot be applied. The remainder of this subsection will discuss the length scales that were considered in the design of the experimental setup.

- *Increase of the water depth.* In case of the inlet section of the Roompot, the water depth more than doubles from approximately 25 m at the location of the bed protection to nearly 60 m at the deepest point of a scour hole. In the experimental setup, a water depth increase of factor two was chosen, as the laboratory experiments were only intended to reproduce the relevant hydrodynamic processes and not to exactly scale the bathymetry of the ES-SSB. To prevent the flume from overtopping a maximum water level of 16 cm was maintained during the experiments. A false bottom was therefore constructed with a height a of 8.0 cm.

- *Steepness of the upstream scour slope.* A decision for the steepness of the downward slope β in the range of 1:4 to 1:6 in the experiment would scale reasonably well with observations of the scour slope near the ES-SSB, where a maximum scour slope of 1:5 over a height of 5 m is the current intervention criterion (Stoutjesdijk et al., 2012). This range of slope steepnesses was also investigated in previous experiments by Broekema (2017a).

- *Width of the jet with respect to the diameter of the large-scale gyres.* In section 2.1 of the literature study, it was explained that the eddies adjacent to the outflow downstream of the barrier grow and shrink in size throughout the tidal cycle, as depicted Figure 2.3. From initial model tests and field measurements (see for instance Broekema, 2016), can be deduced that the diameter of these eddies, or large-scale gyres, can become as large as the width of the jet flow at the maximum point of contraction. Experiments by Talstra (2011) show that for an SLE the width of the horizontal recirculation zone is approximately equal to the expansion width. Choosing a value for the ratio of the width of the upstream flow over the width of the contracting elements $B1/D$ in the experimental setup up to 1 seems therefore justified.

- *Length of the bed protection.* In the experiments, the length of the bed protection of the ES-SSB $L_{b,p}$ is represented by the distance from the lateral expansion to the upstream end of the downward slope $L_{b,m}$. Although the additional roughness of the bed protection is not taken into account in the model, the length of the bed protection is of importance as it for example influences the smearing of lateral velocity gradients in the horizontal mixing layers. In the case of the ES-SSB, the width W and bed protection length vary for each inlet section. Values for these length scales and the ratio of the width of each inlet section over its bed protection length $W/L_{b,p}$ are summarised in Table 3.1.

Inlet section	Width [m]	Bed protection length [m]	$W/L_{b,p}$ [-]
Hammen	662	650	1.02
Schaar van Roggenplaat	675	550	1.23
Roompot	1391	650	2.14

Table 3.1: Geometric properties of the inlet sections of the ES-SSB. The widths of the inlet sections and their bed protection lengths were obtained from Google Maps (2018) and Stoutjesdijk et al. (2012), respectively. The given ratio expresses the width of the inlet section over the bed protection length.

From Table 3.1 it can be concluded that in order to correctly scale the ratio of the width of the inlet section over the bed protection length, a ratio of $B1/L_{b,m}$ in the model of approximately 1 to 2 should be applied. This range has been used in the experimental setup.

3.2.2. Froude number

The Froude number expresses the ratio of the inertia force over the gravitational force and is given by:

$$Fr = \frac{U}{\sqrt{gL}} \tag{3.2}$$

in which L is a characteristic length scale that is often taken as the water depth. Froude similarity is of importance in cases where a free stream flow is induced by a gravitational force (Battjes, 2002), and should therefore be considered in a scaled model of the ES-SSB. The maximum in field Froude number corresponding to the flow at the location of the bed protection can be approximated by $Fr \approx 0.2$ (Broekema, 2017a). Since $Fr < 1$, the flow near the ES-SSB can be characterised as sub-critical.

In the preliminary experiments, various discharges were tested to examine how these would affect the flow conditions in the flume. For relatively large discharges it was found that small standing surface waves emerged at the location of the downward slope, see for example Figure B.4. These disturbances were undesired as they could affect the outcomes of the experiment. It was decided to decrease the discharge in the final experimental setup to a stage in which the standing surface waves were nearly damped out. To fairly compare the results of the experiments an average flow velocity just downstream of the inlet section $u1$ was kept at 0.38 m/s (for the experimental runs without grid elements). Assuming a constant water depth of 8.0 cm upstream of the lateral expansion, a Froude number in the model of 0.42 was maintained. This is about twice as large as the Froude number that is characteristic for the flow near the ES-SSB. A larger Froude number in the model results in an underestimation of the gravitational force with respect to the inertial force. A relatively high flow velocity in the model and associated Froude number was chosen in a trade-off with the third scaling parameter, the Reynolds number, that will be discussed in subsection 3.2.3.

3.2.3. Reynolds number

The second flow scaling parameter that is considered is the Reynolds number. The Reynolds number is used to express the ratio of the inertial force over the viscous force and is given by:

$$Re = \frac{UL}{\nu}. \tag{3.3}$$

In the case of the ES-SSB, the Reynolds number associated with the maximum flow conditions is in the order of 10^7 , when assuming a flow velocity of 2.5 m/s and a characteristic length scale of 25 m (water depth). This order of the Reynolds number can hardly be achieved in experiments with a down-scaled model. For Reynolds similarity, the flow velocity in the experiment would need to increase relative to the flow velocity of the prototype. This means that flow velocities in the flume should to be higher than at least 2.5 m/s to correctly scale the maximum flow conditions observed near the ES-SSB. The shallow flume at TU Delft cannot facilitate these magnitudes of flow velocities for sub-critical flow conditions. Compared to the prototype, a lower Reynolds number was maintained in the experiment.

In the experimental runs without grid elements, a Reynolds number of 3.0×10^4 was maintained at the location upstream of the lateral expansion, which is smaller compared to the Reynolds number associated with the maximum flow conditions near the ES-SSB. As a consequence of dissimilarity of the Reynolds number, the model overestimates the viscous force with respect to the inertial force. Although the Reynolds number in the model deviates from that of the prototype, the flow in the experiment was considered to be sufficiently turbulent.

3.2.4. Grid solidity

The grid that was used in the experiments was chosen such that its grid solidity So, described in Equation 2.12, corresponds to that of the ES-SSB ($So \approx 0.12$). Scaling by the grid solidity only did not determine the length scales of the experimental grid since the number of grid elements, the diameter of the elements D and centre-to-centre distance d could be still chosen freely. It was decided to maintain the same ratio for the diameter of the grid elements over the water depth D/h as can be observed near the ES-SSB. Assuming a diameter of the barrier's pillars of 5.5 m and a water depth at the bed protection of 20 m, the second scaling criteria for the grid was that $D/h \approx 0.275$. This finally resulted in

a grid with a diameter of the elements of 2.0 cm and a centre-to-centre distance of 17.0 cm, as shown in Figure 3.3.

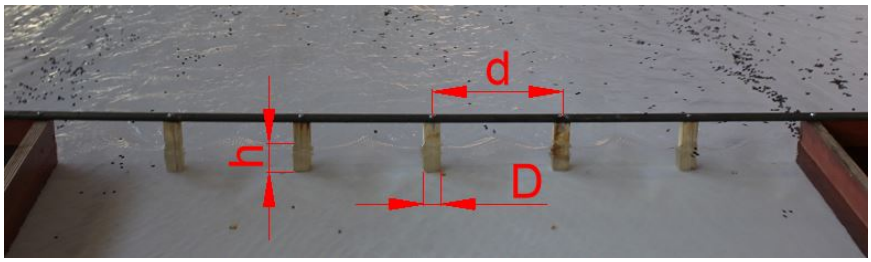

Figure 3.3: Dimensions of the grid that was used to simulate the effect of the pillars of the ES-SSB. The flow direction is from the bottom to the top of the figure.

The settings of the in- and outlet boundaries conditions in the experiments with grid elements were not adjusted from the associated runs without grid elements. The deployment of the grid elements resulted in a partial blockage of the upstream flow with $B1$, around 10 to 11 %. The water depth upstream of the grid therefore increased, resulting in a slightly lower flow velocity $u1$ upstream of the lateral expansion.

3.3. Experimental variables

This section discusses the variables that were systematically varied in the experimental runs. The decision for the range of each variable is based on the scaling parameters that were considered. Prior to each experimental run, one of the variables was adjusted to investigate its effect on vertical flow separation at the downward slope, while all other experimental variables were kept constant. An overview of the experimental variables and their range is given in Table 3.2. The preliminary experiments that are discussed in Appendix B have had an important role in the decision for the investigated variables.

Experimental variable	Symbol	Value
Downward slope	β	1:4 - 1:6
Length of the bed protection	$L_{b,m}$	0 - 2 m
Width of the contracting elements	D	0.5 - 1 m
Grid solidity	So	0.12

Table 3.2: Overview of the experimental variables.

The following variables were varied in the experimental setup:

1. *Downward slope.* The first variable that is considered in the experimental setup is the steepness of the downward slope. Initially, experiments started with a 1:4 slope. As the majority of these experimental runs resulted in vertical flow separation on the downward slope, it was decided to perform additional experiments with a slope steepness of 1:6 . The tipping point between vertical separation and attachment of the flow is considered to be important, as both processes can be observed in the scour holes near the ES-SSB during a tidal cycle. It was expected that for a milder slope vertical flow attachment would be more likely to occur due to a decrease of the adverse pressure gradient that normally causes flow separation.

2. *Location of the lateral expansion.* Increasing the distance between the contracting elements and the downward slope $L_{b,m}$ results in wider horizontal mixing layers above the slope. As explained in subsection 2.3.3, the core of a jet is decelerated in downstream direction while the ambient fluid accelerates. It was therefore expected that for larger distances $L_{b,m}$ the lateral velocity gradient at the location of the downward slope decreases due to an increase in lateral mixing. Figure 3.4 gives an impression of the expected change in the lateral velocity gradients along three transverse cross-sections. In the experiments the lateral expansion was positioned at x=0.0 m, x=-1.0 m and x=-2.0 m, respectively.

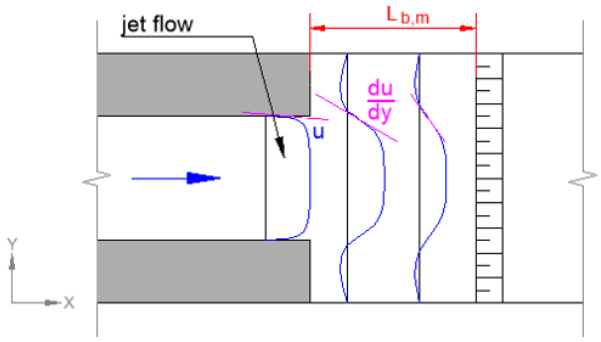

Figure 3.4: Qualitative sketch of the streamwise flow velocity of the jet flow along three transverse cross-sections (blue). The lateral velocity gradient is expected to decreases for increasing distance from the lateral expansion (magenta).

3. *Width of the contracting elements* D. To study the importance of the width of the jet flow with respect to the width of the mixing layers, experiments have been performed with several upstream flow widths $B1$, see Figure 3.5. To investigate the influence of the width of the jet, contracting elements with a width D of 0.5 m, 0.75 m and 1.0 m have been used. During the preliminary experiments, it was found that at the location where the mixing layers reach the downward slope the flow remained vertically attached to the slope. It was therefore thought that decreasing the width of the jet centre with respect to the width of the mixing layers could possibly result in flow attachment along the centerline of the downward slope.

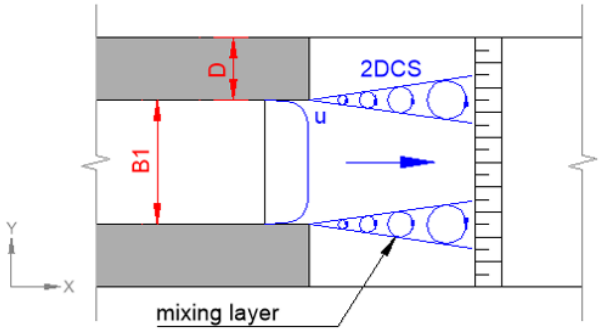

Figure 3.5: Qualitative sketch of the importance of the width of the jet flow with respect to the width of the mixing layers.

4. *Grid elements.* Finally, the effect of grid turbulence generated by the barrier's pillars was investigated in the experiments. It was done by applying an array of square shaped elements in the flow. The grid elements were made of wooden beams that were attached to a metal strip, such that they could easily be added and removed from the experimental setup. In all experimental runs in which grid turbulence was investigated, the grid elements were positioned at the location of the lateral expansion. Figure 3.3 shows the grid that was used. The grid elements had a width of 2.0 cm and a centre-to-centre distance of 17.0 cm. Depending on the upstream flow width, the grid varied varied between 5 and 11 elements. The corresponding blockage of the upstream flow width ranged from 10.0 to 11.0 %.

3.4. Description of the experimental runs

An overview of all experimental runs and the data that was collected is summarised in Table 3.3. Run numbers 1, 2, 3 and 22 are the reference cases in which no contracting elements were installed in the flume. For the remaining experiments, the structure of the name partially informs about the setup that was used. The first digit of the run name indicates the steepness of the downward slope in the experimental run: number 1 represents a slope of 1:4 and number 2 a slope of 1:6. The second digit of the name explains if grid turbulence is included or not. An even number indicates no effect of grid

turbulence whereas for uneven numbers grid turbulence is included. In the case of grid turbulence, the grid elements were always positioned at the location of the lateral expansion. The third digit indicates the position of the lateral expansion. The numbers 0, 1 and 2 correspond to the location of the lateral expansion at x=0.0 m, x=-1.0 m and x=-2.0 m, respectively. For the upstream width, $B1$ the reader is referred to Table 3.3 as this is not included in the name of the run.

As an example, Run 2.4.3 represents an experiment with a 1:6 downward slope in which the effect of grid turbulence is not included and where the lateral expansion is located at 2 m upstream of the downward slope.

#	Name	Slope	Lateral expansion		Grid	Discharge	Data collection		
			Width [m]	Position x [m]		[l/s]	Video	PIV	ADV
1	Run 1.1.1	1:4	N/A	N/A	No	40	X	X	
2	Run 1.1.2	1:4	N/A	N/A	No	60	X	X	
3	Run 1.1.3	1:4	N/A	N/A	No	80	X	X	X
4	Run 1.4.1	1:4	B1=1.5	0.0	No	45	X	X	X
5	Run 1.4.2	1:4	B1=1.5	-1.0	No	45	X	X	X
6	Run 1.4.3	1:4	B1=1.5	-2.0	No	45	X	X	X
7	Run 1.5.1	1:4	B1=1.5	0.0	Yes	45	X	X	X
8	Run 1.5.2	1:4	B1=1.5	-1.0	Yes	45	X	X	X
9	Run 1.5.3	1:4	B1=1.5	-2.0	Yes	45	X	X	X
10	Run 1.6.1	1:4	B1=2.0	0.0	No	60		X	X
11	Run 1.6.2	1:4	B1=2.0	-1.0	No	60		X	X
12	Run 1.6.3	1:4	B1=2.0	-2.0	No	60		X	X
13	Run 1.7.1	1:4	B1=2.0	0.0	Yes	60		X	X
14	Run 1.7.2	1:4	B1=2.0	-1.0	Yes	60		X	X
15	Run 1.7.3	1:4	B1=2.0	-2.0	Yes	60		X	X
16	Run 1.8.1	1:4	B1=1.0	0.0	No	30		X	X
17	Run 1.8.2	1:4	B1=1.0	-1.0	No	30		X	X
18	Run 1.8.3	1:4	B1=1.0	-2.0	No	30		X	X
19	Run 1.9.1	1:4	B1=1.0	0.0	Yes	30		X	X
20	Run 1.9.2	1:4	B1=1.0	-1.0	Yes	30		X	X
21	Run 1.9.3	1:4	B1=1.0	-2.0	Yes	30		X	X
22	Run 2.1.1	1:6	N/A	N/A	No	80	X	X	X
23	Run 2.2.1	1:6	B1=1.5	0.0	No	45	X	X	X
24	Run 2.2.2	1:6	B1=1.5	-1.0	No	45	X	X	X
25	Run 2.2.3	1:6	B1=1.5	-2.0	No	45	X	X	X
26	Run 2.3.1	1:6	B1=1.5	0.0	Yes	45	X	X	X
27	Run 2.3.2	1:6	B1=1.5	-1.0	Yes	45	X	X	X
28	Run 2.3.3	1:6	B1=1.5	-2.0	Yes	45	X	X	X
29	Run 2.4.1	1:6	B1=1.0	0.0	No	30	X	X	X
30	Run 2.4.2	1:6	B1=1.0	-1.0	No	30	X	X	X
31	Run 2.4.3	1:6	B1=1.0	-2.0	No	30	X	X	X
32	Run 2.5.1	1:6	B1=1.0	0.0	Yes	30	X	X	X
33	Run 2.5.2	1:6	B1=1.0	-1.0	Yes	30	X	X	X
34	Run 2.5.3	1:6	B1=1.0	-2.0	Yes	30	X	X	X

Table 3.3: Description of the experimental runs and the collected data.

3.5. Measurement techniques

Several measurement techniques have been used to qualitatively and quantitatively describe the flow in the experiments. The measurements mainly focused on the following flow characteristics: the large-scale gyre downstream of the horizontal contraction, flow attachment or the formation of a recirculation zone at the downstream slope, 2DCS in the mixing layer and three-dimensional turbulence. The first step was to identify the present flow structures by inserting dye at various locations in the flume. Then, PIV measurements were conducted to quantify the surface velocity. At last, acoustic Doppler velocimetry (ADV) measurements have been performed to obtain detailed information on all velocity components of the flow field.

3.5.1. Visualisation of the flow

The first step of the experiments was to visualise the presence of flow structures downstream of the lateral expansion by injecting coloured dye. These qualitative measurements helped to identify flow processes such as vertical attachment or separation of the flow, the direction of the jet flow, the growth of eddies in the mixing layer and vortex merging. Turbulence caused the dye to diffuse such that only flow processes a couple of meters downstream the location of injection could be visualised. In addition to the injection of dye, sinking and floating particles have been used to visualise the direction of the flow. Sinking particles were especially useful to determine if vertical flow separation occurred since the particles would then remain in the recirculation cell on the downward slope for a short period of time.

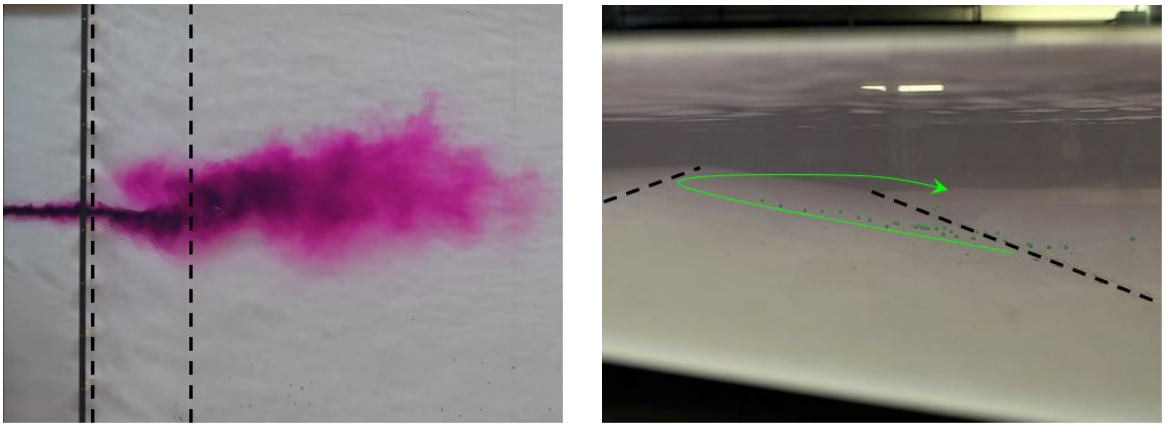

(a) (b)

Figure 3.6: Flow visualisation: (a) Dye injection (Run 1.5.1) and (b) Sinking particle seeding (Run 2.1.1). The dashed black lines in the sub-figures indicate the position of the downward slope. The green arrow shows the direction of the sinking particles.

3.5.2. Particle image velocimetry

In this master thesis, the open-source tool PIVlab version 1.42 (Thielicke, W. and Stamhuis, E. J., 2014) for MATLAB has been used to quantitatively describe the surface flow in the laboratory experiments. This subsection first addresses the measurement setup that was used for the PIV measurements. Then the main steps of the PIV analysis are discussed, namely: image pre-processing, image evaluation and data post-processing. More information on PIV can be found in Appendix C.

Measurement setup

For the PIV measurements, a *Samsung NX1* digital camera equipped with a *16-50 mm OIS* lens was used. The camera was mounted on a movable frame 2.56 m above the bottom of the flume. Furthermore, the camera was directed exactly vertically downwards, i.e. perpendicular to flume's bottom. During recording, ceiling lights above the flume were turned off to prevent reflection from the water surface. No other additional light sources than daylight were used to illuminate the flume.

Depending on the region of interest (ROI) in each experimental run, three to eight camera positions were used to determine the mean surface velocity. The footage therefore covers a total length of the flume between 5.0 and 12.5 m. In all experiments, the ROI at least covered the area from the location

of the lateral expansion to approximately 2 m downstream of the downward slope. Neighbouring camera positions were given an overlap of 46.0 cm which corresponds to approximately 23 % of the width of the camera reach, see Figure 3.7. For each camera position, a video was recorded of at least 6 minutes. The camera was set to record with a resolution of 1920×1080 pixels at 120 frames per second (fps). The open source software *Free Video to JPG Converter* of Digital Wave Ltd was used to extract individual images from the videos.

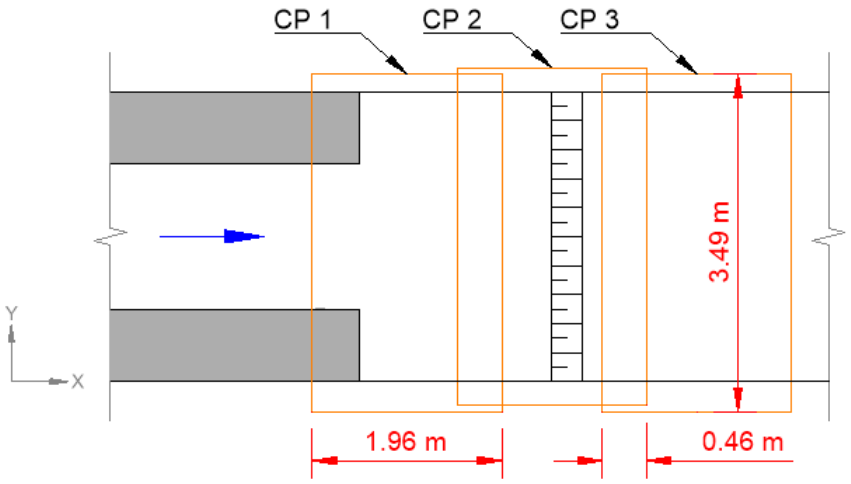

Figure 3.7: Multiple camera positions were used to cover the region of interest. The orange boxes indicate the reach of three camera positions: CP 1, CP 2 and CP 3. The red dimensions indicate the reach and overlap of the camera positions.

For the PIV measurements black polypropylene tracer particles with a diameter of 3 to 4 mm were used. In order to avoid peak locking-effects, Weitbrecht et al. (2002) suggest that the diameter of the particles should be covered by at least 1.5 times the pixel size. Calibration images showed that this criterion was indeed met as 1 pixel corresponded to approximately 1.8×10^{-3} m. For the purpose of this master thesis, 6 mm thick white coloured HPL plates were installed over the entire length of the flume's bottom to increase the contrast with the tracer particles. The black tracer particles gave a large contrast with the white HPL bottom and were therefore highly suitable for this measurement technique.

For the PIV measurement, a dispenser was used to equally distribute tracer particles along the width of the flume. Also, a sieve was placed in the outlet section to retrieve tracer particles. Additional information on the experimental setup can be found in Appendix A.

The remainder of this subsection will discuss how the image pre-processing, image evaluation and data post-processing were performed to determine the surface velocity with PIVlab.

Image pre-processing

Free Video to JPG Converter of Digital Wave Ltd was used to extract 10 fps from the individual videos. With a recording time of 6 minutes a single camera position contained at least 3600 images to compute the surface flow velocity from. Figure 3.8 depicts the editing steps that performed in the pre-processing of the images. The *Image Processing Toolbox* of MATLAB was used to edit the footage. As a first step, the raw extracted images were rotated 90 ° anti-clockwise to have the flow directed from left to right (Figure 3.8a). Then, the raw footage was converted to grayscale to increase to the contrast of the tracer particles with the background and to reduce the size of the image (Figure 3.8b). Lastly, the background was removed of all images. This was done by calculating an average image of all grayscale images and subsequently subtracting this from each individual image (Figure 3.8c). The remaining images show the tracer particles as white dots on a black background. These images were used in the second step of the PIV analysis: the image evaluation.

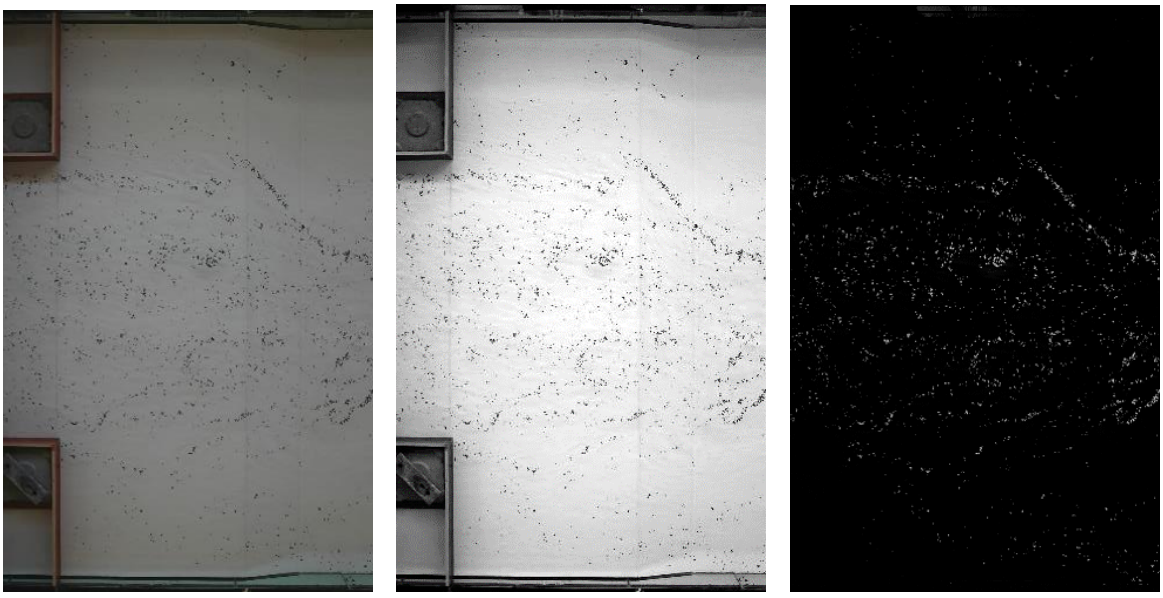

(a) (b) (c)

Figure 3.8: PIV image pro-processing steps (a) raw image extracted from the video, (b) image converted to grayscale and (c) image with average grayscale image subtracted. (Run 1.4.2)

Lens distortion of the camera was not taken into account in the pre-processing of the images. Since the camera was positioned relatively high above the flume, straight lines in the experimental setup also appeared to be straight in the footage. An advantage of neglecting the camera's lens distortion was that the computational time could be reduced. In section C.2 of Appendix C an example is given of a correction of the lens distortion.

Image evaluation

In the image evaluation step, small sub-images (named interrogation areas) of consecutive images pair are cross-correlated to determine the instantaneous surface velocity field of the ROI. To obtain the surface velocity field, a cross-correlation algorithm is used to derive the most probable displacement of the tracer particles in the interrogation areas. The statistical pattern matching technique that is used in the PIV analysis is the discrete cross-correlation function which is defined as:

$$C(m,n) = \sum_{i}\sum_{j} A(i,j)B(i-m,j-n) \tag{3.4}$$

where A and B are the interrogation areas in image A and image B, respectively (Huang et al., 1997). The maximum peak location in the correlation matrix $C(m,n)$ gives the most probable particle displacement of the tracer particles. With the time interval between the images known, the PIV analysis results in a velocity vector for each interrogation area of consecutive images.

Two approaches can be used to solve Equation 3.4: direct cross-correlation (DCC) and discrete Fourier transform (DFT). DCC and DFT compute the correlation matrix in the spatial and frequency domain, respectively. By default, PIVlab is set to DFT in which multiple passes can be used to accurately determine the displacement of the tracer particles in an image pair. The passes have different sizes such that particle displacement is first determined for a relatively large interrogation area, and subsequently for smaller interrogations windows to increase the vector resolution. An advantage of the DFT algorithm is that the interrogations areas of subsequent passes are not only displaced but that also deformation is taken into account.

Another important step in the image evaluation is the method that is used for the peak finding of the correlation matrix. In general, the peak location of the correlation matrix is found by fitting a Gaussian function to the integer intensity distribution. PIVlab includes two methods to determine the intensity

peak of the correlation matrix at sub-pixel accuracy: a 2×3-point fit that uses the directly adjacent horizontal and vertical pixels, and a 9-point fit. For all PIV data, the 2×3-point fit was used to determine the peak of the correlation matrix. For more information on the cross-correlation algorithms and peak finding methods implemented in PIVlab, the reader is referred to the paper of Thielicke, W. and Stamhuis, E. J. (2014).

The ROI of each camera position included the full width and part of the height of recorded footage, as depicted in Figure 3.9. An object mask was added to the camera positions which included contracting elements and grid elements to exclude these areas from the PIV analysis.

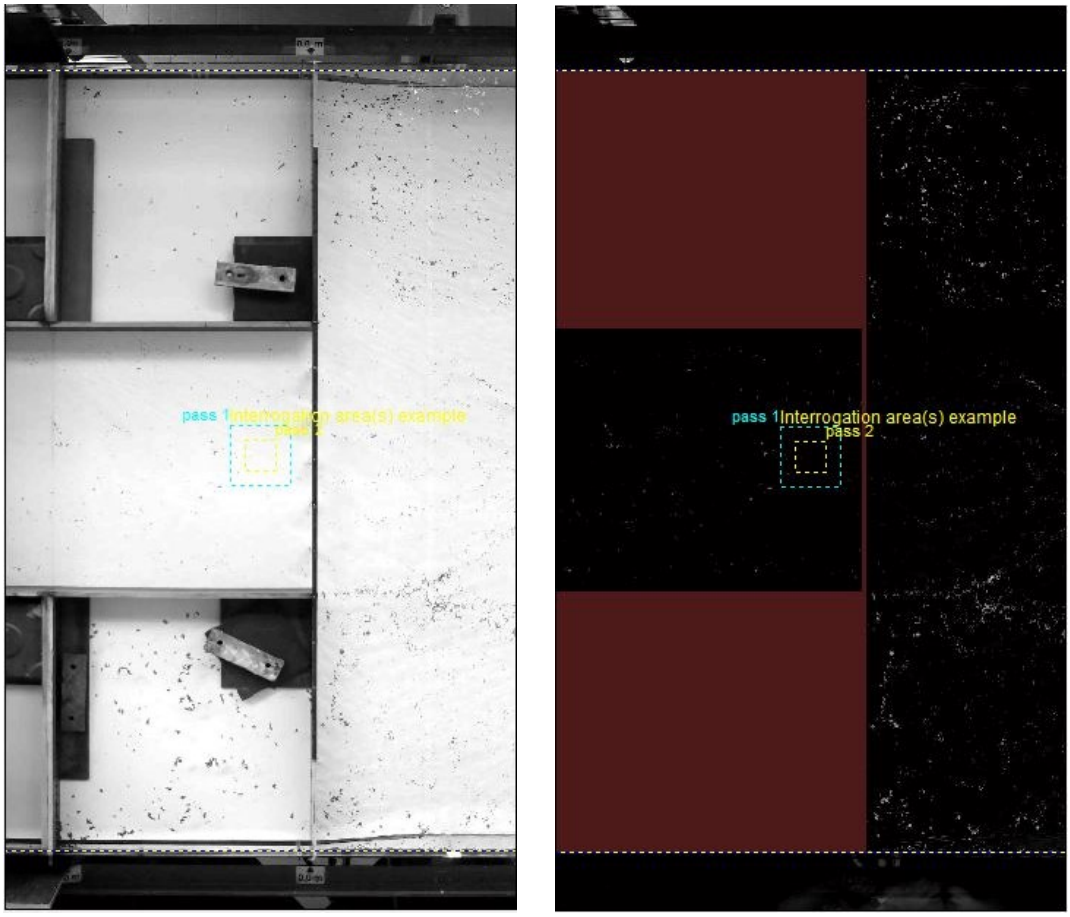

Figure 3.9: Screen shot of the used ROI, object mask and interrogation areas in PIVlab. (a) The grayscale image to determine the ROI and the object mask. (b) The ROI and object mask applied to a fully pre-processed image. The white dashed lines show the vertical extent of the ROI. The blue and yellow dashed squares indicated the size of pass 1 and pass 2, respectively. The brown area presents the object mask that was used to exclude areas from the analysis. (Camera position 2 of Run 2.5.1)

Assuming an upper limit for the flow velocity in the flume of 0.5 m/s, the maximum displacement of the tracer particles in a pair of consecutive images would be around 28 pixels. Choosing a pass size of 128×128 for pass 1 meets the criterion stated by Thielicke, W. and Stamhuis, E. J. (2014) to keep the particle displacement smaller than one quarter of the interrogation area. This is advised to prevent background noise in the correlation matrix. To obtain a higher vector resolution for the velocity field, a second pass was included in the evaluation step. Pass 2 included an interrogation area of 64×64 pixels. Finally, the velocity field of a single camera position without objects could be described by a matrix of 32×50 velocity vectors.

Data post-processing

In the data post-processing step, the PIV data of the individual camera positions were filtered and merged. Two filters have been used to post-process the data sets. First of all, a filter was applied

with a manually set upper and lower limit for the measured u and v velocity components. With this first filter, unrealistic velocity vectors were eliminated from the data sets. Details of the used threshold velocities are summarised in Table 3.4, where the subscripts min and max indicate the minimum and maximum allowed velocities.

Velocity limit	Velocity threshold [m/s]
u_{min}	-0.5
u_{max}	0.8
v_{min}	-0.6
v_{max}	0.6

Table 3.4: Manually set velocity limits to filter outliers from the PIV data.

To visualise the effect of the first filter, Figure 3.10 shows an example of a scatter plot of the flow velocity data obtained from the first 10 image pairs of camera position 1 of Run 1.4.2. It can be seen that only a small number of data points is eliminated from the data set.

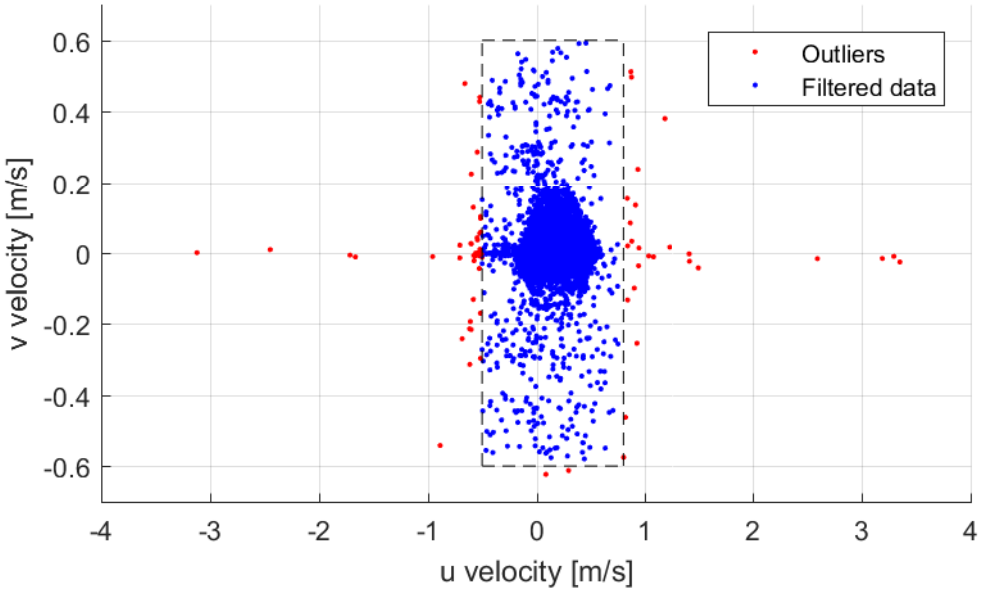

Figure 3.10: Example of PIV data post-processing for the data set of 10 images pairs of the most upstream camera postition of Run 1.4.2. The black dashed rectangle indicates the velocity thresholds.

As a jet flow contains a (strongly) inhomogeneous flow field, including both high and low velocities regions, filtering the obtained PIV data based on velocity thresholds alone does not eliminate a great number of outliers. Especially, outliers that just fall within the domain of the chosen velocity limits can still significantly affect the flow field in low-velocity regions. Therefore, a second more universal outlier detection method named the normalised median test was applied. The normalised median test adapts to the local flow situations. This inbuilt PIVlab filter proposed by Westerweel and Scarano (2005) is based on the velocity fluctuations and median of a 3×3 neighbourhood of data points. The median of the velocity fluctuation is used as normalisation for a more classical median test (Thielicke, W. and Stamhuis, E. J., 2014).

At last, missing data points by the removal of outliers were replaced by two-dimensional linear interpolation. The filtered and interpolated data sets of all individual camera positions were merged to obtain a complete image of the flow field.

Measurement inaccuracies

During the experiments, several processes were identified that caused errors in the measured surface velocity flow field. Inaccuracies in the PIV data result from:

1. *Poor distribution of the tracer particles.* First of all, inaccuracies in the surface flow field arise from regions that were poorly seeded, as for example depicted in Figure 3.11. Insufficient velocity data in these regions and interpolation of the missing data points result in an erroneous representation of the surface flow by PIV. Difficulties in the distribution of tracer particles were caused by wall boundary separation along the flume's side walls and upwelling in eddies. Also, it was found that for experiments that included grid turbulence, the wakes downstream of the grid elements barely contained any tracer particles.

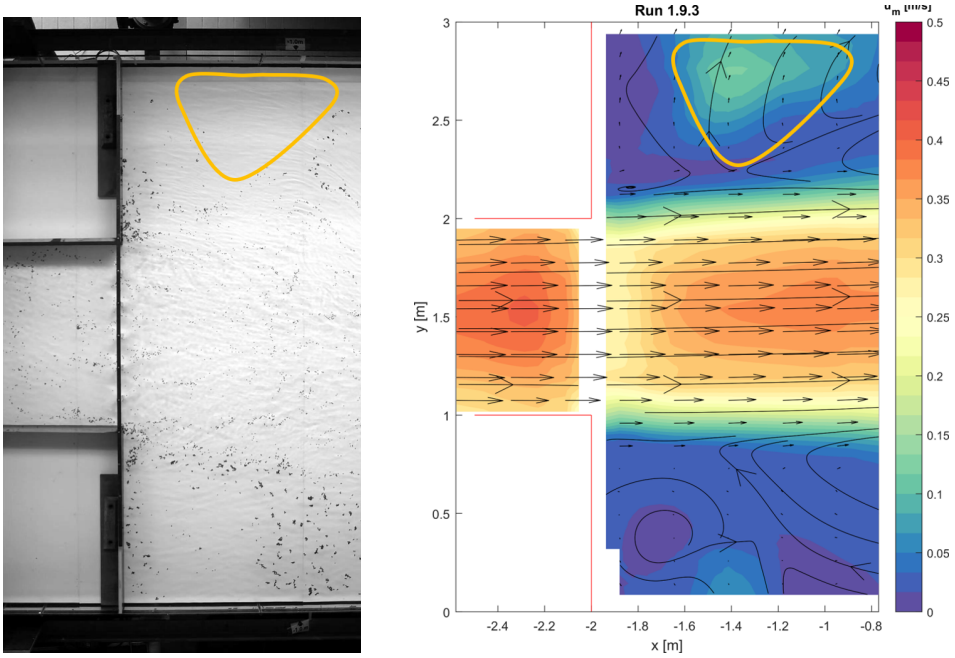

(a) (b)

Figure 3.11: Inaccuracies of PIV by poorly seeding of the water surface. (a) No tracer particles are present in the orange outlined area. (b) Erroneous representation of the mean surface flow in a region with insufficient tracer particles. (Run 1.9.3)

2. *No detection of the tracer particles.* It should be noted that at the location of the grid no surface velocity data is available as the tracer particles moved behind the metal strip to which the grid elements were attached. This region was excluded from the PIV analysis as the algorithm could not possibly determine a correct displacement of the tracer particles, see Figure 3.11b.

3. *Size of the interrogation area with respect to the turbulence length scales.* For the experiments that included the effect of grid turbulence, it was found that the measured surface flow field directly downstream of the grid deviated from visual observations. For example, Figure 3.11b shows a nearly uniform flow velocity over the width of the jet flow directly downstream of the grid, whereas visual inspection revealed that wake structures were present in the lee of all grid elements. Besides the absence of tracer particles in these wakes, inaccuracies in the PIV measurements for experiments that include grid turbulence result from the size of the interrogation area. As the size of the smallest interrogation window is relatively large compared to the turbulence length scales that were observed in the vicinity of the grid elements, the PIV algorithm cannot possibly determine the surface flow near the grid correctly. With the used PIV settings a single velocity vector was computed for an area of 6.0×6.0 cm^2, while the vortices that were shed from the grid elements can be described by a characteristic length scale approximately equal to the width of the grid elements ($L \approx$2.0 cm). Figure 3.12a presents a schematic of the size of the wake structures and the area that is used to compute a single velocity vector (purple square).

4. *Submergence of tracer particles.* In the experimental runs in which the grid elements were positioned directly upstream of the downward slope, it was observed that tracer particles submerged, see Figure 3.12b. The local submergence of the tracer particles resulted from a strong downward flow near the slope. As the submerged particles were still visible in the footage, the PIV algorithm used particle displacements that were not representative for the surface flow.

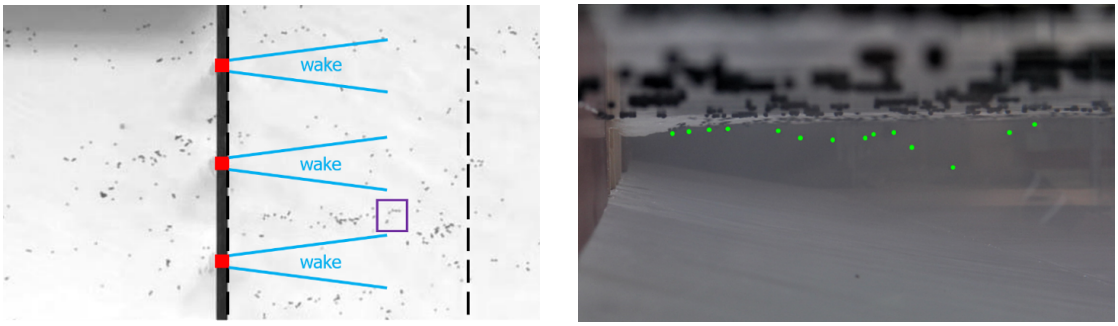

(a) (b)

Figure 3.12: Top and side view of Run 2.5.1 during the PIV measurements. (a) The area used to compute a single velocity vector (purple square) and the wake structures (blue) that formed downstream of the grid elements (red). The black dashed lines indicate the location of the downward slope. (b) Submergence of tracer particles (green dots) at the location of the slope. The photograph was taken at the side of the flume, below the water surface.

As the PIV measurement technique was not suitable to correctly determine the flow conditions directly downstream of the grid, it was decided to exclude erroneous data from all subsequent analyses. Data points within a downstream distance of four initial water depths from the grid are assumed to be incorrect and will not be used or displayed in the remainder of this master thesis.

3.5.3. Acoustic Doppler velocimetry

Acoustic Doppler velocimetry (ADV) is a measurement technique that can be used to determine all orthogonal velocity components at a specific point in the flow. ADV is based on the Doppler frequency shift of emitted acoustic signals after reflection by small sound-scattering particles that are present in the fluid (Lane et al., 1998). Assuming that these small particles in the fluid have the same velocity as the flow, the shift of the frequency is proportional to the flow velocity.

A *Vectrino 2D-3D Sidelooking, fixed stem* of Nortek was used to perform the ADV measurements. The device has a sampling volume with a diameter of 6 mm that is located at 50 mm from the probe. For the measurements, the device's maximum sampling rate of 25 Hz was used. As there were insufficient sound-scattering particles in the water, tiny oxygen bubbles were added to the flow just upstream of the probe. The oxygen bubbles were generated via electrolysis with a frame of thin platinum wires (cathode) and a metal bar (anode) to complete the electrical circuit. More information on the experimental setup of the ADV measurements can be found in Appendix A.

Data acquisition

ADV measurements were performed to quantitatively describe the flow conditions near the downward slope. For all experiments, ADV measurements were conducted along a longitudinal transect in the centerline of the flume and at several points in the centre of the dominant horizontal mixing layer. ADV measurement were taken at x=-0.10 m, halfway the downward slope and 10 cm downstream of the slope. As the y-coordinates of the centre of the mixing layer varied in each experimental run, the exact locations of these measurement points was first determined by dye injection or the PIV results. For some experiments, more measurement points were used to obtain detailed information on certain hydrodynamic processes. As an example, Figure 3.13 shows the locations of the measurement points of Run 1.6.1.

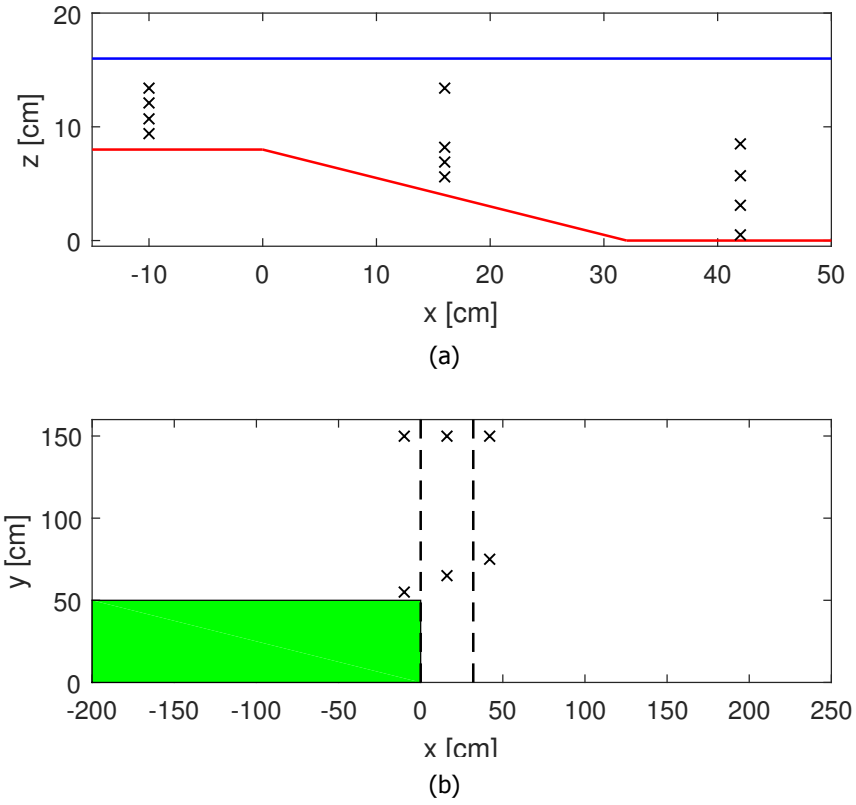

Figure 3.13: Overview of the positions of ADV measurements for Run 1.6.1. (a) Side view indicating the xz positions of the measurement point. (b) Top view showing the xy locations of the measurement point. The blue, red and black dashed lines indicate the water surface level, flume's bathymetry and the position of the downward slope, respectively. The green box shows the position of one contracting element.

Based on Taylor's hypothesis, also known as the frozen turbulence approximation, it was decided to record data for 5 minutes per measurement point. Assuming a characteristic length scale of the largest eddies of 1 m and a mean streamwise velocity downstream of the downward slope of approximately 0.2 m/s, the time for a single vortex to pass a fixed point of observations equals 5 s. The output signal of the ADV measurements will therefore contain approximately 60 times the largest eddies size. This is assumed to be sufficient for a statistical analysis.

Data post-processing

Outliers in the ADV data were detected and removed by the inbuilt Hampel identifier of MATLAB (Pearson, 2005). The *Hampel*-function requires two input parameters to filter the ADV data: the half-width window size K and the threshold parameter t_{ADV}. For each data point, the filter computes the median of a window including the considered data point and its neighbouring data points (K on each side of the sample). Furthermore, the filter calculates the median absolute deviation (MAD) of the data points in the measurement window. If the considered data point deviates more than t_{ADV} times the MAD from the window's median, then the data point is treated as an outlier and replaced by the median of that window. In the data post-processing, a half-width window of ten data points and a threshold parameter of 3 were used to filter the ADV data. Figure 3.14 depicts the functioning of the Hampel filter for one of the measurement points of Run 1.4.1.

Measurement inaccuracies

Inaccuracies of the ADV measurement technique result from:

1. Disturbances of the flow by the measurement device and the frame that supports the wire mesh, as depicted in Figure 3.15 for velocity measurements near the downward slope.

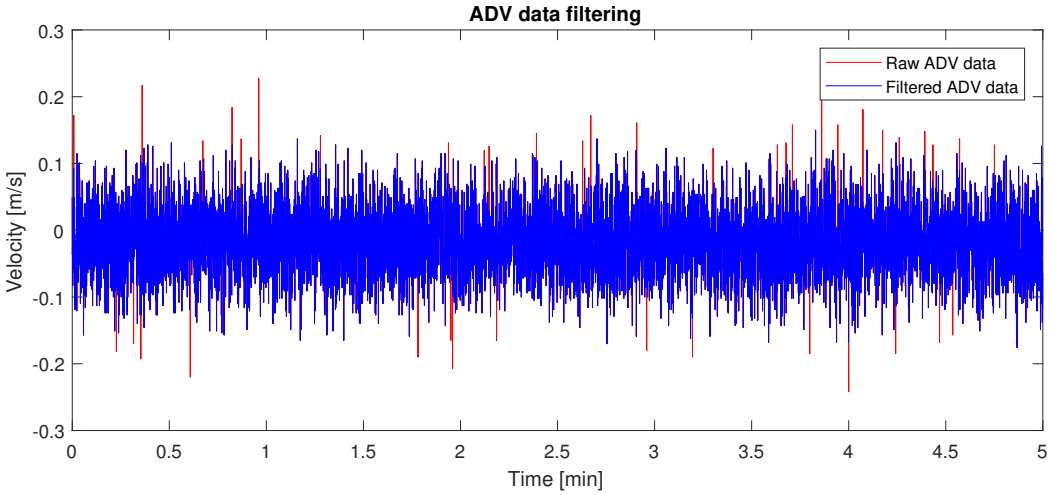

Figure 3.14: Data filtering for measurement point (x,y,z)=(0.160; 1.500; 0.069) of Run 1.4.1.

2. The tiny air bubbles that are generated by the wire mesh have the tendency of to move upwards. As illustrate in Figure 3.15, the tiny air bubbles move towards the water surface and thus do not correctly follow the movement of the fluid.

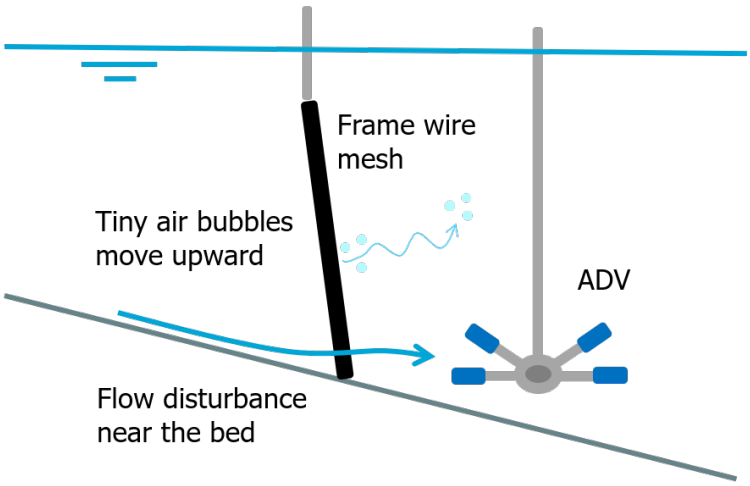

Figure 3.15: Longitudinal schematic representation of ADV near the downward slope. Inaccuracies of ADV measurements results from disturbance in near-bottom flow by the frame of the wire mesh and the tendency of tiny air bubbles to move upward.

3. The incorrect positioning of the measurement device such that all velocity components correspond to the longitudinal, lateral and vertical direction of the flume as defined in Figure 3.2.

4

Results

This chapter presents the results that were obtained from the laboratory experiments that were conducted in the Fluid Mechanics Laboratory at Delft University of Technology.

A possible explanation for the attachment of the flow in the scour holes of the ES-SSB follows from conservation of potential vorticity. Through conservation of potential vorticity, it can be shown that a base flow with a lateral velocity gradient that is subjected to a depth increase may experience an additional acceleration. In Broekema (2017a) it is hypothesised that when this acceleration is sufficiently large, it can counteract the effect of the adverse pressure gradient that causes the boundary layer to separate from the bed. The flow then remains vertically attached to the bed. This hypothesis will be further investigated through the experiments that are conducted for this master thesis.

4.1. Vertical flow structure

Near the ES-SSB, a deceleration of the flow results from a sudden depth increase caused by the scour holes at the downstream end of the bed protection. Depending on the stage of the tidal cycle, vertical flow separation or attachment can be observed at the upstream slope of the scour hole. It is expected that the vertical flow state largely affects the bed shear stress and thereby the development of the scour hole.

This section addresses the vertical structure of the flow that was observed in the laboratory experiments. Two types of vertical flow states near the downward slope can be distinguished from the experiments that contained a lateral expansion: vertical flow attachment along the entire width of the jet flow and vertical flow separation of the jet centre. A schematic overview of these vertical flow states is depicted in Figure 4.1. In Figure 4.1, ZOAF and ZOSF represent a zone of attached flow and a zone of separated flow, respectively.

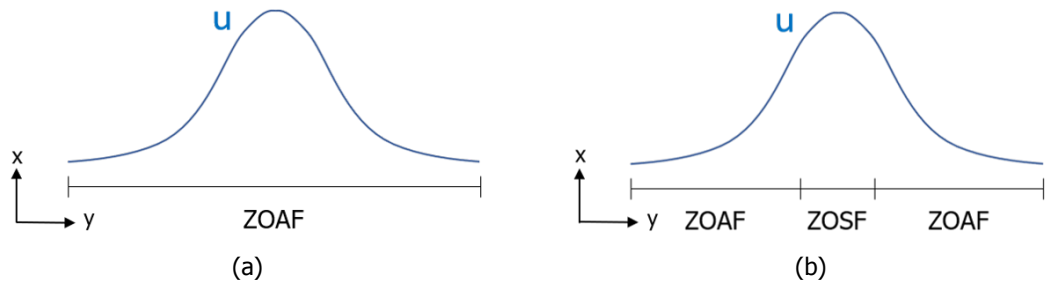

Figure 4.1: Schematic overview of the observed vertical flow states at the location of the downward slope: (a) Experiments with vertical flow attachment along the full width of the jet (b) Experiments with vertical flow separation in the jet centre and vertical flow attachment in the horizontal shear layers.

4.1.1. Experiments with vertical flow attachment of the jet flow

Vertical flow attachment at the downward slope over the full width of the jet was visually observed in ten of the experiments that were performed in the shallow water flume. The determination of vertical flow attachment or separation in an experimental run is based on dye injection and the seeding of sinking particles. An example of vertical flow attachment of the jet flow based on a photo series of dye injection is shown in Figure 4.2. It can be seen that the dye follows the contours of the bottom without overshooting a region along the downward slope. This indicates that no recirculation zone is present that is characteristic for vertically separating flows.

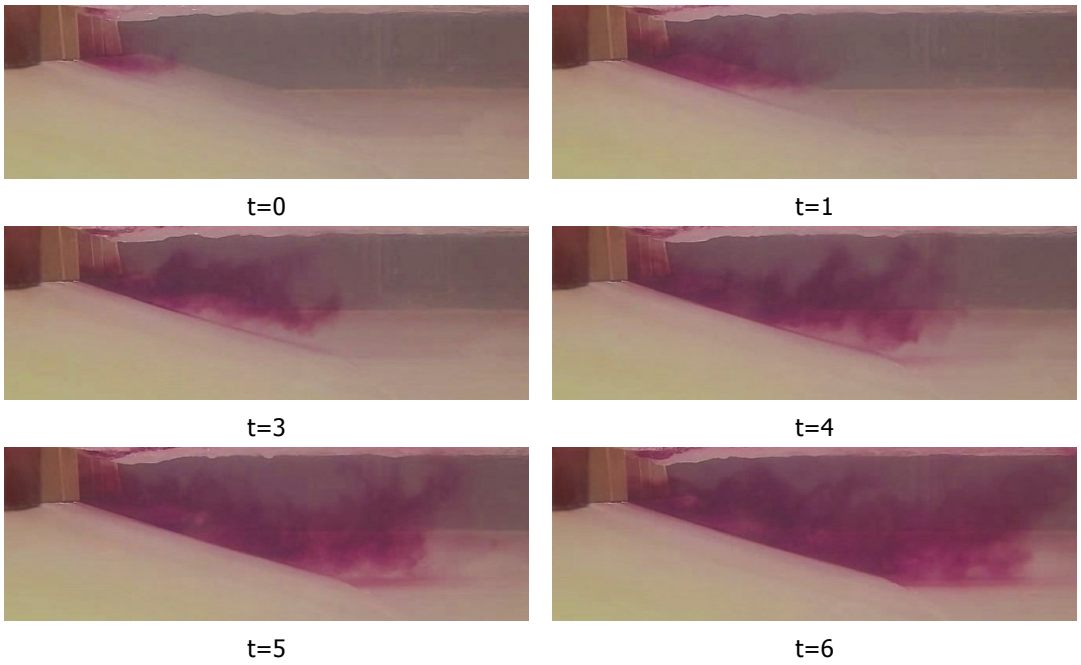

Figure 4.2: Photo series of vertical flow attachment of the jet centre at the downward slope. The interval between each time steps equals 0.2 s. (Run 1.9.1: slope 1:4, B1=1.0 m, $L_{b,m}$=0.0 m and with grid)

In addition, the vertical flow state near the downward slope in an experiment was based on the movement of sinking particles. In the case of vertical flow attachment, the sinking particles would at all times follow the bed and directly move past the downward slope indicating that no vertical recirculation zone is present at the slope. Lastly, vertical flow attachment was quantitatively demonstrated by the ADV measurements. For vertically attached flows, the measurement points closest to the slope are all directed in downstream direction and show relatively high flow velocities. An example of the ADV measurements that is representative for experiments with vertical flow attachment of the jet centre is given in Figure 4.3. An important characteristic of vertical flow attachment, that can also be noticed in Figure 4.3, is that flow velocity is approximately uniform over the depth.

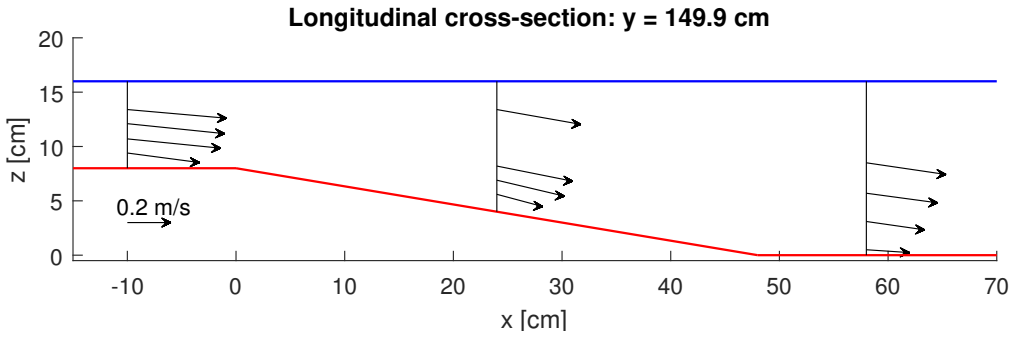

Figure 4.3: ADV measurements indicating vertical flow attachment in the jet centre. (Run 2.5.2: slope 1:6, B1=1.0 m, $L_{b,m}$=1.0 m and with grid)

The experiments in which flow attachment of the centre of the jet was observed are divided into two categories, as it is expected that there are different mechanisms that cause flow attachment on the downward slope. In the remainder of this thesis, reference is made to two flow attachment categories:

- *Flow attachment: Category 1.* This category includes all experiments with a 1:6 downward slope and an initial upstream flow width $B1$ of 1.0 m. The similarity between these experimental runs is the ratio of the width of the upstream flow over the width of the contracting elements $B1/D$ that is equal to 1. Category 1 includes Run 2.4.1, Run 2.4.2, Run 2.4.3, Run 2.5.2 and Run 2.5.3. For an overview of the experimental runs, the reader is referred to Table 3.3.
- *Flow attachment: Category 2.* The second category includes all experiments include the effect of grid turbulence where the elements are located directly upstream of the downward slope, i.e. at the location x=0 m. Category 2 includes Run 1.5.1, Run 1.7.1, Run 1.9.1, Run 2.3.3 and Run 2.5.1, see Table 3.3.

The main focus of this master thesis will be on the experiments described in category 1, as it is expected that the flow attachment in these runs results from an additional acceleration through conservation of potential vorticity. Remarkable is that all experimental runs in which grid elements were located directly upstream of the downward slope resulted in vertical flow attachment, even though the majority of the corresponding experimental runs without grid turbulence resulted in vertical flow separation of the jet centre. It is therefore expected that a different generation mechanism causes vertical flow attachment of the jet centre. Possible generation mechanisms for vertical flow attachment of the jet centre in experiments assigned to category 2 will be further discussed in subsection 4.3.3. The flow attachment observed in category 2 is not likely to correctly simulate the flow conditions at the ES-SSB, as the pillars of the barrier are located at a certain distance from the scour hole.

4.1.2. Experiments with vertical flow separation of the jet centre

Vertical flow separation of the jet centre was observed in the majority of the experimental runs. This was concluded from visual observations in which dye and sinking particles remained in a vertical recirculation zone at the centre of the downward slope, as for example shown in Figure 4.4. Figure 4.4 clearly shows that the dye shoots over a region at the downstream end of the slope. Also, the photo series shows the development of disturbances in the mixing layer that originates from the upstream end of the slope.

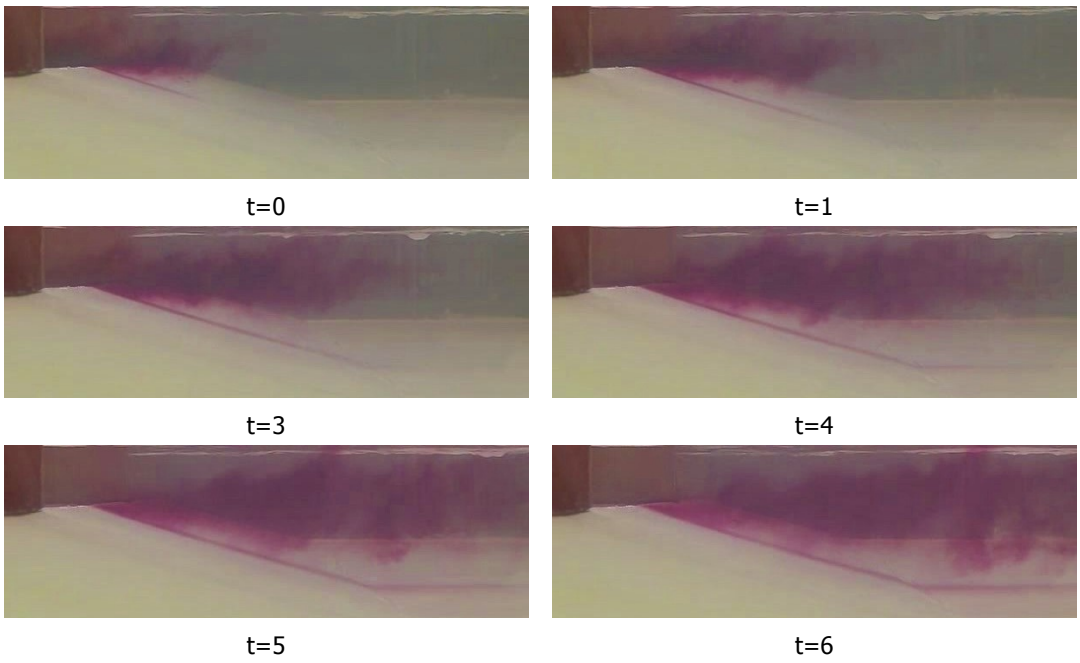

Figure 4.4: A side view photo series of vertical flow separation of the jet centre at the downward slope. The interval between each time steps equals 0.2 s. (Run 1.8.1: slope 1:4, B1=1.0 m, $L_{b,m}$=0.0 m and no grid)

To confirm that vertical flow separation would occur on a 1:4 and 1:6 downward slope, four reference cases were set up that did not contain any horizontally contracting objects. Dye injection and the ADV measurements presented in Figure 4.5 indeed show vertical flow separation on a 1:4 and 1:6 slope.

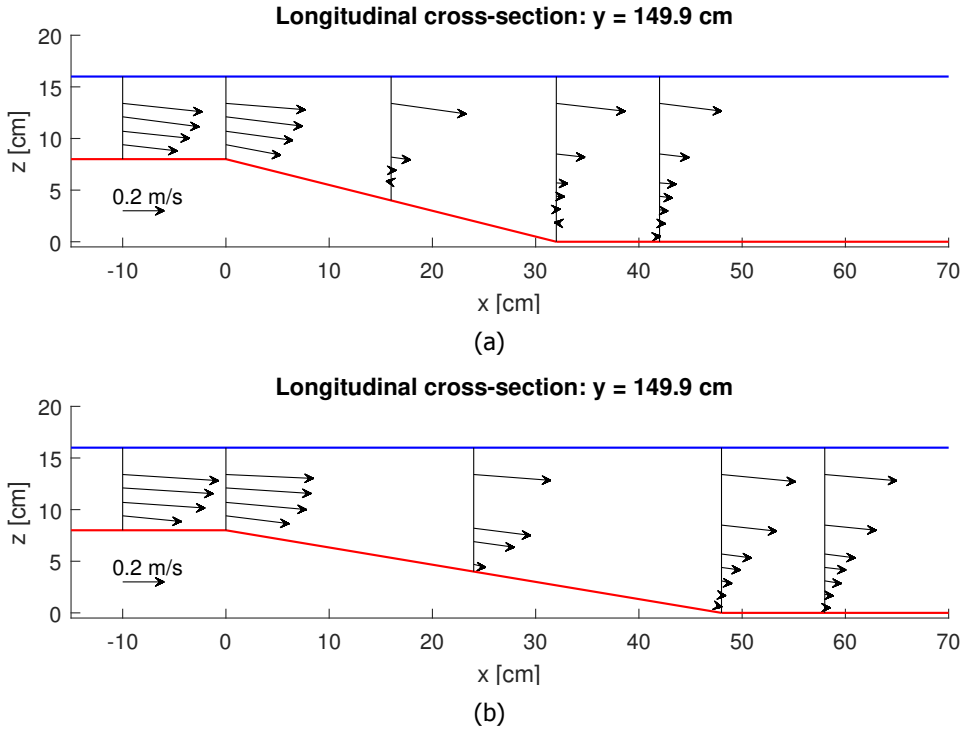

Figure 4.5: References cases that confirm vertical flow separation on a 1:4 and 1:6 downward slope for a uniform base flow: (a) Run 1.1.3: slope 1:4, B1=3.0 m and no grid. (b) Run 2.1.1: slope 1:6, B1=3.0 m and no grid.

In Figure 4.5 it can be seen that the recirculation zone on the 1:4 slope is more pronounced compared to the recirculation zone that formed on the 1:6 slope. In the case of the 1:4 slope, a clear reversal of the flow is observed on the downstream part of the slope which was not measured for the 1:6 reference case.

For the experiments that contained a lateral expansion, it was found that during some runs vertical flow separation was suppressed a part of the downward slope. The flow remained vertically attached to the upstream part of the slope, while at the downstream end a recirculation zone was observed. In that case, the separation point was located somewhere along the slope instead of at the upstream edge. This process is schematically presented in Figure 4.6. It should be noted that although the separation point in Figure 4.6b is indicated at a fixed location, its position may vary due to turbulence structures.

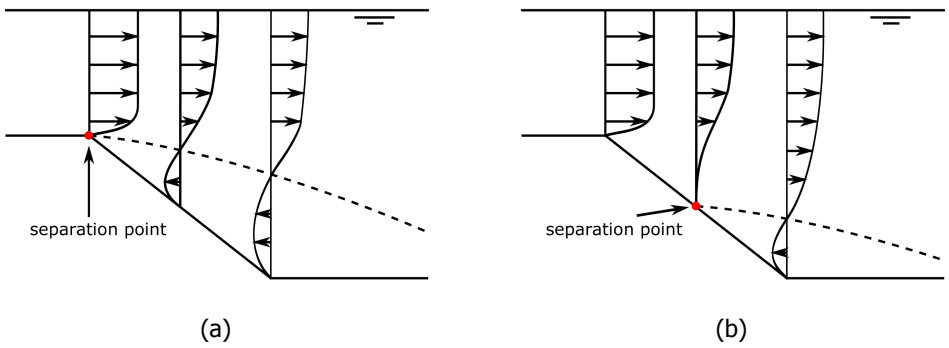

Figure 4.6: Schematic overview of the observed types of flow separation: (a) Vertical flow separation from the the upstream edge of the downward slope and (b) Vertical flow separation at an arbitrary point along the downward slope.

Although vertical flow separation of the jet centre was observed in the majority of the experiments, it was found that for these experimental runs the flow remained vertically attached in the shear layers adjacent to the jet flow. Figure 4.7 shows vertical flow separation in the centre of the jet (magenta), while the flow in the horizontal mixing layer (red) stays attached to the downward slope.

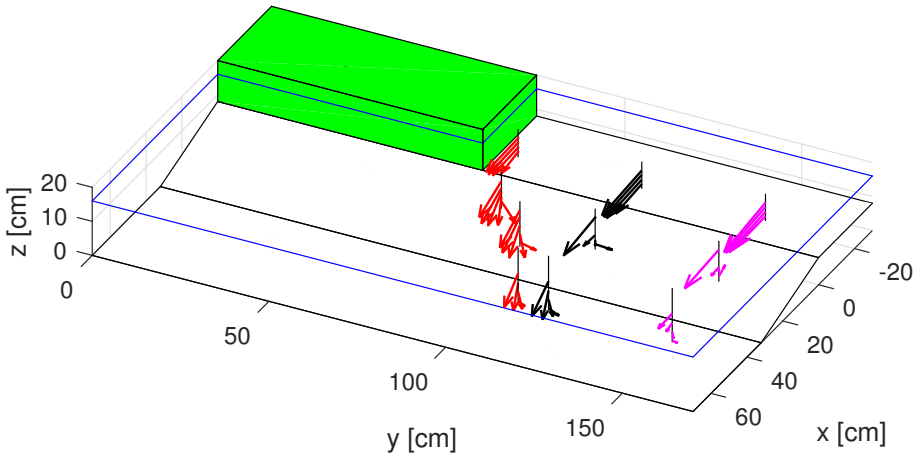

Figure 4.7: Detailed ADV measurements of the flow conditions at the downward slope on the right side of the flume, showing vertical flow separation in the centerline of the flume (magenta) and vertical flow attachment in the horizontal mixing layer (red). The green box and the blue lines indicate the right contracting element and the water surface level, respectively. (Run 1.4.1: slope 1:4, B1=1.5 m, $L_{b,m}$=0.0 m and no grid)

4.1.3. Conclusions

The experiments in the shallow flume can be classified according to the vertical flow state that was observed at the location of the downward slope: vertical flow attachment or separation of the jet centre. The vertical flow state of an experimental run was based on the motion of dye and tracer particles in the vertical recirculation zone, if present. Since in some experiments the residence time of the dye and tracer particles in the vertical recirculation zone was short, i.e. in the order of 1 to 2 s, a clear distinction of the vertical flow state by visual inspection only might be inaccurate. The vertical state of the flow was also assessed by the results of the ADV measurements. It was found that in the case of vertical flow attachment of the jet centre, the near-bed velocities remained nearly as high as for the rest of the water column (Figure 4.3). The assumption of a quasi-two-dimensional horizontal flow then seems justified.

The experimental runs in which vertical flow attachment was observed are categorised according to their expected generation mechanism. The flow attachment observed in category 1 is expected to be the result of an additional acceleration through conservation of potential vorticity, and therefore best resembles the situation observed near the ES-SSB. An explanation for the generation mechanism of experiments in category 2 will be proposed in subsection 4.3.3.

The experimental runs described in category 1 have in common that they all have a slope steepness of 1:6. Compared to the experiments with a slope of 1:4, the flow experiences a relatively small deceleration and thus a smaller adverse pressure gradient should persist. An additional acceleration through conservation of potential vorticity is, therefore, more likely to overcome the adverse pressure gradient such that the flow remains vertically attached to the downward slope. Additionally, an equal ratio for the upstream flow width over the width of the contracting elements was maintained in the experimental runs of category 1, namely $B1/D$=1. For these runs, the width of the horizontal mixing layers is relatively large with respect to the width of the jet flow, compared to other experiments in which larger ratios were maintained.

The ADV data indicate that the references cases of the 1:4 and 1:6 downward slope both result in a stagnation of the flow at the location of the downward slope along the centerline of the flume, see

Figure 4.5. For the reference case of the 1:4 slope, the flow velocities in the lower half of the water column downstream of the false bottom show a larger relative decrease compared to the reference case of the 1:6 slope. This can be explained by a larger deceleration of the flow due to the steeper downward slope. Visual inspection by injection of dye showed that in the reference case of the 1:4 slope a clear recirculation flow was present near the bed. As the ADV results of the 1:4 reference case do not show a significant return flow, it is suspected that the measurement device or the wire screen locally affects the flow conditions in the near-bottom region.

In section 4.1 a subdivision of experiments is made in vertical flow attachment and vertical flow separation at the downward slope in the centerline of the flume. This distinction might not be justified as a transition is present between the two processes, see Figure 4.6. In this thesis, vertical flow separation also refers to the scenarios in which the separation point is located along the downward slope.

For all experiments that showed vertical flow separation of the jet centre, it was found that the flow remained vertically attached in the shear layers (Figure 4.7). To understand the conditions that result in vertical flow attachment, the next step is to consider the horizontal structure of the flow field.

4.2. Horizontal flow structure

Field observations near the ES-SSB show that lateral velocity gradients are present in the flow. Lateral velocity variations include the effect of the jet flow, grid turbulence and large-scale gyres. These processes are reproduced in the experimental setup to investigate their effect on the vertical flow structure.

This section will first address the horizontal velocity field that was observed in experiments with vertical flow attachment. Then, the surface flow of experiments in which vertical flow separation of the jet centre was observed will be discussed. Lastly, a more detailed study of the streamwise velocity profiles and observations of the asymmetric basin flow will be presented.

4.2.1. Experiments with vertical flow attachment of the jet flow

Based on the generation mechanisms that cause vertical flow attachment a subdivision into two categories was made in subsection 4.1.1. This subsection discusses the horizontal flow structures that are representative for these categories.

Flow attachment: Category 1

Flow attachment of the experimental runs in category 1 is expected to be caused by the additional acceleration of the flow through conservation of potential vorticity. Since the mean surface velocities of the runs in category 1 show a similar pattern, the PIV results of only one experiment will be shown and discussed in more detail. An example of the mean surface velocity of Run 2.4.3, that is representative for flow attachment in category 1, is depicted in Figure 4.8.

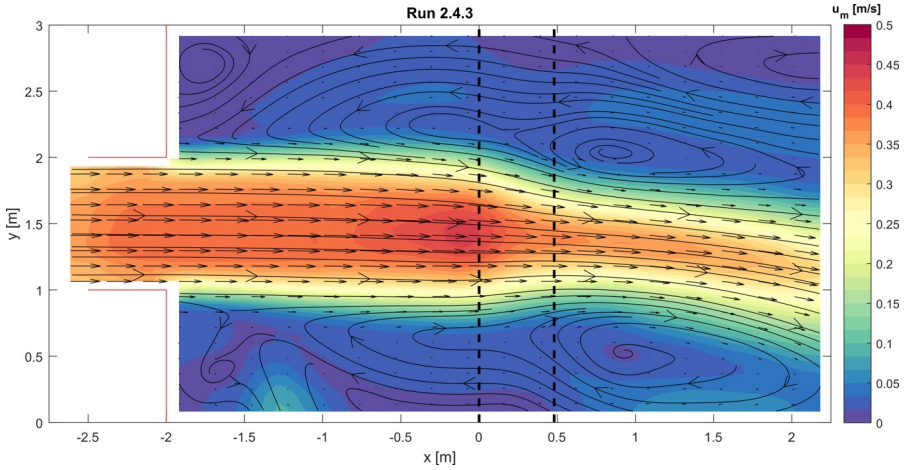

Figure 4.8: Representative mean surface velocity for flow attachment in category 1. (Run 2.4.3: slope 1:6, B1=1.0 m, $L_{b,m}$=2.0 m and no grid)

The following observations are made from Figure 4.8:

1. *Jet flow.* At the location of the lateral expansion the wall boundary layers separate from the contracting elements resulting in the formation of a jet flow. The width of the shear layers along the sides of the jet flow grow in width with downstream distance from the lateral expansion. The flow velocity in the centre of the jet flow shows a local increase just upstream of the slope. Furthermore, it was found that downstream of the downward slope the jet is deflected towards one of the glass side walls.

2. *Flow contraction at the downward slope.* In the experiments, it was found that the flow contracts at the location of the downward slope. This contraction of the flow continues until approximately 1 m downstream of the slope, after which the streamlines diverge indicating the spreading of the jet flow.

3. *Horizontal recirculation zones.* Horizontal recirculation zones formed in the lee of the contracting elements. These recirculation zones contained at least two smaller steady gyres with different rotational directions. In Figure 4.8, the rotational axes of the gyres are found at approximately x=-1.8 m and x=1.0 m.

Using Equation 2.6 the vertical vorticity ω_z can be determined from the velocity data that is presented in Figure 4.8. An example of the vertical vorticity at the surface that is representative for flow attachment category 1 is given in Figure 4.9.

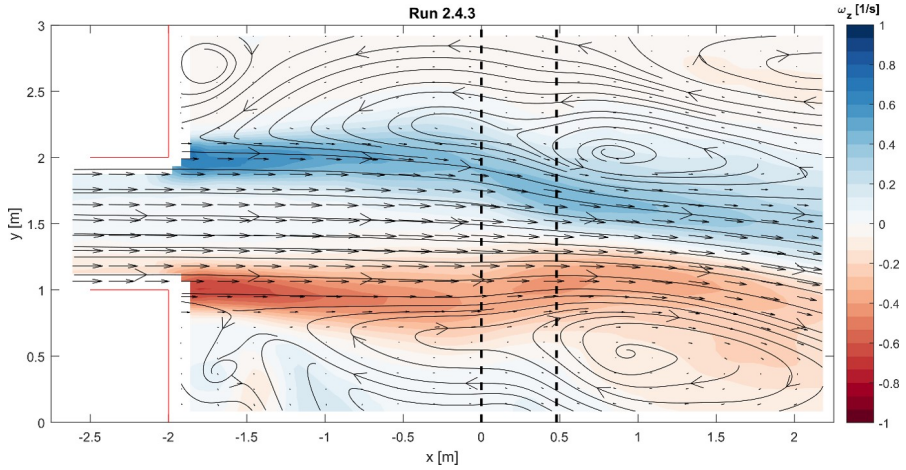

Figure 4.9: Representative mean vertical vorticity at the surface for flow attachment in category 1. (Run 2.4.3: slope 1:6, B1=1.0 m, $L_{b,m}$=2.0 m and no grid)

In Figure 4.9 it can be seen that the minimum and maximum vertical vorticity are found in the horizontal mixing layers of the jet. Additionally, it can be observed that the vertical vorticity determined at the water surface decreases in downstream direction. No increase of vertical vorticity is found downstream of the downward slope which could be expected from conservation of potential vorticity, as discussed in subsection 2.2.5.

Flow attachment: Category 2

Figure 4.10 depicts the results of the PIV measurements of Run 1.5.1. These results are considered to be representative for the experimental runs in category 2, where the grid elements are located directly upstream of the slope. The PIV results of the mean surface velocity of the experiments assigned to category 2 show that the flow conditions deviate from horizontal flow structure that is characteristic for flow attachment category 1. This supports the expectation that a different generation mechanism is responsible for the attachment in category 2.

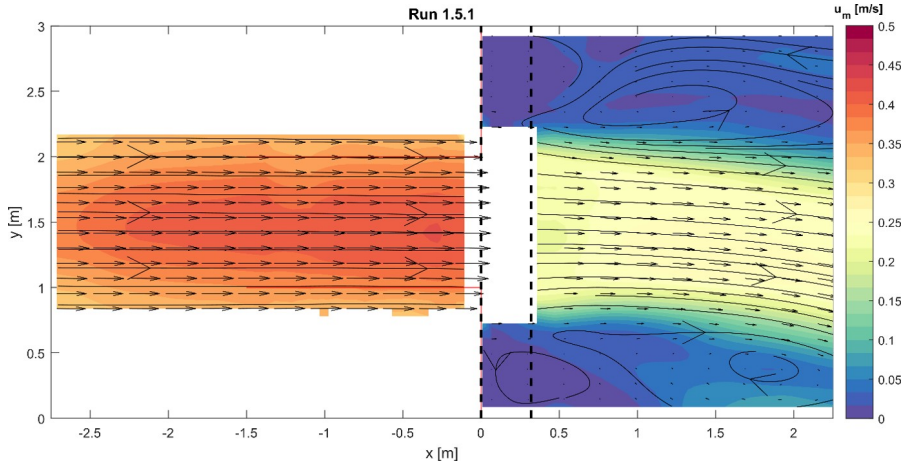

Figure 4.10: Representative mean surface velocity for vertical flow attachment in category 2. (Run 1.5.1: slope 1:4, B1=1.5 m, $L_{b,m}$=0.0 m and with grid)

Figure 4.10 shows an abrupt decrease of the flow velocity downstream of the grid elements. The flow velocity downstream of the grid is reduced to about half the flow velocity that can be observed upstream of the downward slope. Part of the velocity data at the location of the downward slope is not displayed. The reliability of the PIV data as was previously discussed in subsection 3.5.2.

4.2.2. Experiments with vertical flow separation of the jet centre

A remarkable observation in the reference cases, where vertical flow separation at the downward slope was observed, was that the flow already showed a contracting behaviour without the presence of any horizontal contracting elements in the experimental setup. Figure 4.11 shows the dispersion of the dye that is injected near the glass side wall upstream of the slope. At the location of the upstream end of the slope, the wall boundary layer seems to be disturbed and streamlines bend under an angle of approximately 45° towards the centerline of the flume. This phenomenon was observed along both side walls for all reference cases.

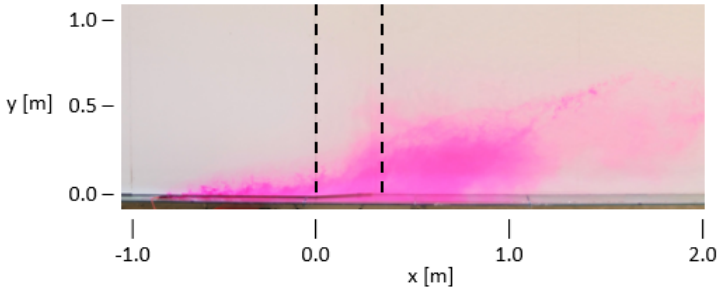

Figure 4.11: Contraction of the flow at the downward slope for a reference case. (Run 1.1.3: slope 1:4, B1=3.0 m and no grid)

In all references cases, the injection of dye revealed steady recirculation zones along the side walls at the location of the slope. For the 1:4 slope, several experiments were conducted to investigate the effect of the flow velocity on the magnitude of the contraction (Run 1.1.1, Run 1.1.2 and Run 1.1.3). The PIV measurements show that the streamlines at the water surface do not differ between these runs. It is therefore assumed that the contracting behaviour is independent of the flow velocity. Figure 4.12 shows an example of the mean surface velocity in the right half of the flume of Run 1.1.3. Significantly lower flow velocities can be observed in the mixing layer downstream of the slope. Also, a small region with slightly higher flow velocities is observed adjacent to the mixing layer. From visual inspection, it was concluded that the mixing layers along the side walls were approximately equal in size for the reference cases with a 1:4 downward slope.

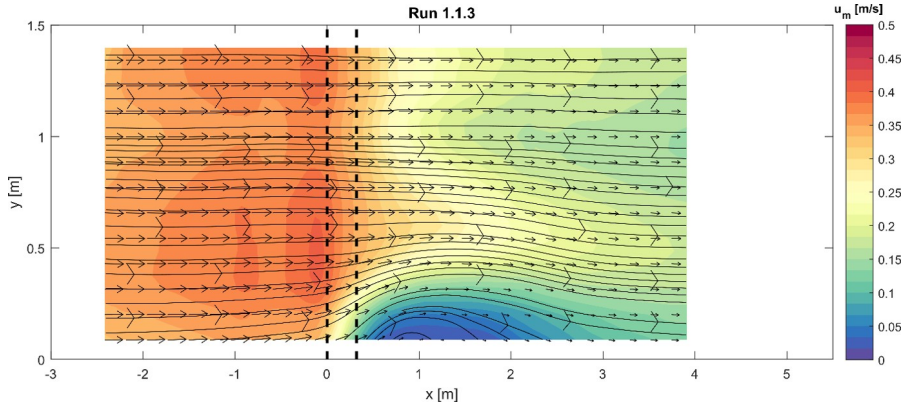

Figure 4.12: Mean surface velocity of a reference case with a 1:4 slope. (Run 1.1.3: slope 1:4, B1=3.0 m and no grid)

The reference case of the 1:6 downward slope shows a stronger contraction of the flow compared to the runs with a 1:4 slope. Figure 4.13 depicts the results of the PIV analysis for the reference case of the 1:6 slope that includes measurements over the full width of the flume. Although the experimental setup was geometrically symmetrical, the mean surface velocity shows an asymmetric basin flow in which the horizontal recirculation zones significantly differ in size. Due to an increase of the total width of the recirculation zones, the flow velocity downstream of the slope remains relatively higher compared to the runs with a 1:4 slope. Lastly, it can be observed that the boundary layer separation from the side wall of the largest recirculation is already initiated upstream of the slope.

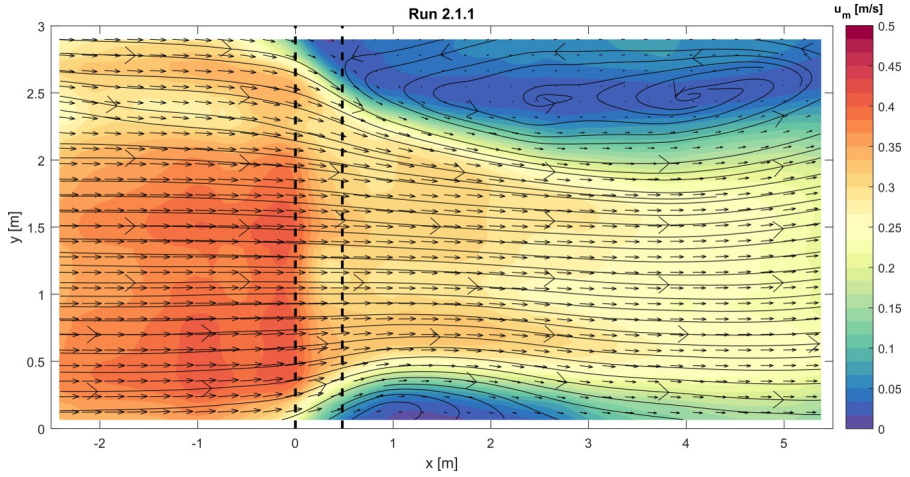

Figure 4.13: Mean surface velocity of a reference case with a 1:6 slope. (Run 2.1.1: slope 1:6, B1=3.0 m and no grid))

Contraction of the flow at the location of the downward slope was also observed in the experimental runs that included a lateral expansion and showed vertical separation of the jet centre. Comparing the PIV outcomes of experiments with vertical flow attachment and vertical flow separation does not reveal a clear difference in the horizontal structure of the surface flow. To illustrate this, Figure 4.14 depicts the PIV analysis of Run 1.8.3 that resulted in vertical flow separation of the jet centre at the slope. The only difference in the experimental setup with Run 2.4.3, in which vertical flow attachment was observed, is the steepness of the slope. Comparing the PIV results of Run 1.8.3 (Figure 4.14) to Run 2.4.3 (Figure 4.8) shows a nearly equal mean surface flow. A small difference can be found in the velocity in the centre of the jet flow downstream of the slope, which in the case of flow attachment remains relatively high at a larger distance from the slope.

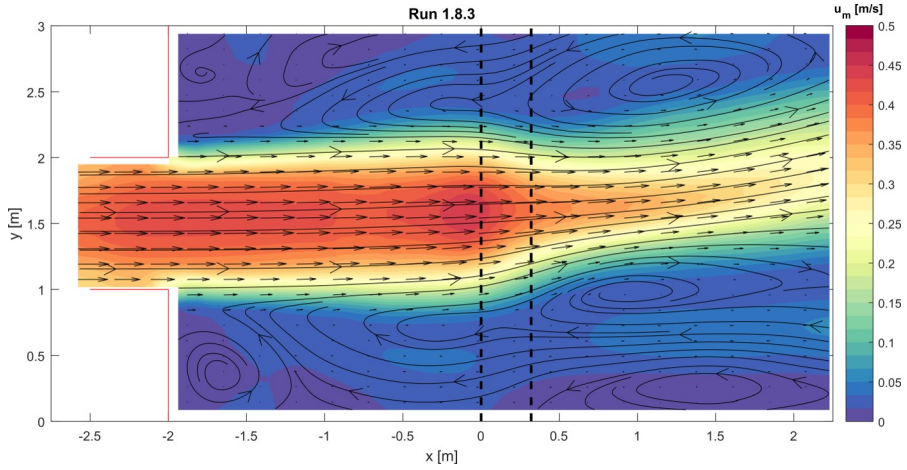

Figure 4.14: Representative mean surface velocity for vertical flow separation of the jet centre. (Run 1.8.3: slope 1:4 , B1=1.0 m, $L_{b,m}$=2.0 m and no grid)

Dye visualisation was used to further reveal the horizontal structure of the flow at the location of the downward slope. The following two observations were made:

1. *Deformation and deflection of the eddies in the horizontal mixing layers.* It was observed that downstream of the lateral expansion, the eddies in the horizontal mixing layers followed a path nearly parallel to the side walls of the flume. Above the slope, however, the eddies were horizontally stretched in the direction of the flow and deflected to the high-velocity side. Downstream of the slope the eddies restored to a circular shape. Also, it was found that when increasing the distance between the lateral expansion and the downward slope $L_{b,m}$, the eddies in the horizontal mixing layers became larger at the location of the slope. Figure 4.15 depicts the deflection of the eddies in the horizontal mixing layers. Lastly, it should be noted that the deformation of the vortices in the experiments deviated from the deformation that was expected based on conservation of potential vorticity as depicted in Figure 2.11.

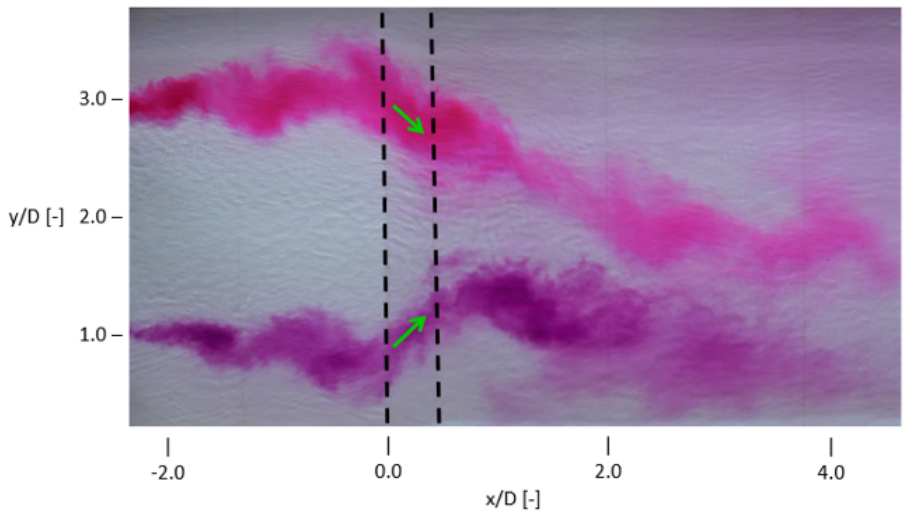

Figure 4.15: Contraction of the flow at the downward slope resulting in the deflection of eddies. (Run 1.5.3: slope 1:4 , B1=1.5 m, $L_{b,m}$=2.0 m and with grid)

2. *Sideways transport in the vertical recirculation zone.* Inspection with dye showed that the vertical circulation cell on the downward slope contained a lateral component. In Figure 4.16 it can be seen that dye is transported along the slope towards the centerline of the flume. In this movement, the dye is taken up by the vertical mixing layer and diffused in downstream direction. This explains the distribution of dye over the width of the jet flow downstream of the slope.

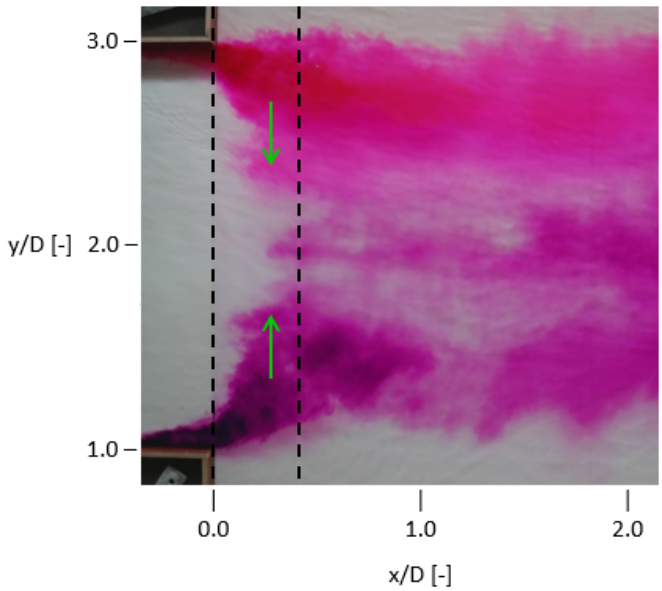

Figure 4.16: Dye visualisation of the sideways transport in the vertical recirculation zone. The direction of the dye near the surface of the slope is indicated by the green arrows. (Run 1.4.1: slope 1:4 , B1=1.5 m, $L_{b,m}$=0.0 m and no grid)

A more detailed study of the obtained PIV data is required to determine the surface flow characteristics that are associated with vertical flow attachment and vertical flow separation. As a next step, the streamwise velocity of several transverse transects along the flume will be considered to describe the horizontal structure of the jet flow for various experimental runs.

4.2.3. Streamwise velocity profiles

Streamwise velocity profiles of several experimental runs are presented to investigate the effect of experimental variables on the lateral velocity gradient. In order to make a fair comparison between the different experimental runs, the PIV results are linearly interpolated to specific transverse transects along the flume.

Influence of the slope steepness

Streamwise velocity profiles along transverse transects of the slope indicate minor differences in the surface flow for vertical flow attachment of the jet flow and vertical flow separation of the jet centre, as for example depicted in Figure 4.17. In Figure 4.17 the only difference in the geometry of the experimental setup between the considered runs is the slope steepness.

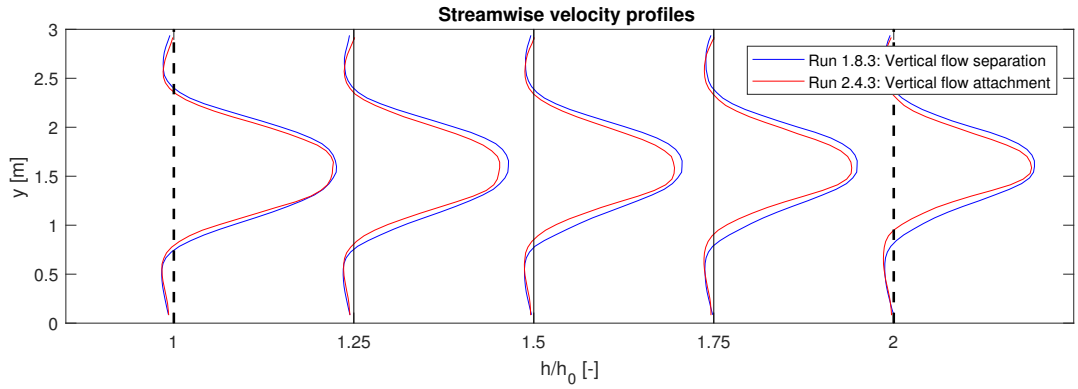

Figure 4.17: Streamwise velocity profiles of vertical flow attachment of the jet flow and vertical flow separation of the jet centre. In the figure $h/h_0 = 1$ and $h/h_0 = 2$ indicate the upstream and downstream end of the downward slope, respectively. (Run 1.8.3: slope 1:4 , B1=1.0 m, $L_{b,m}$=2.0 m and no grid. Run 2.4.3: slope 1:6 , B1=1.0 m, $L_{b,m}$=2.0 m and no grid)

The experimental run with vertical flow attachment in Figure 4.17 shows slightly larger lateral velocity gradients in the streamwise velocity profiles compared the scenario of vertical flow separation of the jet centre. To clarify this, Figure 4.18 depicts the lateral velocity gradients that correspond to the streamwise velocity profiles of Figure 4.17. The lateral velocity gradient was calculated from individual data points. No curve was plotted through the obtained data to smooth the velocity profiles depicted in Figure 4.17.

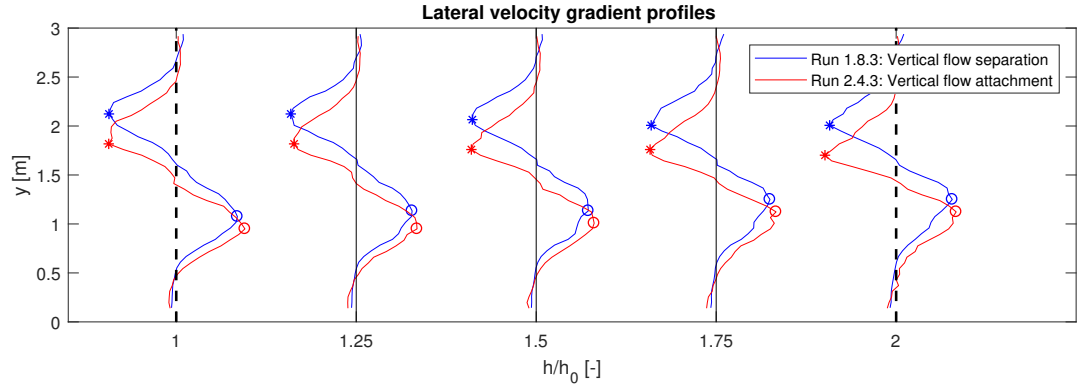

Figure 4.18: Lateral velocity gradient profiles corresponding to the streamwise velocity profiles presented in Figure 4.17. (Run 1.8.3: slope 1:4 , B1=1.0 m, $L_{b,m}$=2.0 m and no grid. Run 2.4.3: slope 1:6 , B1=1.0 m, $L_{b,m}$=2.0 m and no grid)

Additionally, Figure 4.19 presents the absolute values of the minimum and maximum lateral velocity gradients that are obtained from Figure 4.18. In the case of vertical flow attachment, it is found that no (significant) increase in the lateral velocity gradient can be observed at the location of the downward slope as would be expected through conservation of potential vorticity.

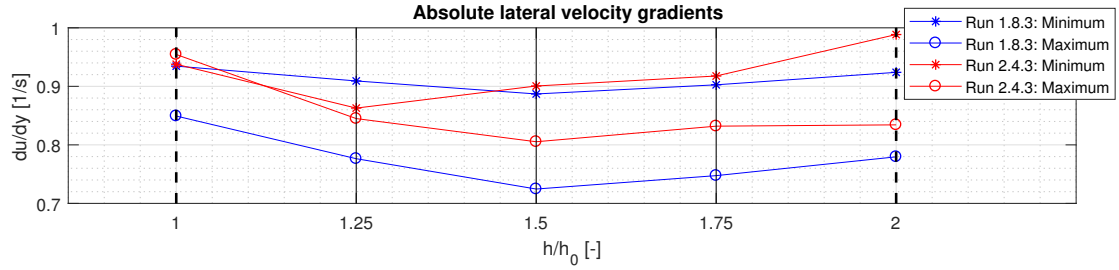

Figure 4.19: Absolute values of the minimum and maximum lateral velocity gradients of the mixing layers corresponding to the lateral velocity gradient profiles presented in Figure 4.18.

Influence of the location of the lateral expansion

The influence of the distance between the lateral expansion and the downward slope $L_{b,m}$ on the lateral velocity gradient was investigated. A comparison between Run 1.4.1, Run 1.4.2 and Run 1.4.3, in which the only geometric difference in the setup is the length $L_{b,m}$, is shown in Figure 4.20. It can be seen that the maximum streamwise velocity decreases when the lateral expansion is located 2 m upstream of the slope (Run 1.4.3). Furthermore, it can be observed that the lateral velocity gradient decreases with increasing values of $L_{b,m}$, resulting in a spreading of the streamwise velocity profile. The lateral velocity gradient profiles corresponding to Figure 4.20 are presented in Figure 4.21.

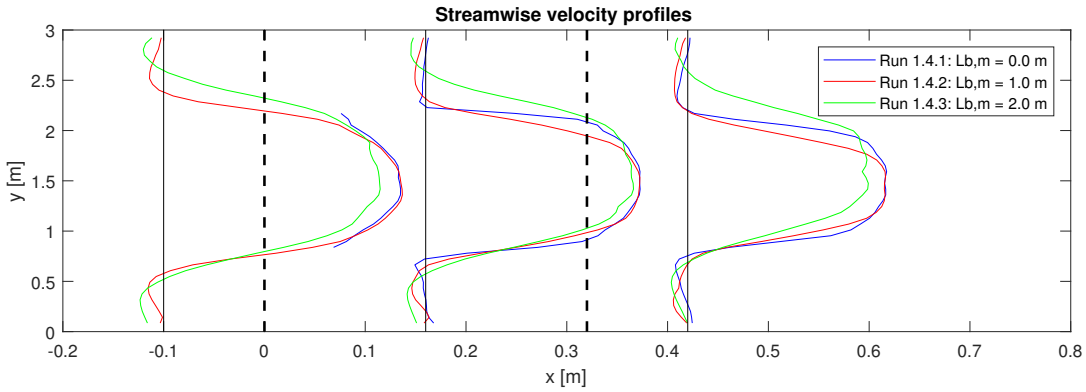

Figure 4.20: Example of the influence of the distance between the lateral expansion and the upstream slope $L_{b,m}$ on the streamwise velocity profiles. These experiments all resulted in vertical flow separation of the jet centre. (Run 1.4.1: slope 1:4, B1=1.5 m, $L_{b,m}$=0.0 m and no grid. Run 1.4.2: slope 1:4, B1=1.5 m, $L_{b,m}$=1.0 m and no grid. Run 1.4.3: slope 1:4, B1=1.5 m, $L_{b,m}$=2.0 m and no grid)

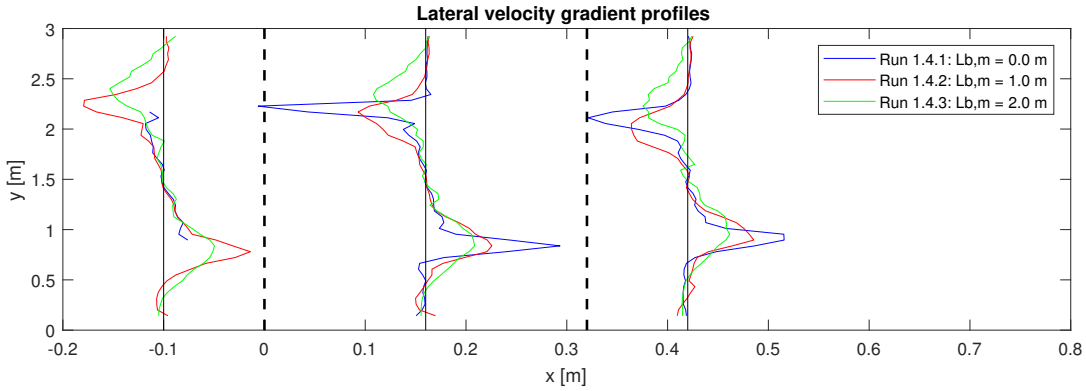

Figure 4.21: Lateral velocity gradients corresponding to the streamwise velocity profiles in Figure 4.20

Based on the literature study it is expected that the width of the mixing layer increases with downstream distance from the lateral expansion, see subsection 2.3.4. To verify this Figure 4.22 depicts the measured width of the mixing layer for Run 1.4.2 and Run 1.4.3 dependent on the downstream distance from the lateral expansion x_{lat}. Additionally, Figure 4.22 includes a model estimation of the growth of the mixing layer width proposed by Van Prooijen (2004). This modelling approach is based on the width of the mixing layer of an SML but was found to be applicable to SLE's as well by Talstra (2011). Van Prooijen (2004) defines the width of the mixing layer δ as:

$$\delta = \frac{\Delta U}{\frac{\partial U}{\partial y_c}} \tag{4.1}$$

where ΔU is the mean velocity difference over the mixing layer and $\partial U/\partial y_c$ the lateral velocity gradient in the centre of the mixing layer. The theoretical expression for the mixing layer width of an SLE, that is based on the modelling approach of van Prooijen and Uijttewaal (2002), is by Talstra (2011) given as:

$$\delta(x_{lat}) = 2\alpha\frac{h}{2c_f}\left(1 - \exp\left[-\frac{2c_f}{h}x_{lat}\right]\right) + \delta_0 \tag{4.2}$$

in which α is the entrainment coefficient ($\alpha \approx 0.085$), c_f the bed friction coefficient ($c_f \approx 0.005$ for a turbulent flow over a smooth bottom (van Prooijen and Uijttewaal, 2002)) and δ_0 the initial mixing layer width emerging from the boundary layer that has developed upstream of the separation point ($\delta_0 \approx h$).

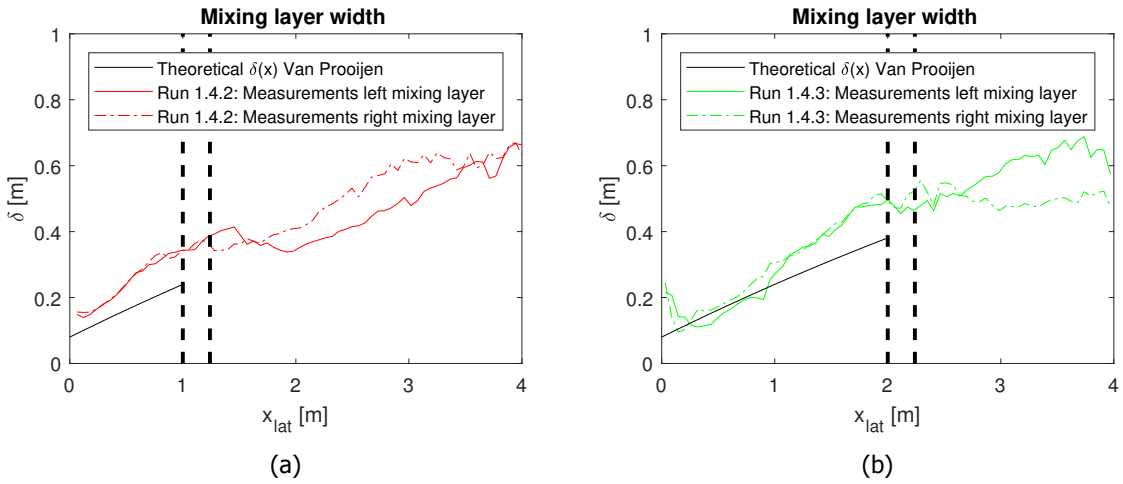

Figure 4.22: Comparisons of the measured width of the mixing layers between Run 1.4.2 and Run 1.4.3, and the theoretical value based on the modelling approach of Van Prooijen (2004). For each experiment the width of both mixing layers of the jet was measured. (Run 1.4.2: slope 1:4 , B1=1.5 m, $L_{b,m}$=1.0 m and no grid & Run 1.4.3: slope 1:4 , B1=1.5 m, $L_{b,m}$=2.0 m and no grid)

From Figure 4.22 it can be seen that the widths of the mixing layers measured in the experiments grow with increasing distance from the lateral expansion. The width of the left and right mixing layer are approximately equal upstream of the downward slope but deviate downstream of the slope. Furthermore, it can be observed that the growth rate of the mixing layer width upstream of the downward slope is larger compared to that downstream of the slope. Overall, the modelling approach of Van Prooijen (2004) results in a smaller estimation for the width of the mixing layers than is determine based on the experiments.

Influence of the upstream flow width

Lastly, Figure 4.23 depicts an example that is representative for the influence of the upstream flow width $B1$ on the lateral velocity gradients. It was found that a larger upstream flow width $B1$ results in a wider jet flow. The maximum lateral velocity gradients are, however, unaffected by the variation of this experimental variable. Furthermore, it can be observed that the shape of the experiment with the widest jet flow (Run 1.6.2) deviates from the other experimental runs.

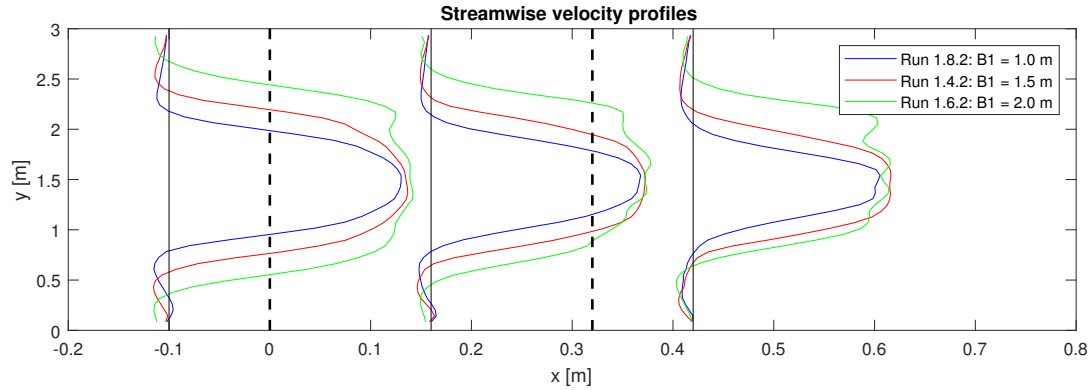

Figure 4.23: Example of the influence of the upstream flow width $B1$ on the streamwise velocity profiles for Run 1.8.2, Run 1.4.2 and Run 1.6.2. These experiments all resulted in vertical flow separation. (Run 1.8.2: slope 1:4 , B1=1.0 m, $L_{b,m}$=1.0 m and no grid, Run 1.4.2: slope 1:4 , B1=1.5 m, $L_{b,m}$=1.0 m and no grid & Run 1.6.2: slope 1:4 , B1=2.0 m, $L_{b,m}$=1.0 m and no grid)

As approximately half of the conducted experiments included the effect of grid turbulence, results of these experimental runs will be discussed separately in section 4.3.

4.2.4. Asymmetric basin flow

It was found that despite the symmetry of the experimental setup the flow field often behaved asymmetrically. This was observed in all experimental runs except for the reference cases with a 1:4 downward slope. For instance, Figure 4.24 shows that during Run 1.5.1 the jet flow was deflected to the left glass side wall. In this case, the jet impinged on the glass side wall approximately 5 m downstream of the slope. Switching the pump off and on without adjusting the downstream weir could result in the deflection of the jet to the right side wall. It was therefore assumed that the deflection of the jet was caused by subtle pressure differences. The asymmetric flow was found to be stable as the jet did not change its direction when the boundary conditions were kept constant.

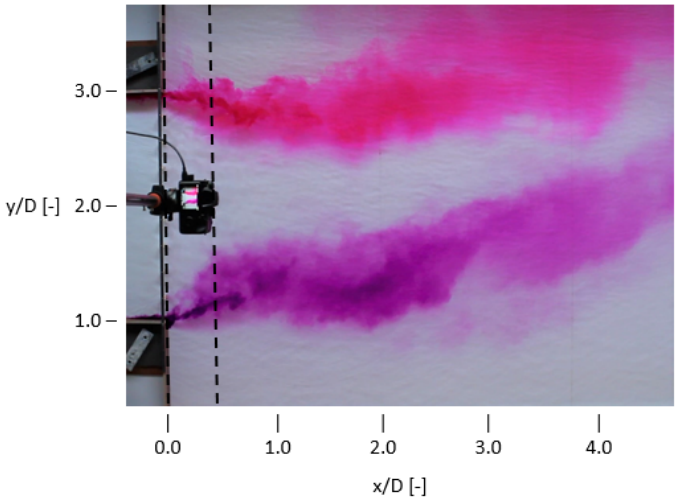

Figure 4.24: Deflection of the jet flow visualised by dye injection. (Run 1.5.1: slope 1:4, B1=1.5 m, $L_{b,m}$=0.0 m and with grid)

The deflection of the jet flow has consequences for the horizontal recirculation zones downstream of the lateral expansion. Figure 4.25 depicts the mean surface velocity of Run 1.4.2. First of all, the figure shows the deflection of the jet to the right side wall. Secondly, it can be observed that the size of the recirculation zones downstream of the contracting elements significantly differs. The recirculation zone along the glass side wall where the jet flow attaches, from now on named the non-dominant gyre, is smaller compared to the other recirculation zone. The largest recirculation zone will in the remainder of this work be referred to as the dominant gyre. It was found that during all experimental runs in which the flow showed an asymmetric pattern, the reattachment point of the dominant gyre was located approximately 1 m upstream of the weir. Figure 4.24 also shows that the dominant and non-dominant gyre contain an unequal number of smaller gyres. In general, the non-dominant gyre contained a primary and a secondary gyre, while the dominant gyre could consist of four smaller sub-gyres.

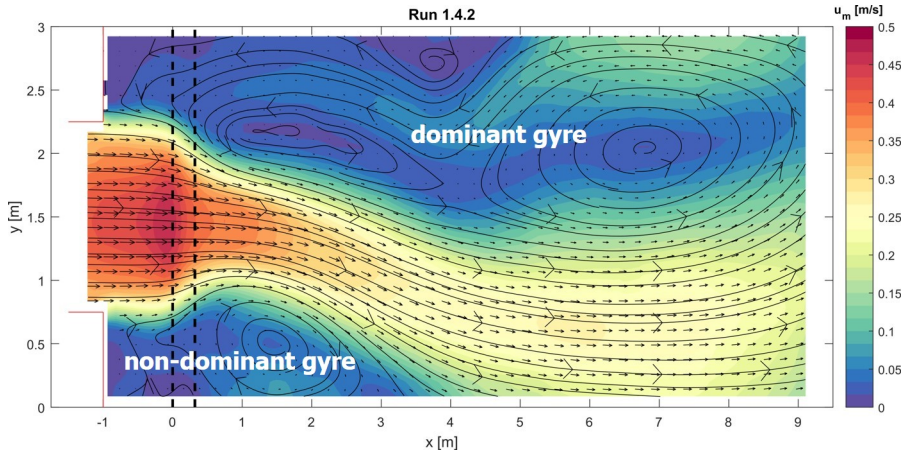

Figure 4.25: Asymmetric basin flow. (Run 1.4.2: slope 1:4, B1=1.5 m, $L_{b,m}$=1.0 m and no grid)

Kantoush and Schleiss (2009) have described the flow pattern of several shallow basin flows. Depending on a geometric shape factor, it was found that the flow in a basin showed a symmetric or asymmetric structure. In their study, it was concluded that the length of the basin mainly determined the behaviour of the flow field. The asymmetric flow pattern in shallow basins was explained to be a Coanda effect. A consequence of the asymmetric basin flow is that the horizontal mixing layer of at the side of the non-dominant gyre is more affected by the wall boundary layer compared to the other mixing layer of the jet flow. This is not expected to be problematic in this research thesis.

4.2.5. Conclusions

Subsection 4.2.1 describes the horizontal structure of the experimental runs in which vertical flow attachment of the jet flow was observed. As previously noted, for this vertical flow state the velocity is approximately uniform over the water depth, such that the flow field can be characterised as a quasi-two-dimensional horizontal flow. Therefore, it is assumed that the surface flow obtained by PIV is representative for the horizontal structure of the flow.

The horizontal structure of the flow depicted in Figure 4.8, that is representative for flow attachment category 1, shows several similarities with flow conditions observed in the experiments of Talstra (2011) in which an SLE was investigated, see subsection 2.3.4. These similarities include the presence of a lateral velocity gradient, the development of 2DCH in the mixing layer and the formation of a circulation zone that includes smaller gyres. A clear difference with the experiment of Talstra (2011) is that the horizontal flow structure in Figure 4.8 contains a contraction of the flow. This contraction of the flow is found at the location of the downward slope and is expected to be caused through conservation of potential vorticity. Although the water depth doubles downstream of the slope, it is found that due to this flow contraction velocities in the centre of the jet remain relatively high. Also, a representative plot of the vertical vorticity (Figure 4.9) reveals that the vorticity in the horizontal mixing layers decreases in downstream direction. This is not in line with the expectation of subsection 2.2.5 in which it was discussed that the vorticity would increase for a depth increase based on conservation of potential vorticity.

A remarkable observation in the reference cases is that a contraction of the flow at the location of the downward slope already presents itself when no horizontally contracting elements are included in the experimental setup, as depicted in Figure 4.12. It is found that the wall boundary layers separate near the upstream edge of the slope and thereby induce a contraction in the horizontal flow field.

Another important finding through the laboratory experiments is that in all experimental runs a contraction of the flow was observed at the location of the downward slope, including the experiments with vertical flow separation of the jet centre. This is in contradiction with the results of Broekema (2017a), in which the depth average flow showed a diverging behaviour on the slope for experiments in which vertical flow separation was observed. From the experiments performed for this master thesis, it can be concluded that a converging flow at the location of a downward slope is not necessarily a characteristic for vertical flow attachment along the full width of the jet flow.

An analysis of streamwise velocity profiles has shown the influence of the experimental variables on the streamwise surface velocity profiles, except for the impact of the grid elements. First of all, it can be concluded that no clear difference of the streamwise surface velocity is observed between experimental runs with vertical attachment of the jet flow and vertical separation of the jet centre, as depicted in Figure 4.17. The minimum and maximum lateral velocity gradients obtained from these streamwise velocity profiles were found to be approximately constant at the location of the downward slope (Figure 4.19). For the experimental run with vertical flow attachment, this is not in line with the expectations based on conservation of potential vorticity. In Equation 2.8 it was derived that vorticity increases proportional to a relative depth increase ($\omega/h =$ constant) and thus also the lateral velocity gradient when the lateral velocities are assumed to be small. Based on conservation of potential vorticity, one would expect a doubling of the lateral velocity gradient for a doubling of the water depth. This cannot be verified by the computed lateral gradients of the experiment with vertical flow attachment in Figure 4.19. The vertical state of experiments in flow attachment category 1 can therefore not entirely be explained through an acceleration through conservation of potential vorticity.

Secondly, it was found that for a larger distance between the lateral expansion and the downward slope the shear layers spread in lateral direction. This results in a wider jet flow with smaller lateral velocity gradients at the location of the downward slope. This deformation of a jet flow is in line with the expectations based on the literature study (Cohen, 2012).

Lastly, the effect of the ratio of the width of the upstream flow over the width of the contracting elements was investigated. It was found that the width of the shear layer with respect to the width of the jet flow is an important factor that affects the vertical state of the flow on a downward slope. For five experimental runs (Flow attachment: Category 1), that have in common a slope steepness of 1:6 and a ratio of $B1/D = 1$, it was expected that the vertical flow attachment at the downward slope over the full width of the jet would result from an acceleration through potential vorticity (Run 2.4.1, Run 2.4.2, Run 2.4.3, Run 2.5.2 and Run 2.5.3). The PIV measurements, that are assumed to be representative for the horizontal structure of the flow, do however not reveal conservation of potential vorticity as no increase in vertical vorticity was observed for an increasing water depth.

In Broekema (2017b) it was hypothesised that an additional acceleration of the flow through conservation of potential vorticity, if sufficiently large, can counteract the adverse pressure gradient on a downward slope that causes the boundary layer to separate. Based on the outcomes of visual inspection, ADV data and PIV measurement vertical flow attachment over the full width of the jet flow in the conducted experiments cannot be (fully) assigned to result from conservation of potential vorticity. The above-stated hypothesis is therefore rejected.

Experiments in which vertical flow separation of the jet centre was observed showed that the flow remained vertically attached to the slope in shear layers on the sides of the jet flow. So far, no possible explanation can be given for the local attachment of the flow.

Still unanswered remains what the effect is of the grid turbulence that is generated by the pillars of the ES-SSB on the flow conditions in the scour holes. The next section addresses the experiments that were performed to investigate the influence of grid turbulence on the flow downstream of the lateral expansion.

4.3. The influence of grid turbulence

A foamy top layer on the downstream side of the ES-SSB reveals the disturbance of the flow by the pillars of the barrier. The wakes that are formed show a systematic pattern as the pillars of the barrier are equally spaced along the inlet sections. This disturbance of the flow can be associated with grid turbulence. It was in the literature study shown that, based on the solidity of the grid of the ES-SSB, the formed eddies are not expected to merge and grow into large-scale coherent structures. The grid turbulence could, however, affect the background vorticity and the dissipation of it. In the experiments performed for this master thesis, the effect of the pillars of the barrier is investigated by the deployment of a simplified grid. This section discusses the results of the experimental runs with grid turbulence.

4.3.1. Vertical flow structure

Experiments in which vertical flow attachment is observed include experimental runs with and without grid turbulence. Figure 4.26 depicts a comparison of the vertical flow conditions between experimental runs with and without grid turbulence.

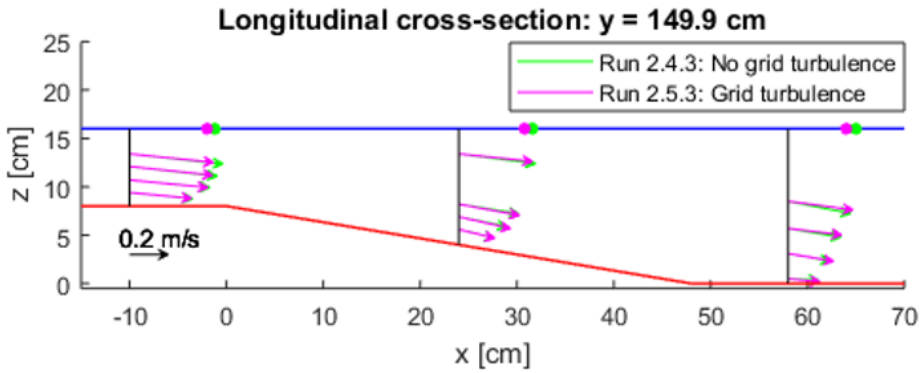

Figure 4.26: Comparison of the vertical flow conditions for experimental runs in flow attachment category 1 with and without grid turbulence. The data points displayed at the water surface are obtained with PIV. (Run 2.4.3: slope 1:6, B1=1.0 m, $L_{b,m}$=2.0 m and no grid. Run 2.5.3: slope 1:6, B1=1.0 m, $L_{b,m}$=2.0 m and with grid)

Figure 4.26 shows that the influence of the grid turbulence barely affects the mean vertical structure of the flow near the downward slope in the centerline of the flume. Only slightly larger flow velocities are found near the surface upstream of the downward slope. In addition, from Figure 4.27 it can be seen that no significant difference can be observed in the computed turbulent kinetic energy (TKE) between the considered experimental runs. See Equation 4.4 for the definition of the TKE.

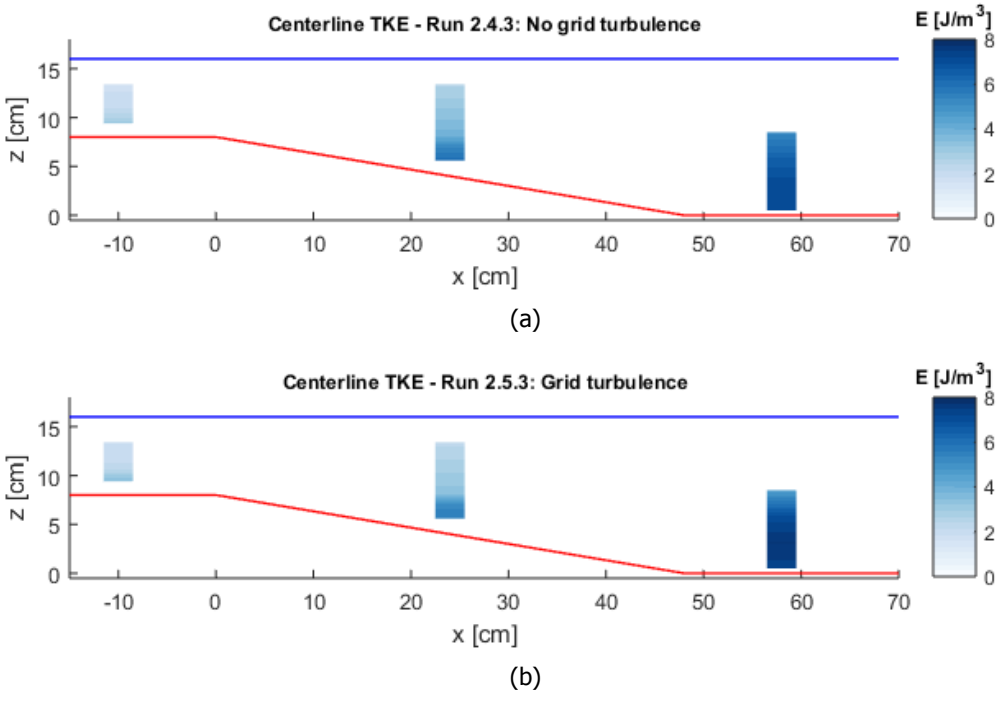

Figure 4.27: Comparison of the turbulent kinetic energy for corresponding experiments with and without grid turbulence. (a) Run 2.4.3: slope 1:6, B1=1.0 m, $L_{b,m}$=2.0 m and no grid. (b) Run 2.5.3: slope 1:6, B1=1.0 m, $L_{b,m}$=2.0 m and with grid.

A clear difference in the vertical structure of the flow, however, is found for experimental runs in which the grid was positioned directly upstream of the downward slope (Flow attachment: Category 2). A comparison of the vertical flow structure of experiments with and without grid turbulence in which the lateral expansion is located at x=0 m is presented in Figure 4.28.

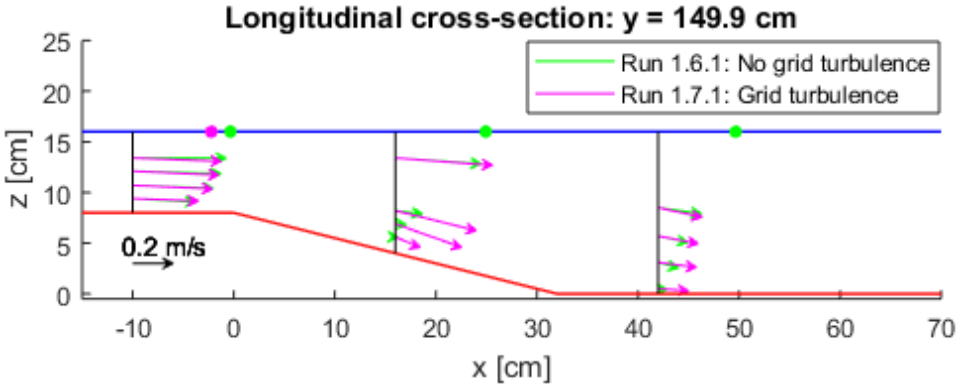

Figure 4.28: Comparison of the vertical flow conditions for experimental runs with and without grid turbulence in which the lateral expansion is located directly upstream of the downward slope. Since in Run 1.7.1 a grid element was located in the centerline of the flume, ADV measurements were performed along the longitudinal cross-section y=160.1 cm. The data points displayed at the water surface are obtained with PIV. (Run 1.6.1: slope 1:4 , B1=2.0 m, $L_{b,m}$=0.0 m and no grid. Run 1.7.1: slope 1:4 , B1=2.0 m, $L_{b,m}$=0.0 m and with grid.)

The instalment of the grid elements on the upstream edge of the slope directly resulted in vertical flow attachment, whereas in all corresponding experimental runs without a grid vertical flow separation was observed (with the expectation of Run 2.4.1). It is therefore expected that a different mechanism causes vertical flow attachment of the experimental runs assigned to category 2.

Experimental runs in which vertical flow separation of the jet centre was observed do not show a significant difference in the mean flow conditions at the location of the downward slope when grid turbulence is included. A representative example of the effect of grid turbulence in experiments with vertical flow separation of the jet centre is depicted in Figure 4.29.

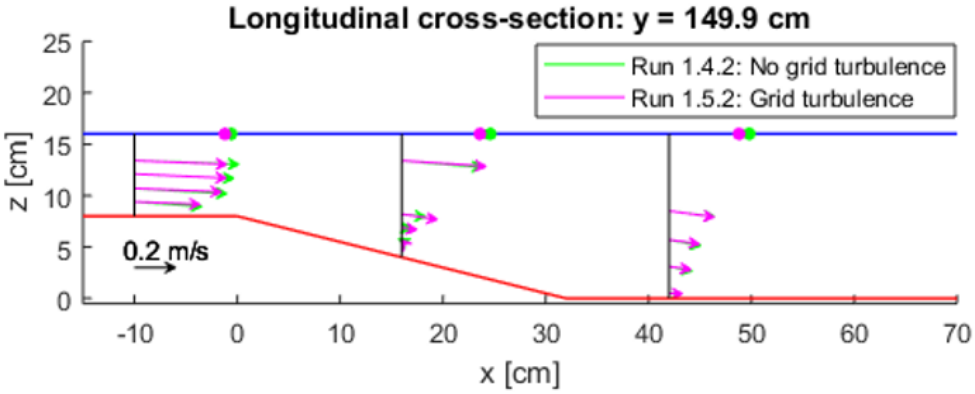

Figure 4.29: Comparison of the vertical flow conditions for experimental runs with and without grid turbulence in the case of vertical flow separation of the jet centre. The data points displayed at the water surface are obtained with PIV. (Run 1.4.2: slope 1:4 , B1=1.5 m, $L_{b,m}$=1.0 m and no grid. Run 1.5.2: slope 1:4 , B1=1.5 m, $L_{b,m}$=1.0 m and with grid)

4.3.2. Horizontal flow structure

The effect of the grid elements on the flow was first tested by dye injection just upstream of the lateral expansion. Figure 4.30 shows that vortices are shed from the grid elements. Based on the dye injection it seems that the vortices do not merge and dissipate in downstream direction. This was also expected in the literature study for a grid solidity of $So = 0.12$. Furthermore, it can be seen that the flow pattern downstream of the grid elements is similar to the vortex street that is depicted in Figure 2.18.

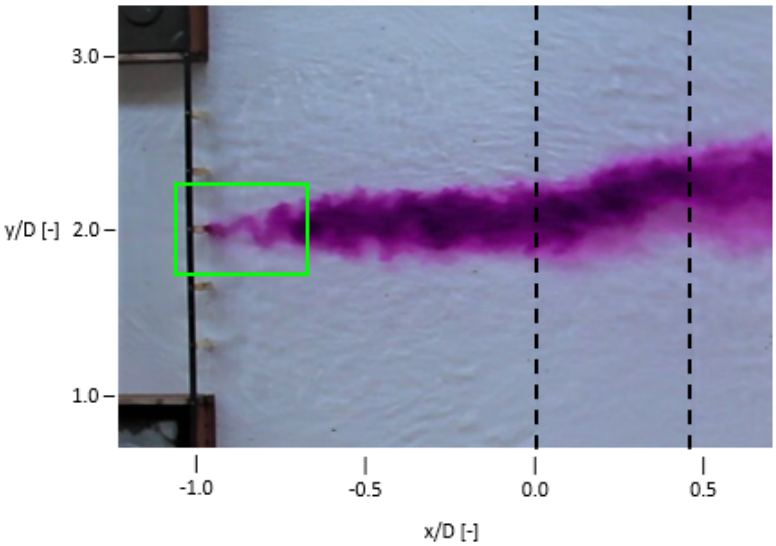

Figure 4.30: Vortex shedding from a grid element indicated by the green square. (Run 2.5.2: slope 1:6, B1=1.0 m, $L_{b,m}$=1.0 m and with grid)

PIV measurements show that only small deviations in the mean surface flow are present between corresponding experimental runs with and without grid turbulence, with exception of the experiments in which the lateral expansion is located at x=0 m. As an example, Figure 4.31 shows the mean surface flow of Run 2.5.3 with grid turbulence. The mean surface flow of its corresponding experiment without grid turbulence was given in Figure 4.8.

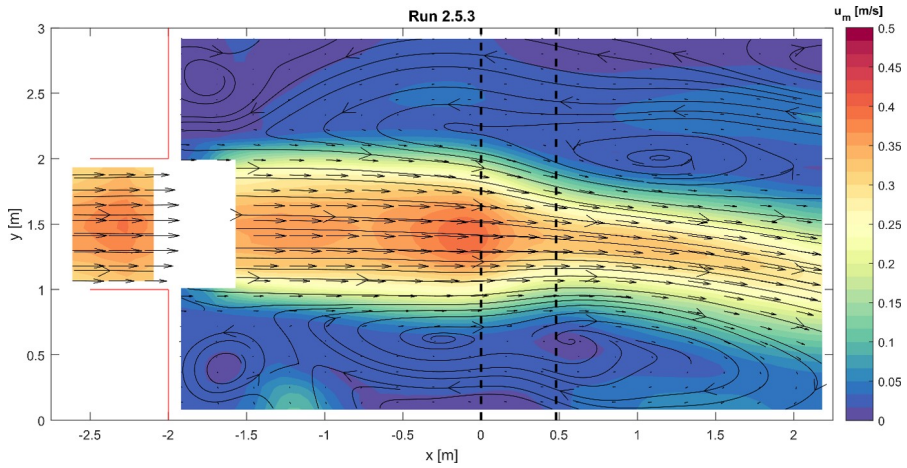

Figure 4.31: Representative mean surface velocity for experimental runs with grid elements positioned 1 or 2 m upstream of the downward slope. (Run 2.5.3: slope 1:6, B1=1.0 m, $L_{b,m}$=2.0 m and with grid)

The following observation is made when comparing Run 2.5.3 (Figure 4.31) to Run 2.4.3 (Figure 4.8):

- *Decreased velocity of the jet centre.* The overall surface velocity of the jet centre in the experimental run with grid turbulence (Run 2.5.3) is slightly smaller compared to its corresponding experiment without grid turbulence (Run 2.4.3). As a possible explanation, an increase in vertical mixing by the grid elements could result in a more depth uniform flow and thus a lower velocity at the surface.

The decreased velocity of the jet centre is clearly observed when plotting several streamwise velocity profiles near the location of the downward slope, see Figure 4.32. The streamwise velocity profiles show a decrease of the peak surface flow velocity of the jet for the experimental runs with grid turbulence.

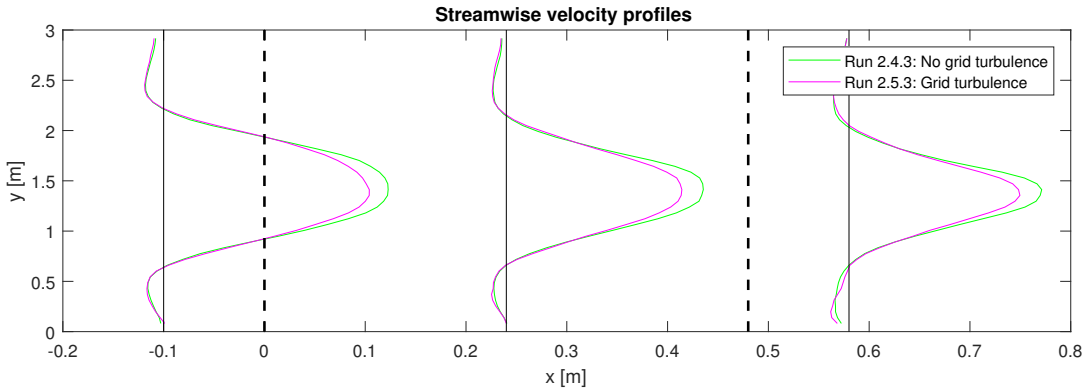

Figure 4.32: Example of the influence grid turbulence on the streamwise velocity profiles for Run 2.4.3 and Run 2.5.3. These experiments resulted in vertical flow attachment of the jet flow. (Run 2.4.3: slope 1:6 , B1=1.0 m, $L_{b,m}$=2.0 m and no grid. Run 2.5.3: slope 1:6 , B1=1.0 m, $L_{b,m}$=2.0 m and with grid)

The horizontal flow structure of experiments with grid turbulence in which the lateral expansion is located at x=0 m (Flow attachment: Category 2) was previously discussed in subsection 4.2.1.

4.3.3. Conclusions

The grid turbulence that is generated by the pillars of the barrier was simulated in the experiments by means of a simplified grid. To correctly scale this process, the grid solidity was used as the main scaling parameter. All experimental runs with a lateral expansion were tested with and without the grid elements to investigate the influence of grid turbulence.

ADV data in the centerline of the flume show that the mean vertical flow profile is barely affected by grid turbulence for experiments in which the grid is located at 1 or 2 m upstream of the downward slope. Compared to the corresponding experimental runs without grid elements only small deviations in the flow velocity are found 10 cm upstream of the slope, see Figure 4.26 and Figure 4.28. The experiments in which the grid is located directly upstream of the slope ($L_{b,m}$=0.0 m) all resulted in vertical flow attachment of the jet flow. For these experiments, the mean vertical flow structure significantly differs from the corresponding experimental runs without grid elements. This enforces the expectation that vertical flow attachment in these experimental runs is not caused by an additional acceleration through conservation of potential vorticity. A possible explanation for the flow attachment of experiments assigned to category 2 could be that the grid elements locally disturb the boundary layer resulting in an increase of vertical mixing near the bottom. These additional vertical fluctuations then possibly result in attachment of the boundary layer to the slope. Another possible explanation is that the grid elements accelerate the flow directly upstream of the slope. This additional acceleration could be large enough to counteract the adverse pressure gradient that causes vertical flow separation.

Visualisation by dye injection showed that vortices are shed from the grid elements. Based on the solidity of the grid, it was in subsection 2.3.5 expected that the eddies that are formed do not merge and grow into large-scale coherent structures. This was indeed verified by visual inspection during the laboratory experiments. Additionally, seeding with tracer particle showed that wakes are present in the lee of the grid elements, resulting in a locally reserved flow direction. The effect of grid turbulence on the horizontal structure of the flow was also studied by the mean surface flow obtained from the PIV measurements. The experiments with grid turbulence in which the lateral expansion was located 1 or 2 m show small deviations from the corresponding experimental runs without grid elements. A slight decreased overall surface velocity of the jet centre was found for experiments that included grid turbulence. Furthermore, it was found that the horizontal structure of the surface flow of the experiment in which the grid is positioned directly upstream of the slope (Flow attachment: Category 2) significantly differs from all other experimental runs with a lateral expansion. Representative for these experimental runs, Figure 4.10 shows that the mean surface flow decreases to about half the upstream flow velocity and does not increase again in downstream direction.

In conclusion, the mean flow field of experiments in which the lateral expansion is located at a distance from the downward slope only shows minor differences between experimental runs with and without grid turbulence. As these experiments best represent the situation near the ES-SSB, it is expected the grid turbulence that is generated pillars of the barrier does not largely affect the mean flow condition.

4.4. Estimation of the bed shear stresses

So far, the flow conditions have been described that were measured in the laboratory experiments. To gain more insight into the development of the scour holes near the ES-SSB, a next step would be to consider the load that is acting on the bed. To study the impact of the flow conditions on scour development the bed shear stresses in the experiments were estimated. Two methods were used to estimate the bed shear stresses in the vicinity of the downward slope: the Reynolds shear stress τ_{xz} and the turbulent kinetic energy (TKE) E.

$$\tau_{xz} = -\rho_w \overline{u'w'} \tag{4.3}$$

$$E = \frac{1}{2}\rho_w\left(\overline{u'^2} + \overline{v'^2} + \overline{w'^2}\right) \tag{4.4}$$

In the above expressions, the prime and the overbar denote the fluctuating component and the time average of the total velocity signal after Reynolds decomposition. For the second method, a linear relation is assumed between the TKE and the bed shear stress, namely: $\tau_0 = CE$ (Soulsby, 1981). In this expression, the empirical coefficient C was found to be 0.19 for complex flow fields (Biron et al., 2004).

Comparison between reference cases

The Reynolds shear stress and TKE of the reference cases are depicted in Figure 4.33. These results will be used as a reference level in comparisons between other experimental runs in this section.

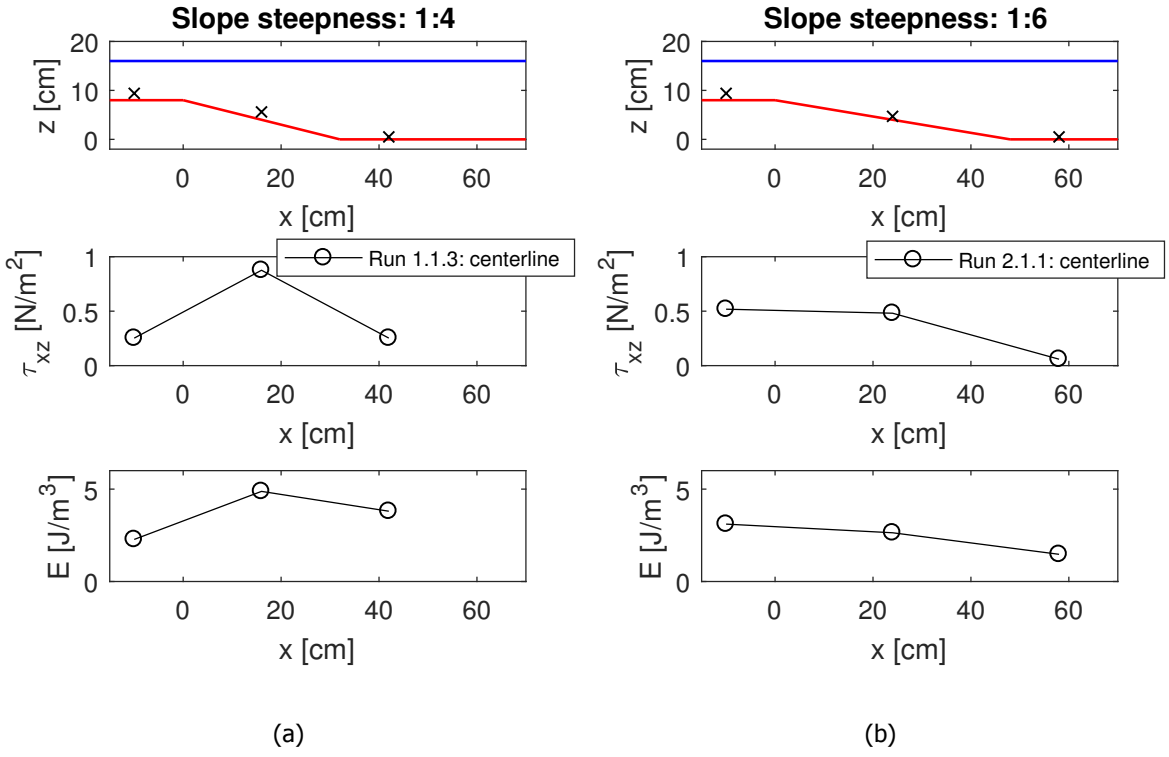

Figure 4.33: The Reynolds stress τ_{xz} and the TKE for the reference cases. Both experiments were performed with a discharge of 80 l/s and resulted in vertical flow separation. The upper panel in the subplots indicates the position of the measurement points. (a) Run 1.1.3: slope 1:4, B1=3.0 m and no grid. (b) Run 2.1.1: slope 1:6, B1=3.0 m and no grid.

The following observations are made from Figure 4.33:

1. The reference case of the 1:4 downward slope shows an increase in the Reynolds shear stress and TKE at the location of the slope compared to the upstream measurement point. The Reynolds shear stress decreases again downstream of the slope, while the TKE remains relatively high.
2. In the reference case of the 1:6 downward slope the Reynolds shear stress and TKE both decrease in downstream direction. For the downstream measurement point, the Reynolds shear stress decreases to nearly zero and the TKE is about half the intensity measured upstream of the slope.
3. Comparing the reference cases of the 1:4 and 1:6 downward slope, it can be seen that for the majority of the measurement points the Reynolds shear stress and the TKE are higher for the reference case with the 1:4 slope.

Comparison between vertical flow states

To investigate the effect of the vertical flow state on the bed shear stresses in the centerline and mixing layer experimental runs with vertical flow separation of the jet centre and vertical flow attachment of the jet flow are compared. An example of such a comparison is depicted in Figure 4.34. Two similar comparisons between experimental runs with vertical attached and separated flow are presented in Figure D.1 and Figure D.2. As a reference level Figure 4.34 also includes the estimation of the bed shear stresses of Run 2.1.1.

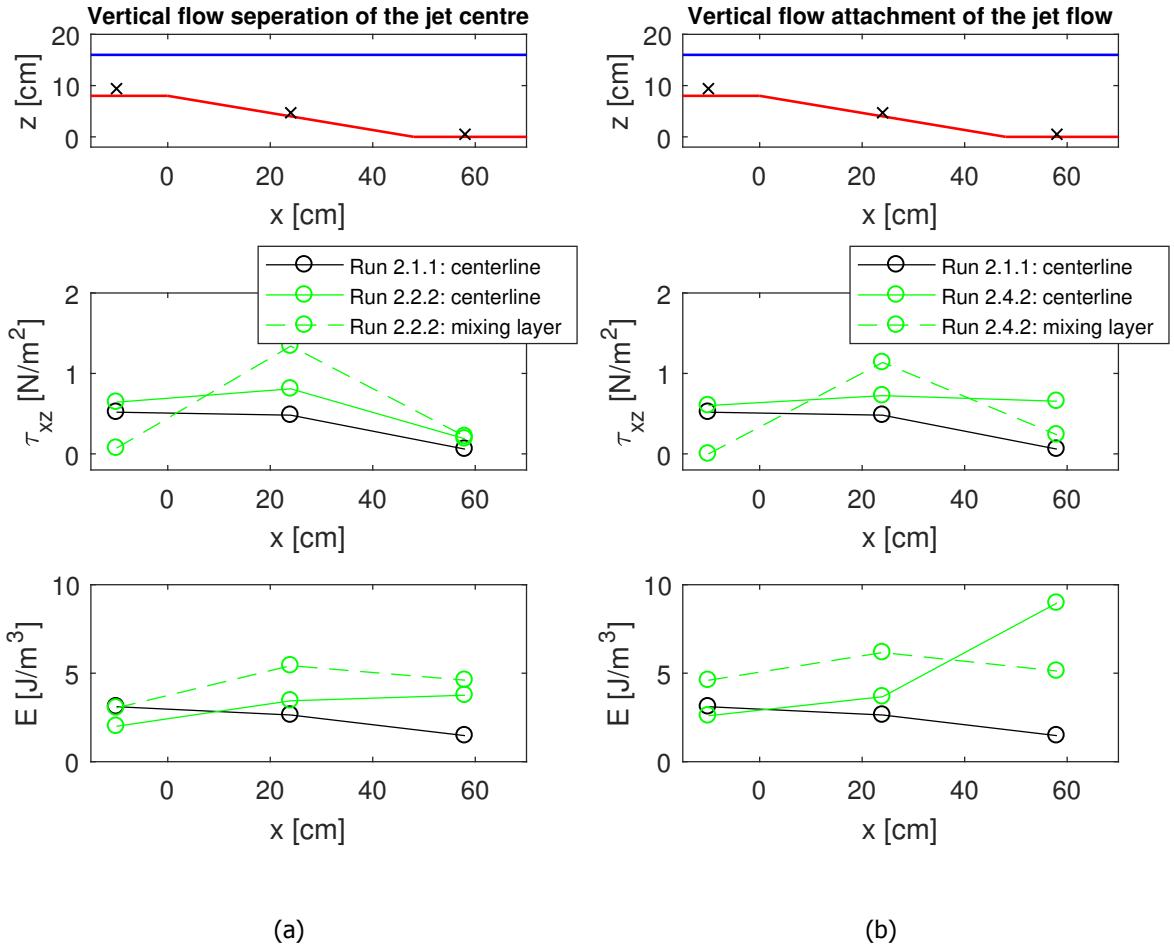

Figure 4.34: The Reynolds stress τ_{xz} and the TKE for experimental runs representative for vertical flow separation of the jet centre and vertical flow attachment of the jet flow. The only geometric difference in the setup is the upstream flow width. (a) Vertical flow separation (Run 2.2.2: slope 1:6, B1=1.5 m, $L_{b,m}$=1.0 m and no grid). (b) Vertical flow attachment (Run 2.4.2: slope 1:6, B1=1.0 m, $L_{b,m}$=1.0 m and no grid).

The following observations are made from Figure 4.34:

1. The Reynolds shear stress, as well as the TKE, are nearly equal between the experimental runs with vertical flow separation of the jet centre and vertical flow attachment of the jet flow for the upstream and middle measurement points.
2. Both the Reynolds shear stress and the TKE of the downstream measurement point in the centerline increase in the case of vertical flow attachment compared to the experimental runs with vertical flow separation of the jet centre.
3. The Reynolds shear stress and TKE are nearly equal for the downstream measurement point in the mixing layer.
4. The Reynolds shear stress in the middle measurement point shows a significantly larger increase compared to the TKE.

Comparison between experiments with and without grid turbulence

Lastly, the effect of grid turbulence on the bed shear stresses is investigated by comparing corresponding experimental runs with and without grid elements, see for instance Figure 4.35. Two more examples of comparisons between experimental runs with and without the influence of grid turbulence are depicted in Figure D.3 and Figure D.4. As a reference level Figure 4.35 also includes the estimation of the bed shear stresses of Run 1.1.3.

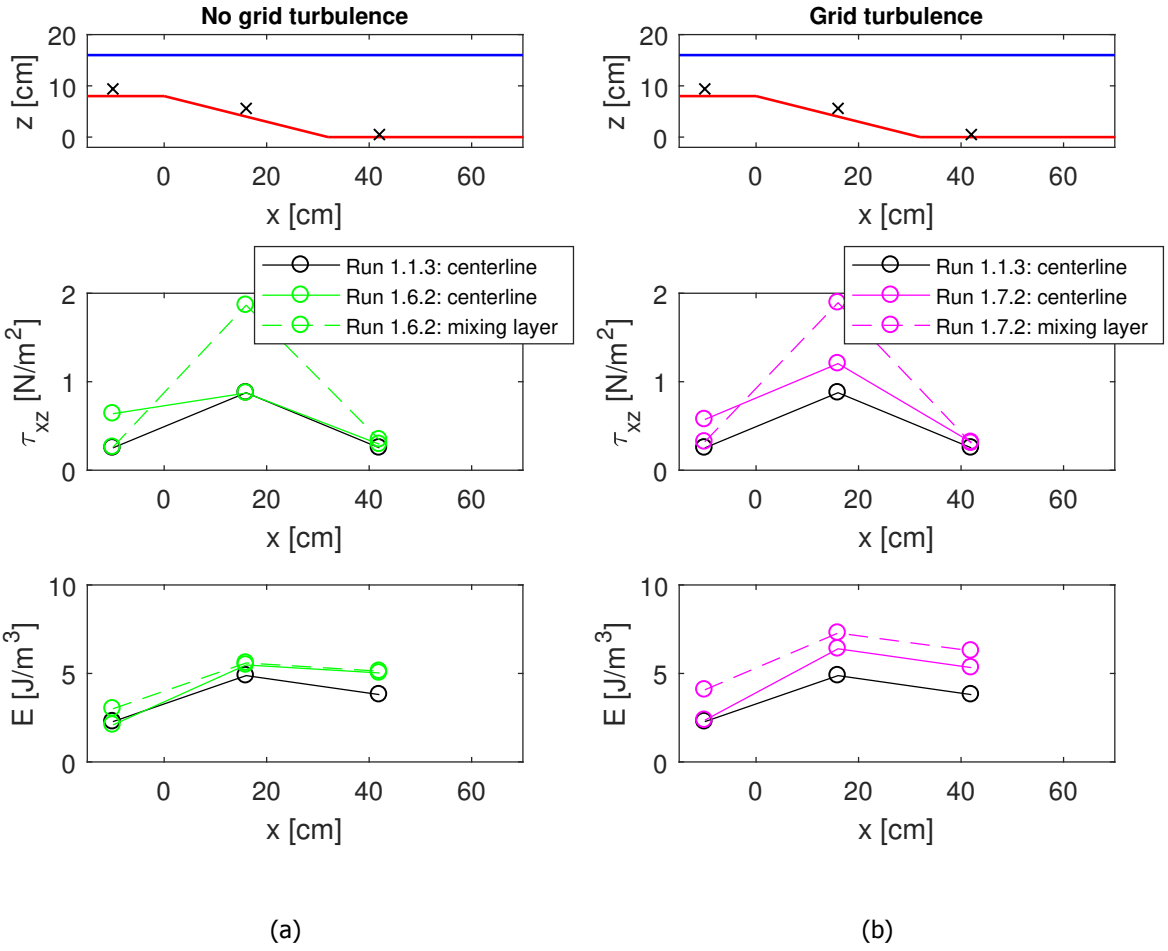

Figure 4.35: Representative change of the Reynolds stress τ_{xz} and the TKE for experimental runs with and without grid turbulence. (a) Experimental run without the effect of grid turbulence (Run 1.6.2: slope 1:4, B1=2.0 m, $L_{b,m}$=1.0 m and no grid). (b) Experimental run including grid turbulence (Run 1.7.2: slope 1:4, B1=2.0 m, $L_{b,m}$=1.0 m and with grid).

The following observations are made from Figure 4.35:

1. The Reynolds shear stress between the experiments are nearly identical with only a significantly higher value of τ_{xz} in the middle measurement point in the centerline for the experimental run with grid turbulence.
2. The TKE for the experiment with grid turbulence is higher for all measurement points in the mixing layer.
3. Based on the Reynolds shear stress τ_{xz} and the TKE, the largest bed shear stress on the downward slope are found at the location of the mixing layer. This can also be observed in Figure 4.34.

4.4.1. Conclusions

This subsection discusses the comparisons that were made in section 4.4 in more detail. Possible explanations are given for the observed difference between the experimental runs.

Comparison between reference cases

For the reference cases, it would be expected that the Reynolds shear stress and the TKE for the measurement point upstream of the slope would approximately be equal as similar flow conditions were maintained in the reference cases (an equal average upstream flow velocity and an uncontracted setup). For the upstream measurement point, the Reynolds shear stress of the 1:6 reference case is higher compared to the reference case with the 1:4 slope. The difference cannot be explained but could result from inaccuracies of the measurement technique. All observations in the remainder of this section should therefore be treated with caution.

Visual inspection showed the presence of a vertical recirculation zone in the 1:4 reference case. It was observed that a strong return flow was present near the bed at the location of the downward slope. In the case of the 1:6 reference case, the flow velocities in the vertical recirculation zone were more moderate and the flow nearly came to a stagnation point. This has an effect on the bed shear stresses. From Figure 4.33 it can be seen that the Reynolds shear stress and the TKE are higher for the steeper 1:4 slope. Similar results were found in previous experiments by Broekema (2017a) for uncontracted cases with a 1:2 and 1:4 slope.

Comparison between vertical flow states

In the case of vertical flow attachment of the jet flow, higher flow velocities reach the bed near the downward slope. It is expected that this results in a larger load on the bed which could be demonstrated by an increase in the bed shear stresses near the downward slope.

Figure 4.34 shows that the Reynolds shear stress and the TKE for the upstream and middle measurement point in the centre of the flume are almost identical for the different flow state. A possible explanation could be that in Run 2.2.2 (Figure 4.34a) the flow remained vertically attached to the upstream part of the downward slope and that the separation point is located between the middle and downstream measurement point. The downstream measurement point does show a significant increase in τ_{xz} and the TKE between the two experimental runs. This strengthens the expectation that a vertically attached flow results in higher bed shear stresses and can enhance scour development. Additionally, Figure 4.34a shows that no large differences are found for the Reynolds shear stress and the TKE in the mixing layer. This can be explained by the fact that in both experimental runs the flow remains attached in the at this location.

Although in Figure 4.34a the influence of vertical flow attachment was clearly noticeable by an increase of the Reynolds shear stress, the other two comparisons between the vertical flow states depicted in Figure D.1 and Figure D.2 show smaller differences for τ_{xz}. In general, the effect of vertical flow attachment of the jet flow is more obvious from a significant increase in the TKE.

Comparison between experiments with and without grid turbulence

To the author's best knowledge, the effect of grid turbulence on scour hole development has not been described in literature before. Comparisons of corresponding experimental runs with and without grid

elements show that grid turbulence, to a limited extent, influences the bed shear stresses near the downward slope. The effect of grid turbulence is best observed by an increase of TKE in the mixing layer, as shown in Figure 4.35. Only moderate deviations in the Reynolds stress τ_{xz} are found between experimental runs with and without grid turbulence. In comparison with the expression for the TKE, the Reynolds shear stress τ_{xz} does not include the effect of lateral velocity fluctuations w'. These could be more significant in experiments in which grid turbulence is included.

5

Discussion

This chapter discusses the selection and the limitations of the scale model that was used to reproduce the flow conditions near the ES-SSB. It addresses how the results that were obtained with the model can be interpreted as well as their shortcomings. Lastly, this chapter relates the observed flow conditions in the model to the development of the scour holes near the ES-SSB.

5.1. Selection and limitations of the scale model

In section 2.1 it was shown that various elements and processes influence the flow field in the vicinity of the ES-SSB and its scour holes. Through an extensive field campaign to the flow conditions near the ES-SSB of Rijkswaterstaat, the Dutch ministry of public works, and an analysis of the obtained velocity data by Broekema (2016) several hydrodynamic characteristics were identified.

Near the ES-SSB, a deceleration of the flow results from a sudden depth increase caused by the scour holes. As a consequence, the flow separates from the bed at certain stages in a tidal cycle. A vertical recirculation zone then forms on the upstream scour slope in which relatively low velocities near the bed persist. At other stages in the tidal cycle, however, it is observed that the flow remains vertically attached to the upstream scour slope resulting in relatively high near-bed velocities. These high near-bed velocities are accompanied by large bed shear stresses that could explain the ongoing scour near the ES-SSB.

Vertical flow attachment in a scour hole is accompanied by a lateral gradient in the barrier's outflow, a contraction of the flow at the end of the bed protection and the formation of large-scale gyres. In addition, the flow conditions near the ES-SSB can be regarded as shallow as the horizontal dimensions largely exceed the local water depth. Lastly, the grid turbulence that is generated by the pillars of the barrier was named as a leading characteristic that determines the flow field near the ES-SSB. These observations have formed the starting point for the experimental setup.

To systematically investigate the flow characteristics that are observed near the inlet sections of the ES-SSB in a scale model, a schematisation of the flow field was required. To correctly reproduce the essential flow processes in a scour hole near the barrier, a scale model should at least include a lateral velocity gradient in the base flow, a local uniform depth increase, a domain in which the horizontal dimensions largely exceed the water depth and an object that results in the generation of grid turbulence. These elements are discussed below:

1. *Lateral velocity gradient.* A lateral gradient in the base flow was obtained by a sudden widening of the incoming flow. In literature, this geometry is often referred to as a shallow lateral expansion (SLE) and was for example studied by Talstra (2011). In contrast to experiments by Talstra (2011), the experimental setup that used for this research thesis included a lateral expansion on both sides of the incoming flow. During the preliminary experiments it was found that wall effects influenced the flow in an asymmetric experimental setup, and therefore it was decided to use a

symmetrical geometric layout. In the conducted experiments, it was found that at the location of the lateral expansion two horizontal mixing layers developed, one on each side of the incoming flow. This resulted in the formation of a jet that can also be observed near the inlet sections of the ES-SSB. Additionally, it was for all experiments found that in the lee of the contracting elements steady gyres were present. These large-scale gyres can also be observed adjacent to the outflow of barrier's inlet sections.

2. *Local uniform depth increase.* In the scale model, a local uniform depth increase was used to reproduce the effect of the upstream scour slope. Although the upstream scour slopes near the ES-SSB have a complex geometry, it was decided to simulate these in the model by a straight downward slope. By using a straight downward slope it was possible to systematically investigate the effect of the slope steepness on the flow conditions. In the model, the flow experienced an abrupt increase in water depth at the location of the slope. This sudden increase in water depth is also observed at the downstream end of the bed protection of the ES-SSB where the scour holes have developed. One of the limitations of the scale model, however, is that the lower part of the upstream slope scour slope is not correctly reproduced. Near ES-SSB the water depth gradually increases to the deepest point of the the scour holes. This gradual increase of the water depth is not present in the scale model. Therefore, the flow conditions near the lower half of the downward slope could deviate from the situation observed in the prototype as streamlines near the bottom are stronger curved.

3. *Shallow flow conditions.* In section 2.3 it was explained that the flow near the ES-SSB can be characterised as a shallow flow. Subsequently, it was in subsection 2.3.1 shown that shallow conditions initiate the formation of two-dimensional coherent structures in the flow that can significantly contribute to the transverse exchange of momentum and mass. In the scale model, shallow flow conditions were obtained as the width and length of the flume were significantly larger than the water depth. Visual inspection revealed that large-scale structures were present in the scale experiments. Important processes such as the development of eddies in the horizontal mixing layers and vortex merging (see Figure B.5) were identified. These could also play an important role in the flow field near the ES-SSB.

4. *Grid turbulence.* The grid turbulence that is generated by the pillar of the ES-SSB was in the scale model reproduced by an array of square beams with an equal centre-to-centre distance. The complex geometry of the pillars of the barrier was not included in the scale model. Scaling of the grid turbulence was based on the solidity of the grid and the water depth, see subsection 3.2.4. The experiments that included grid turbulence all showed that wakes formed in the lee of the grid elements. These wakes are also observed near the pillars of the ES-SSB. As it was found that grid turbulence mainly affects the near-flow field it is not expected that the simplification of the geometry of the pillars significantly affects the results of the scale experiments.

To isolate the flow processes that are observed near the ES-SSB several simplifications were made in the layout of the scale experiment. These simplifications were previously addressed in subsection 3.1.1 and will be further discussed in the remainder of this section.

- *Bathymetry.* In the scale experiment, only one of the inlet sections of the ES-SSB was considered. Therefore, the model ignored the outflow of two other inlet sections. As the width of the mouth of the Eastern Scheldt is large compared to the length of the bed protection, it is not expected that the outflow of the inlet sections interacts in the near-field and thereby influences the flow conditions in other scour holes. Secondly, the scale model does not take into account aspects such as the upstream scour hole, the complex geometry of the downstream scour hole, tidal channels, bed protection elements and bedforms. These aspects were ignored to systematically investigate and isolate the influence of the experimental variables that were described in section 3.3. Including the above aspects in an experimental setup would be interesting for further research. First of all, the additional effect of the tidal channel or side slopes of the scour hole could contribute to the persistence of a lateral gradient in the outflow which is characteristic for the ES-SSB. Secondly, the bottom of the current scale model can be considered to be hydraulically smooth. As the size of bed protection elements is large with respect to the thickness of the

viscous sub-layer, using a hydraulically rough surface in the experiments would better represent the properties of the ES-SSB.

- *Constant and unidirectional flow.* In the scale experiments, a constant discharge was used to reproduce the flow conditions near the ES-SSB. The influence of the M2-tide, which is the most dominant tidal constituent of the North Sea, is therefore completely ignored. In subsection 2.3.3 it was shown that, based on the inlet Strouhal number, starting jet vortices are expected to escape the reversing tidal flow and thus do not affect the flow near inlet sections at subsequent stages in the tidal cycle (Del Roure et al., 2009). Furthermore, the scale model ignores the reversal of the flow direction. This does not influence the results since the scale model, at all times, considered the downstream scour hole. Reversal of the flow direction could be of importance in a scale model that includes an erodible bed. Back-filling of the scour hole is then be a process that should be considered.

- *Geometry of the barrier.* Besides a simplified geometry of the pillars, the scale model did also not include the effect of the barrier's sill. It is expected that the sill does influence the flow conditions directly nearby barrier, however, these disturbances are most likely damped out when the flow reaches the end of the bed protection.

- *Fixed, non-erodible bottom.* Since this thesis specifically focuses on the hydrodynamic processes that contribute to the development of scour holes, it was decided to use a fixed, non-erodible bottom in the experimental setup. The scale model therefore ignores the presence of bedforms and the evolution of the scour hole. Additional research with an experimental setup that includes an erodible bed could give insight in the development of scour holes in which the flow remains vertically attached. This could help to understand the scour process that is observed near the ES-SSB.

5.2. Interpretation of the results

This section discusses the vertical flow structure, the horizontal flow structure and the influence of grid turbulence that were observed in the scale experiments and relates these to the flow conditions near the ES-SSB.

5.2.1. Vertical flow structure

As described in section 4.1, two vertical flow states were observed during the laboratory experiments at the location of the downward slope: vertical flow attachment along the full width of the jet flow and vertical flow separation of the jet centre. A schematic overview of these observed vertical flow states is given in Figure 4.1.

For five experimental runs (assigned to "Flow attachment: Category 1" in subsection 4.1.1) it was expected that vertical flow attachment of the jet flow resulted from an additional acceleration through conservation of potential vorticity. The principle of conservation of potential vorticity was explained in subsection 2.2.5. In addition to a lateral velocity gradient, it was found that important geometric aspects that contribute to vertical flow attachment at the downward slope are a mild slope steepness and a relatively low ratio of the upstream flow width over the width of the contracting elements $B1/D$. For the experimental runs in flow attachment category 1, these variables were equal to 1:6 and 1, respectively. An important observation that follows from the ADV measurements is that in the case of vertical flow attachment the velocity is approximately uniform over the water depth, see Figure 4.3. For five experimental runs assigned to "Flow attachment: Category 2" it was expected that the attachment of the flow resulted from an effect of the grid elements, which in all these experiments were positioned directly upstream of the downward slope. Possible explanations for the attachment of the flow in these experiments were discussed in subsection 4.3.3.

The majority of the conducted experiments resulted in vertical flow separation of the centre of the jet at the location of the downward slope. It was found that ADV measurements did not indicate the presence of a return current, while during most experiments this was observed with dye injection. Another important process that was identified by visual inspection is that the separation point could also be

located along the downward slope instead of at the upstream edge, see Figure 4.6. This process was not quantitatively measured with the ADV technique. A detailed look at the upper subplot in Figure 2.4 reveals that the flow at the upstream part of the scour slope of Roompot East also remains attached to the bed, while at the lower half of the slope a vertical recirculation zone is present.

Overall, the laboratory experiments have successfully reproduced the vertical flow conditions that are observed on the upstream scour slope in scour holes near the ES-SSB.

5.2.2. Horizontal flow structure

The horizontal flow structure reveals that a contraction of the flow at the location of the downward slope is observed for all experimental runs, even for the references cases which did not contain any horizontal contracting elements. From the reference cases, it was concluded that a local depth increase bordered by two wall boundary layer already results in the contraction of a flow. Furthermore, the reference cases indicate that small disturbances near a local depth increase can already significantly impact the horizontal structure of a shallow flow.

For the experiments assigned to flow attachment category 1, it was expected that an additional acceleration through conservation of potential vorticity counteracted the adverse pressure gradient that in other experimental runs resulted in vertical flow separation at the downward slope. Under the assumptions that the lateral velocity of a flow field is much smaller than the streamwise velocity, inviscid flow and low friction, it was in subsection 2.2.5 shown that the expression of conservation of potential vorticity can be reduced to ω/h =constant along a streamline (Broekema, 2017b). From Figure 4.9, which is representative for the mean vertical vorticity of flow attachment category 1, it can be seen that the vertical vorticity decreases for a deepening shallow flow. This is not in line with the above as the vertical vorticity should increase downstream of the slope. Although vertical flow attachment was observed in the scale experiments, it can with this simplistic approach not be proven that the vertical attachment results from an additional acceleration through conservation of potential vorticity. The influence of the lateral velocity and bottom friction in the current experiment can possibly not be considered as small, such that the assumptions stated above do not hold.

Results of experiments with a lateral velocity gradient in the base flow have shown that convergence of the flow near a local uniform depth increase is not a necessary characteristic for vertical attachment of a jet flow, but may also be observed in the case of vertical flow separation of the jet centre. This is in contrast to experimental results of Broekema (2017a) in which divergence of the flow was found for vertically separating flows. Contraction of the flow in experimental runs with vertical flow separation of the jet centre is explained to result from flow attachment in the horizontal mixing layers. As a possible explanation, a lateral velocity gradient in the mixing layers could locally accelerate the flow through conservation of potential vorticity. This acceleration, however, is then insufficient to accelerate the centre of the jet flow such that the flow remains attached over the full width of the jet flow. Again, conservation of potential vorticity in the horizontal mixing layers could not be proven from the mean surface velocity measurements obtained with PIV. Possibly other hydrodynamic processes are of importance that today are not yet fully understood.

A detailed study to the mean streamwise surface flow in subsection 4.2.3 has shown that no deviations can be distinguished between experiments with vertical attachment of the jet flow and vertical separation of the jet centre.

5.2.3. The effect of grid turbulence

The influence of the grid turbulence on the vertical and horizontal structure of the flow was addressed in section 4.3 by comparing corresponding experimental runs with and without grid elements. From ADV measurements in the centerline of the flume, it was concluded that if the grid elements were located 1 or 2 m upstream of the downward slope, then the mean vertical flow conditions barely deviate from the corresponding experimental run without grid turbulence. Also, PIV measurements of these experimental runs show that only small differences can be observed for the mean surface flow, namely a slightly decreased overall surface velocity of the jet centre. Visual inspection showed that wakes formed in the lee of the grid elements. Vortices that are shed from the grid elements were not found

to merge and grow into large-scale coherent structures, as was expected based on the solidity of the grid in subsection 2.3.5.

In contrast to the above, the majority of the experiments in which the grid was positioned directly upstream of the downward slope showed a clear difference in the vertical and horizontal flow structure with corresponding experiments without grid turbulence. Since all experimental runs in which the grid was located directly upstream of the downward slope resulted in vertical flow attachment, it was expected that another generation mechanism was responsible for the favourable pressure gradient that counteracted vertical flow separation. These experiments were therefore assigned to flow attachment category 2. Possible explanations for the flow attachment of experimental runs assigned to category 2 were mentioned in subsection 4.3.3. It is expected that the flow attachment observed in category 2 is not representative for the vertical flow conditions near the ES-SSB, as the pillars of the barrier that generate the grid turbulence are located at a certain distance from the scour holes.

5.3. Consequences for scour

In section 4.4 two methods were used to relate the flow conditions that were measured in the scale experiments to bed shear stresses. These are the Reynolds shear stress τ_{xz} and the turbulent kinetic energy (TKE). Comparisons between experimental runs were made to investigate the influence of the slope steepness, the vertical flow state and grid turbulence on the bed shear stress.

First of all, a comparison between the reference cases shows that higher Reynolds shear stresses and intensities of TKE can be found for a 1:4 slope compared to a 1:6 slope. From visual inspection with dye, it was concluded that return currents were present at the downward slope of the 1:4 reference case. In the case of the 1:6 slope, a stagnant flow was observed that could explain the decrease in the estimation for the bed shear stresses. Secondly, comparisons between experiments with different vertical flow states showed increased values of the Reynolds shear stress and TKE for experimental runs with vertical flow attachment of the jet flow in the centerline of the flume downstream of the slope. This strengthens the expectation that vertical flow attachment in the scour holes of the ES-SSB can enhance scour development. Lastly, the impact of grid turbulence on the bed shear stresses was investigated by comparing corresponding experimental runs with and without grid elements. Based on increased intensities of the TKE, it was concluded that grid turbulence mostly contributes to higher bed shear stresses in the horizontal mixing layers.

6

Conclusions and recommendations

The objective of this master thesis is to obtain more fundamental understanding of the flow patterns and turbulence structure in the vicinity of tidal barriers, such as the Eastern Scheldt storm surge barrier, and how these may contribute to ongoing scour. The research focused on the following main research question:

What are the effects of a lateral velocity gradient and grid turbulence on the flow conditions in and near a downstream scour hole of an open structure tidal barrier, and how may this affect scour development?

Four sub-questions were formulated in order to answer the main research question:

1. How can the hydrodynamic conditions that are characteristic for the flow field near the ES-SSB be reproduced in a scale experiment?
2. How do a lateral velocity gradient and grid turbulence affect the vertical structure of the flow field, and what is the effect of the vertical flow state on the horizontal structure of the flow?
3. How does grid turbulence influence the flow field in the model?
4. How can the flow conditions observed in the scale experiment be related to scour development?

In section 6.1 the research questions of this master thesis are answered. In addition, recommendations for further research are proposed in section 6.2.

6.1. Conclusions

Before the main research question is answered, this section first addresses the sub-questions.

Sub-question 1: How can the hydrodynamic conditions that are characteristic for the flow field near the ES-SSB be reproduced in a scale experiment?

- In section 2.1 it was shown that the flow near the ES-SSB is characterised by a lateral gradient in the barrier's outflow, a contraction of the flow at the downstream end of the bed protection, the formation of large-scale gyres, grid turbulence and shallow flow conditions.
- For certain stages in the tidal cycle, vertical flow attachment is observed on the upstream slope of the downstream scour holes.
- A schematisation of the flow field near the ES-SSB was required to systematically investigate the flow conditions in a scale model.
- The used schematisation included a lateral velocity gradient in the base flow, a local uniform depth increase, a domain in which the horizontal dimensions largely exceed the water depth and grid turbulence. These conditions were reproduced by an abrupt expansion of the flow width, a

straight and linear sloping downward slope, selection of a flume with suitable dimensions and an array of objects with equal spacing, respectively.

Sub-question 2: How does a lateral velocity gradient in the base flow affect the vertical structure of the flow field, and what is the effect of the vertical flow state on the horizontal structure of the flow?

- The experiments that include a lateral flow expansion showed vertical flow separation or attachment of the jet centre at the location of the downward slope. For all experiments, it was found that in the horizontal mixing layers of the jet, where relatively the large lateral gradients are present, the flow remained vertically attached to the downward slope.
- In combination with a lateral velocity gradient, it was found that important geometric aspects that contribute to vertical flow attachment are a mild slope steepness and a relatively low ratio of the upstream flow width over the width of lateral expansion.
- A contraction of the flow at the location of the downward slope was observed in all experiments.
- It could not be proven that an acceleration through conservation of potential vorticity resulted in vertical flow attachment at the location of the downward slope.
- No clear difference in the mean surface flow was found between experiments that resulted in vertical flow separation or attachment of the jet centre.

Sub-question 3: How does grid turbulence influence the flow field in the model?

- Experimental runs in which the lateral expansion and the grid elements were positioned 1 or 2 m upstream of the downward slope only show a slight reduction of the mean surface flow velocity in the jet centre compared to the corresponding experiments that exclude grid turbulence.
- Visual inspection revealed that the vortices that were shed from the grid elements did not merge and grow into large-scale coherent structure, as was expected based on the solidity of the grid.
- All experimental runs in which the grid was positioned directly upstream of the downward slope resulted in vertical flow attachment of the jet centre. These experiments are not representative for the flow near the ES-SSB as the scour holes are located a certain distance from the barrier.

Sub-question 4: How can the flow conditions observed in the scale experiment be related to scour development?

- Two methods were used to relate the measured flow conditions in the model to bed shear stresses: the Reynolds shear stress τ_{xz} and the turbulent kinetic energy.
- A comparison of the reference cases shows higher estimations for the bed shear stress at a 1:4 slope compared to a 1:6 slope.
- Comparisons of experiments with vertical flow separation and attachment of the jet centre reveal that higher bed shear stresses can be found in the centerline of the flume downstream of the downward slope for vertically attached flows. This strengthens the expectation that vertical flow attachment can enhance scour development.
- Based on large intensities of the TKE, it is concluded that grid turbulence mostly contributes to higher bed shear stresses in the horizontal mixing layers.

Taking into account the above sub-questions, the main research question is answered as follows:

Research question: What is the effect of a lateral velocity gradient and grid turbulence on the flow conditions in and near a downstream scour hole of an open structure tidal barrier, and how may this affect scour development?

In this master thesis, a scale experiment was designed to investigate the influence of hydrodynamic conditions, that are representative for the flow field near the ES-SSB, on scour hole development. A

schematisation of the flow field near the ES-SSB was required to correctly reproduce the essential elements and processes that, based on a performed literature study, were expected to be crucial in understanding the ongoing scour. The schematisation included a lateral velocity gradient, a local uniform depth increase, shallow flow conditions and grid turbulence. The scale experiments have shown that a laterally sheared base flow, that is subjected to a uniform local depth increase, results in a contraction of the flow as it experiences a depth increase. For five experimental runs, it was expected that an acceleration through conservation of potential vorticity could counteract the adverse pressure gradient over the full width of a jet flow, such that the bottom boundary layer remained vertically attached. This could however not be proven based on measurements of the surface flow. From experiments with grid elements, it was concluded that grid turbulence mostly affects the local flow conditions in the vicinity of the grid itself and only results in a small reduction of the overall surface velocity of the jet centre. Estimates of the bed shear stresses reveal that vertical flow attachment results in higher bed shear stresses and can possibly enhance scour development. In addition, it was found that grid turbulence mainly contributes to a higher estimation of bed shear stresses in the horizontal mixing layers.

6.2. Recommendations

Based on the results and findings in this thesis the following recommendations are suggested for extension of the current experiment:

1. For all experimental runs that contained a lateral expansion in the experimental setup a contraction of the flow was observed at the location of the downward slope. In addition, it was found that the flow in the mixing layers remained attached for slope steepnesses of 1:4 and 1:6. To investigate if an acceleration through conservation of potential vorticity and thus a contraction of the flow also occurs for steeper slopes, it is recommended to perform experimental runs with a 1:2 downward slope. It is expected that for steeper slopes than 1:4, the jet flow will eventually show a divergence of streamlines at the location of the downward slope.

2. In the current experimental setup, only the upstream slope of a scour hole was modelled thereby neglecting the complex geometry of the scour hole. To further investigate the effect of the geometry of the scour hole, it is recommended to include the side slopes in the experimental setup. As a first step, it is advised to include side slopes with a constant slope. Including the side slopes could preserve the velocity difference of the jet flow as the deeper part is less influenced by bottom friction compared to the shallow parts.

3. The HPL plates that were used to construct the false bottom can be considered to be hydraulically smooth. To study the effect of the bed protection a hydraulic rough bottom is more realistic. Therefore, it is recommended to apply roughness elements to the surface of the false bottom. A rougher bed results in a higher intensity of vertical mixing near the bottom and can possibly contribute to vertical flow attachment on the downward slope. Furthermore, it was found that the HPL plates deform when being exposed to water or humid conditions. It is not advised to use this material in the experimental setup of subsequent experiments.

4. For the experimental runs assigned to flow attachment category 1 in subsection 4.2.1 it would be interesting to (partially) close sections the middle of the grid to investigate its effect on the vertical and horizontal structures of the flow. Manipulation of the streamwise velocity profile might result in flow conditions that are less accelerated through conservation of potential vorticity such that the flow separates at the location of the downward slope. As was shown in this thesis, vertical flow separation may suppress the scour development. Solutions to mitigate the ongoing scour near the ES-SSB could possibly result from (partially) closing certain gates in the inlet sections.

5. To understand the development of scour holes near the ES-SSB it is advised to perform scale experiments with an erodible bed in which the flow remains vertically attached to the upstream scour slope. Additional insights into the scour process could improve the predictions for the maximum scour depth near the ES-SSB.

Additionally, the following recommendations are made for further research:

1. This master thesis has resulted in a large data set with surface flow velocities that were measured during the scale experiments. Although the evolution of eddies in the horizontal mixing layers was visualised by dye injection and qualitatively described, a quantitative description of their development is still missing. The obtained data can be further used to quantitatively describe the behaviour of coherent flow structures in shallow deepening flows.

2. The conducted experiments have shown that the flow in the horizontal mixing layers remained attached to the downward slope during all experimental runs. It remains unknown if this also occurs in the scour holes near the ES-SSB. It is advised to perform an additional analysis to the field data to investigate if the flow indeed remains attached in the scour holes at the location of the horizontal mixing layers.

3. The surface flow near the grid elements could not be quantitatively measured with particle image velocimetry. It is advised to used another measurement technique to quantitatively describe the surface flow in the vicinity of the grid. Particle tracking velocimetry (PTV) could be a suitable option.

Bibliography

Babarutsi, S., Ganoulis, J., and Chu, V. H. (1989). Experimental investigation of shallow recirculating flows. *Journal of Hydraulic Engineering*, 115(7):906–924.

Battjes, J. A. (2002). *Vloeistof Mechanica*. Delft University of Technology.

Bhuiyan, F., Hey, R. D., and Wormleaton, P. R. (2007). Hydraulic evaluation of W-weir for river restoration. *Journal of Hydraulic Engineering*, 133(6):596–609.

Bijlsma, A., Tralli, A., Verbruggen, W., and de Haas, P. (2017). Detailed hydrodynamics of the Eastern Scheldt storm surge barrier: validation of a CFD approach. *4^{th} International Symposium of Shallow Flows, Eindhoven University Technology*.

Biron, P. M., Robson, C., Lapointe, M. F., and Gaskin, S. J. (2004). Comparing different methods of bed shear stress estimates in simple and complex flow fields. *Earth Surface Processes and Landforms: The Journal of the British Geomorphological Research Group*, 29(11):1403–1415.

Bom, S. (2017). Scour holes in heterogeneous subsoil. Master's thesis, Delft University of Technology.

Breusers, H. N. C. (1966). Conformity and time scale in two-dimensional local scour. *Proc. symposium on model and prototype conformity*.

Broekema, Y. B. (2016). Flow around the Eastern Scheldt storm surge barrier. Technical report, Delft University of Technology.

Broekema, Y. B. (2017a). Experimental log. Technical report, Delft University of Technology.

Broekema, Y. B. (2017b). The role of potential vorticity in shaping the horizontal structure of a tidal jet at deep scour holes. *Unknown*. Unpublished article.

Campbell, K. (2016). An ecology of cloud. Retrieved 2018-03-16, from `https://www.linkedin.com/pulse/ecology-cloud-kord-campbell/`.

Chen, D. and Jirka, G. H. (1995). Experimental study of plane turbulent wakes in a shallow water layer. *Fluid Dynamics Research*, 16(1):11–41.

Choi, S. M., Kim, W. H., Côté, D., Park, C. W., and Lee, H. (2011). Blood cell assisted in vivo Particle Image Velocimetry using the confocal laser scanning microscope. *Optics express*, 19(5):4357–4368.

Chu, V. H., Wu, J. H., and Khayat, R. E. (1991). Stability of transverse shear flows in shallow open channels. *Journal of Hydraulic Engineering*, 117(10):1370–1388.

Cohen, C. R. (2012). *Shallow-water plane and tidal jets*. PhD thesis, University of Otago.

Del Roure, F. N., Socolofsky, S. A., and Chang, K. A. (2009). Structure and evolution of tidal starting jet vortices at idealized barotropic inlets. *Journal of Geophysical Research: Oceans*, 114(C5).

Dietz, J. W. (1969). Kolkbildung in feinen oder leichten Sohl-materialien bei strömenem Abfluβ, Mitteilungen. *Mitteilungen des Theodor-Rehbock-Fiußbaulaboratoriums der Universität Karlsruhe*. Heft 155.

Dracos, T. H., Giger, M., and Jirka, G. H. (1992). Plane turbulent jets in a bounded fluid layer. *Journal of Fluid Mechanics*, 241:587–614.

Google Maps (2018). Google maps. Retrieved 2018-06-20, from `https://www.google.nl/maps/@51.6514969,3.7191162,3465m/data=!3m1!1e3`.

Guan, D., Melville, B. W., and Friedrich, H. (2013). Flow patterns and turbulence structures in a scour hole downstream of a submerged weir. *Journal of Hydraulic Engineering*, 140(1):68–76.

Hoffmans, G. J. C. M. and Booij, R. (1993). Two-dimensional mathematical modelling of local-scour holes. *Journal of Hydraulic Research*, 31(5):615–634.

Hoffmans, G. J. C. M. and Verheij, H. J. (1997). *Scour Manual*, volume 96. CRC press.

Huang, H., Dabiri, D., and Gharib, M. (1997). On errors of digital particle image velocimetry. *Measurement Science and Technology*, 8(12):1427.

Ingram, R. G. and Chu, V. H. (1987). Flow around islands in Rupert Bay: An investigation of the bottom friction effect. *Journal of Geophysical Research: Oceans*, 92(C13):14521–14533.

Jirka, G. H. (2001). Large scale flow structures and mixing processes in shallow flows. *Journal of Hydraulic Research*, 39(6):567–573.

Jirka, G. H. and Uijttewaal, W. S. J. (2004). Shallow flows: a definition. *Shallow flows*, pages 3–11.

Kantoush, S. A. and Schleiss, A. J. (2009). Large-scale piv surface flow measurements in shallow basins with different geometries. *Journal of Visualization*, 12(4):361–373.

Koopmans, H. (2017). Scour holes in tidal rivers with heterogeneous subsoil under anthropogenic influence. Master's thesis, Delft University of Technology.

Lane, S. N., Biron, P. M., Bradbrook, K. F., Butler, J. B., Chandler, J. H., Crowell, M. D., McLelland, S. J., Richards, K. S., and Roy, A. G. (1998). Three-dimensional measurement of river channel flow processes using acoustic doppler velocimetry. *Earth Surface Processes and Landforms: The Journal of the British Geomorphological Group*, 23(13):1247–1267.

Nienhuis, P. H. and Smaal, A. C. (1994). The oosterschelde estuary, a case-study of a changing ecosystem: an introduction. *Hydrobiologia*, 282(1):1–14.

Pearson, R. K. (2005). *Mining imperfect data: Dealing with contamination and incomplete records*, volume 93. Siam.

Pietrzak, J. (2015). *An Introduction to Oceanography for Civil and Offshore Engineers*. Delft University of Technology. Reader of the course CIE5317 Physical Oceanography.

Schiereck, G. J. (2003). *Introduction to bed, bank and shore protection*. CRC Press.

Simpson, R. L. (1989). Turbulent boundary-layer separation. *Annual Review of Fluid Mechanics*, 21(1):205–232.

Smaal, A. C. and Nienhuis, P. H. (1992). The eastern scheldt (the netherlands), from an estuary to a tidal bay: a review of responses at the ecosystem level. *Netherlands Journal of Sea Research*, 30:161–173.

Soulsby, R. L. (1981). Measurements of the reynolds stress components close to a marine sand bank. *Marine Geology*, 42(1-4):35–47.

Steenepoorte, K. (2016). De stormvloedkering in de oosterschelde. Technical report, Rijkswaterstaat.

Stenfert, J. G. (2017). Scour holes in heterogeneous subsoil. Master's thesis, Delft University of Technology.

Stoutjesdijk, T., de Kleine, M., de Ronde, J., and Raaijmakers, T. (2012). Stormvloedkering Oosterschelde: ontwikkeling ontgrondingskuilen en stabiliteit bodembescherming, Hoofdrapport. Technical report, Deltares.

Talstra, H. (2011). *Large-scale turbulence structures in shallow separating flows*. PhD thesis, Delft University of Technology.

Thielicke, W. and Stamhuis, E. J. (2014). PIVlab - Time-resolved digital particle image velocimetry tool for MATLAB.

Uijttewaal, W. S. J. (2018). *Turbulence in hydraulics*. Delft University of Technology. Reader of the course CT5312 Turbulence in Hydraulics.

Uijttewaal, W. S. J., Huismans, Y., and Koopmans, H. (2016). A scaled experimental pilot-study on deep scour holes in river beds of heterogeneous composition. Technical report, Delft University of Technology and Deltares.

Uijttewaal, W. S. J. and Jirka, G. H. (2003). Grid turbulence in shallow flows. *Journal of Fluid Mechanics*, 489:325–344.

van der Meulen, T. and Vinjé, J. J. (1975). Three-dimensional local scour in non-cohesive sediments. *16th IAHR-congress*.

van Dyke, M. (1982). *An album of fluid motion*. Parabolic Press Stanford.

van Noortwijk, J. M. and Klatter, H. E. (1999). Optimal inspection decisions for the block mats of the Eastern-Scheldt barrier. *Reliability Engineering & System Safety*, 65(3):203–211.

Van Prooijen, B. C. (2004). *Shallow Mixing Layers*. PhD thesis, Delft University of Technology.

van Prooijen, B. C. and Uijttewaal, W. S. J. (2002). A linear approach for the evolution of coherent structures in shallow mixing layers. *Physics of Fluids*, 14(12):4105–4114.

van Velzen, G., Raaijmakers, T. C., and Hoffmans, G. J. C. M. (2015). Scour development around the Eastern Scheldt storm surge barrier-field measurements and model predictions. *Proceedings of the 7th International Conference on Scour and Erosion*, pages 693–704.

van Zuylen, J. A. (2016). Development of scour in non-cohesive sediment under a poorly erodible top layer. Master's thesis, Delft University of Technology.

Vassalos, D. (1998). Physical modelling and similitude of marine structures. *Ocean engineering*, 26(2):111–123.

Vermeulen, B., Hoitink, A. J. F., and Labeur, R. J. (2015). Flow structure caused by a local cross-sectional area increase and curvature in a sharp river bend. *Journal of Geophysical Research: Earth Surface*, 120(9):1771–1783.

Visser, T. (1991). Ontwerpnota Stormvloedkering Oosterschelde, Boek 2: De waterbouwkundige werken. Technical report, Rijkswaterstaat, Deltadienst.

Visser, Y. (2013). Watersnoodramp (1953) – Een rampzalige stormvloed. Retrieved 2017-11-15, from `https://historiek.net/watersnoodramp-1953/6913/`.

VVV Zeeland (2018). Oosterscheldekering. Retrieved 2018-03-08, from `https://www.vvvzeeland.nl/nl/zien-en-doen/top-10-zien-en-doen/`.

Weitbrecht, V., Kühn, G., and Jirka, G. H. (2002). Large scale PIV-measurements at the surface of shallow water flows. *Flow Measurement and Instrumentation*, 13(5):237–245.

Wells, M. G. and van Heijst, G. J. F. (2003). A model of tidal flushing of an estuary by dipole formation. *Dynamics of Atmospheres and Oceans*, 37(3):223–244.

Westerweel, J. and Scarano, F. (2005). Universal outlier detection for piv data. *Experiments in fluids*, 39(6):1096–1100.

Wikipedia (2011). North Sea flood of 1953. Retrieved 2017-11-15, from `https://en.wikipedia.org/wiki/North_Sea_flood_of_1953`.

Winant, C. D. and Browand, F. K. (1974). Vortex pairing: the mechanism of turbulent mixing-layer growth at moderate reynolds number. *Journal of Fluid Mechanics*, 63(2):237–255.

A

Experimental setup

This appendix discusses and illustrates the experimental setup in more detail. Several photographs are included to give an impression of the performed PIV and ADV measurement techniques.

A.1. The shallow wide flume

The physical experiments were conducted in the wide shallow flume of the Environmental Fluid Mechanics Laboratory at Delft University of Technology. The flume has a length of 19.2 m, an effective length of 19.2 m and a height of 20.0 cm. The discharge in the flume is regulated by three valves of which two are located near the inlet section. Furthermore, the discharge was measured by a *Proline Prosonic 91W* flowmeter. A weir at the downstream end of the flume was operated to adjust the outflow boundary condition. Figure A.1 depicts the main valve, the *Proline Prosonic 91W* flowmeter and the adjustable weir.

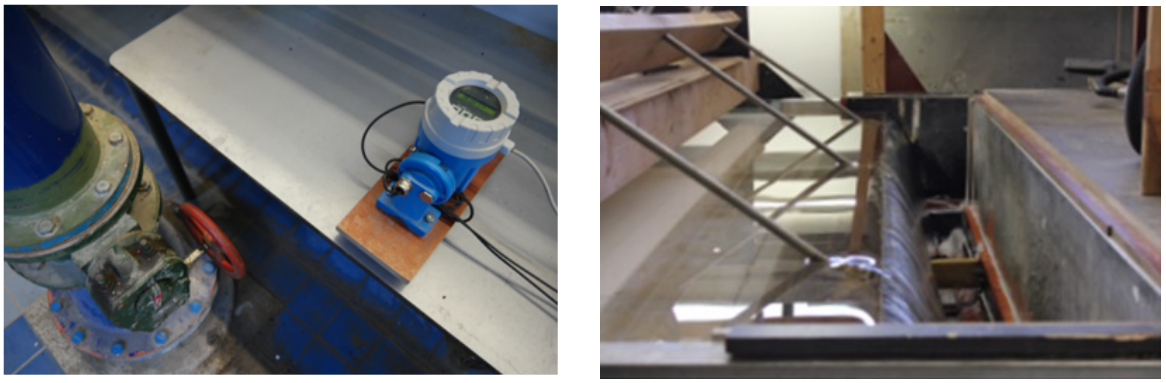

(a) (b)

Figure A.1: Means to regulate the flow in the flume: (a) The main valve to set the discharge and the Proline Prosonic 91W flowmeter and (b) The weir at the downstream side of the flume used to adjust the outflow boundary condition.

A.2. Details of the experimental setup

Directly downstream of the inlet section a honeycomb was installed to ensure that the incoming streamlines were more or less straight. Load blocks were placed on top of the honeycomb grating to prevent it from moving. Additionally, a foam board was used to damp surface waves that were issued from the inlet section. Figure A.2 depicts the inlet section including the honeycomb and the foam board.

Figure A.2: Honeycomb and foam board to damp disturbances issued from the inlet section.

A laser mounted on a wooden frame was installed on the left glass side wall to measure to water depth in the flume. The laser was located approximately 3 m upstream of the weir. As the laser would not reflect on the water surface, a piece of floating white tape that was used to measure the water level. The equipment to measure water level is depicted in Figure A.3. During the experiments, a constant water level of 16.0 cm was maintained downstream of the downward slope.

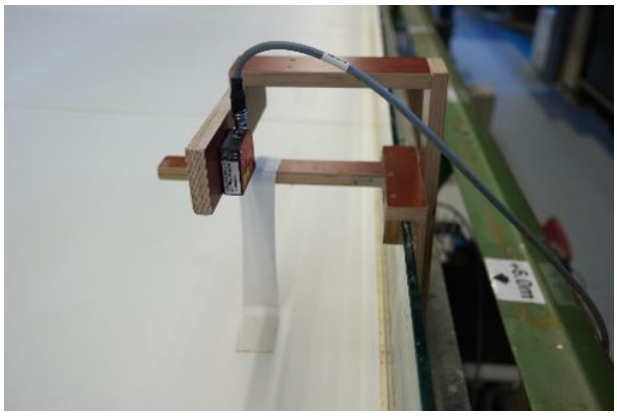

Figure A.3: Laser to measure the downstream water depth.

Figure A.4 depicts the false bottom, contracting elements and the grid that were used in the experimental setup.

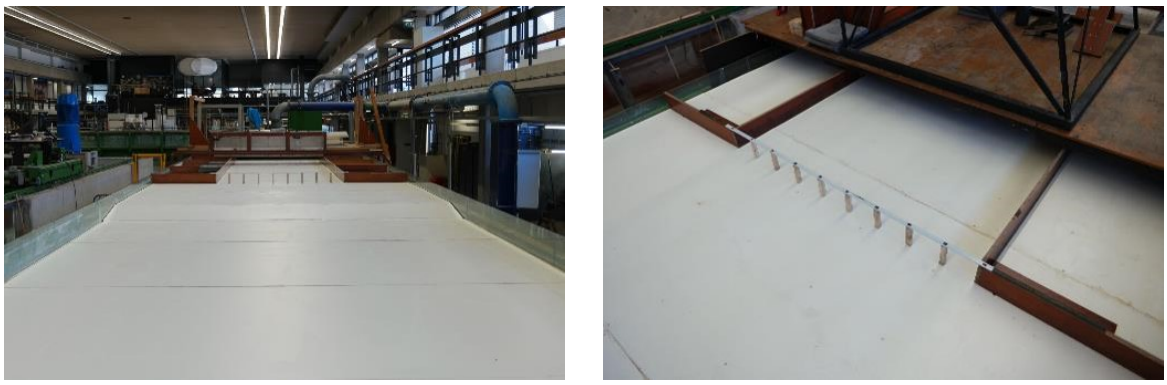

(a) (b)

Figure A.4: Overview of the experimental setup in the shallow flume: (a) The false bottom and (b) The contracting elements and grid.

A.3. PIV measurements

This section presents additional information on the setup that was used for the PIV measurements.

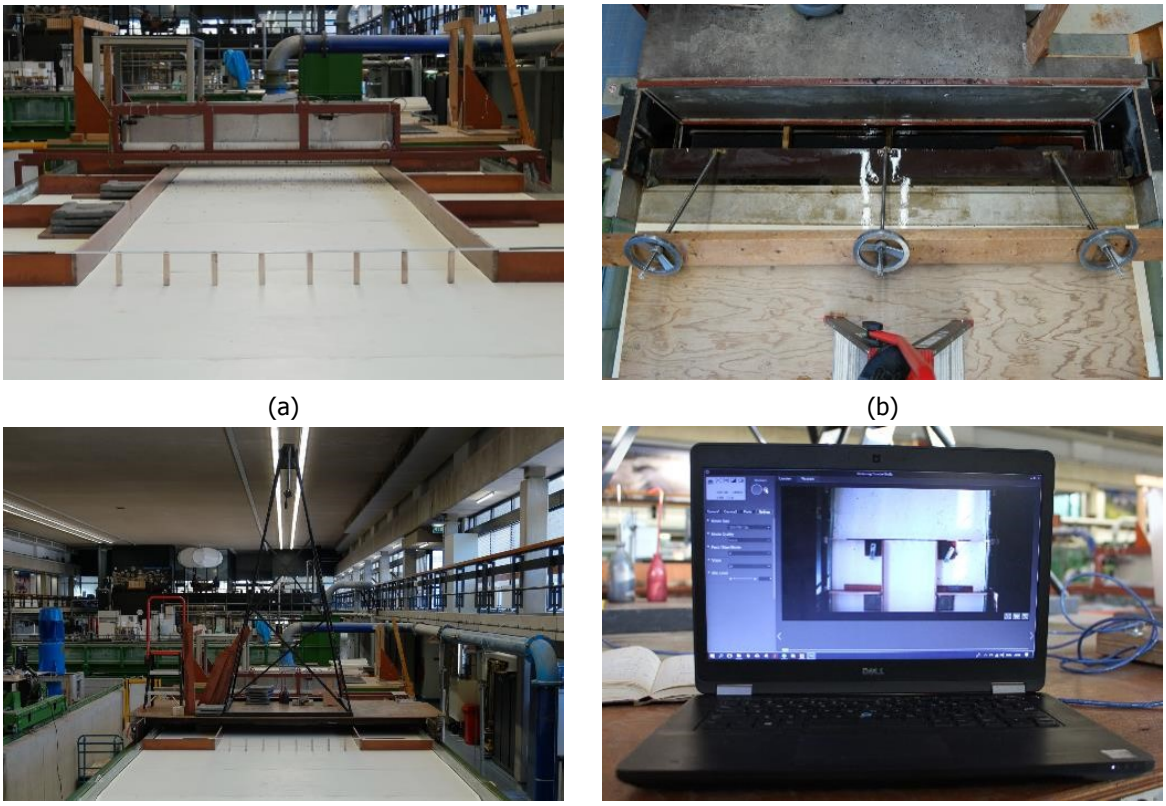

(a) (b)

(c) (d)

Figure A.5: Experimental setup of the PIV measurements: (a) The particle dispenser, (b) The outflow section with grating to recover the tracer particles, (c) The camera frame and (d) Tethered shooting with Canon EOS Utility.

A.4. ADV measurements

This section presents additional information on the setup that was used for the ADV measurements.

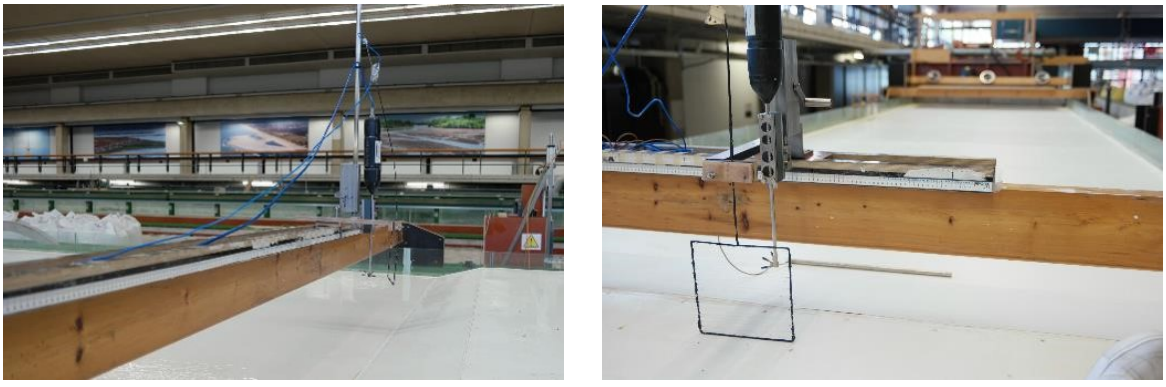

(a) (b)

Figure A.6: Experimental setup for the ADV measurements: (a) Wooden beam positioned over the width of the flume equipped with measurement and (b) The *Vectrino 2D-3D Sidelooking*, the wire mesh and metal bar.

A.5. Inaccuracies in the experimental setup

Inaccuracies in the experimental setup mainly follow from deformation of the material that was used to construct the experimental geometry. The following aspects were found that could have influenced the measurement results:

1. Deviations in the flatness of the false bottom
2. Deformation of the wooden boxes on top of the false bottom

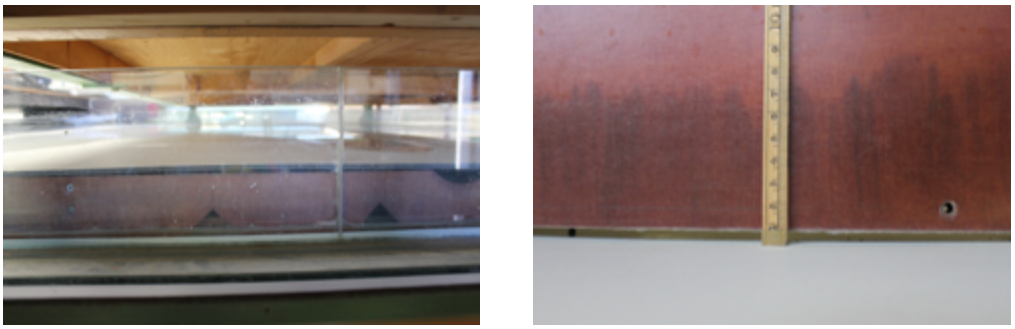

(a) (b)

Figure A.7: Deformation of the experimental geometry: (a) Bulging of the HPL plates which were used to construct the false bottom and (b) deformation of the wooden construction that formed the lateral expansion.

3. Expansion of the sealant downstream of the false bottom

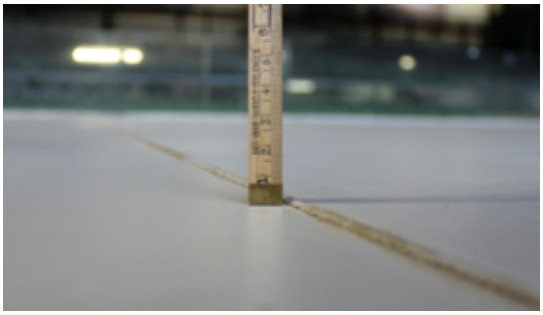

Figure A.8: Expansion of the sealant downstream of the downward slope.

4. Setting the downstream boundary condition

Figure A.9: Inaccuracies in setting the downstream boundary condition.

B

Preliminary experiments

Prior to the experiments with the setup as discussed in the main report, experiments were conducted with triangular geometries to contract the flow. These experiments included setups with one or two triangles and a 1:4 downward slope. Also, various discharges were tried to investigate the influence on the smoothness of the water surface.

This appendix discusses the observations that were made during the preliminary experiments. Observations of the flow field follow from visualisation by dye injection and particle seeding. No quantitative measurements were performed during the preliminary experiments. Table B.1 states geometry and flow properties that were used.

Name	Contraction type	Location [m]	Discharge [m^3/s]	Fr [-]	Re [-]
Run 1.2.1	Single triangle	0.0	65	0.56	3.25×10^4
Run 1.2.2	Single triangle	-1.0	65	0.56	3.25×10^4
Run 1.2.3	Single triangle	-2.0	50	0.39	2.50×10^4
Run 1.2.4	Single triangle	-3.0	50	0.39	2.50×10^4
Run 1.3.1	Two triangles	0.0	50	0.59	3.33×10^4
Run 1.3.2	Two triangles	-1.0	50	0.59	3.33×10^4
Run 1.3.3	Two triangles	-2.0	50	0.59	3.33×10^4
Run 1.3.4	Two triangles	-3.0	50	0.59	3.33×10^4

Table B.1: Description of the preliminary experiments

B.1. Flow contraction by a single triangle

In line with the work of Broekema (2017a) experiments started with a single triangle to contract the flow. The motivation to use only a single triangle to contract the flow follows from idea to utilise the line of symmetry in the experimental setup. It is thereby assumed that the glass side wall on the opposite side of the contraction has a negligible effect on the flow. The advantage of using the line of symmetry is that the entire width of the flume can be used for measurements compared to only half of the flume in the case of two triangles. (Note: for an experimental setup with two triangles it was expected that the flow field would also be symmetric and measurement would only be required in one half of the flume.)

The triangle that was used for these experiments had a length of 4 m and a maximum width of 1 m. The discharge cross-sectional area on the vertical step was therefore reduced by 33 %. The 1:4 slope of the triangle was steeper compared to the contraction used in the experiments of Broekema (2017a). The steeper slope was chosen in a trade-off between the length of the contraction and downstream distance available for measurements. Using a steeper slope for the contraction resulted in presence of

a larger lateral velocity component in the flow.

The following observations were made during the preliminary experiments with a single triangle to contract the flow:

1. *Vertical flow separation at the downward slope.* All runs with a single triangle resulted in the separation of the jet flow at the downward slope. This was concluded from both dye injection and seeding of sinking tracer particles. Only at the location were the lateral velocity gradient was the largest, that is in the mixing layer, it was observed that the flow remained attached to the downward slope. Also, it was observed that the vertical recirculation cell on downward slope contained a lateral velocity component. In Figure B.1 it can be seen that the dye is transported along the toe of the slope in the direction away from the contraction.

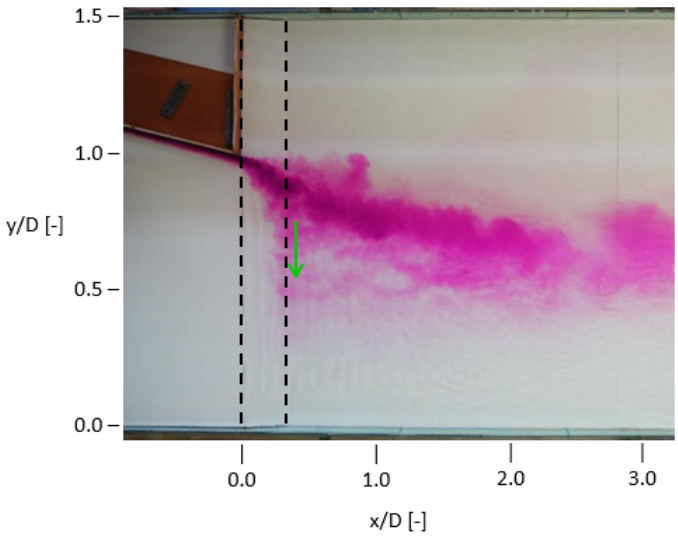

Figure B.1: Lateral velocity component in the vertical recirculation cell on the downward slope indicated by the green arrow. The black dashed lines show the location of the downward slope. The flow is directed from left to right. (Run 1.2.1)

2. *Flow contraction at the downward slope.* It was found that the jet flow is contracted at the location of the downward slope. In Figure B.2 it can be seen that the flow downstream of the contraction initially follows a line extending from the slope of the contraction. Then, at the upstream end of the downward slope, the jet flow experiences a lateral acceleration directed away from the contraction. Dye injection clearly demonstrated that the eddies that are formed in the mixing layer between the jet flow and the large-scale gyre are deflected toward the high-velocity side.

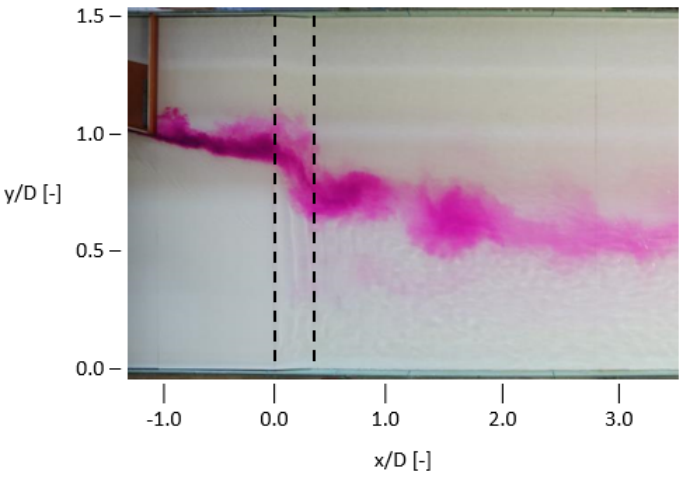

Figure B.2: Flow contraction above the downward slope. (Run 1.2.2)

3. *Large-scale horizontal recirculation zone.* Downstream of the contraction a large-scale recirculation formed that included a primary and secondary gyre. In all runs the reattachment point of the mixing layer was located approximately 1 m upstream of the weir. The location of the secondary separation point, on the other hand, varied for each run.
4. *Mixing layer along the glass side wall.* As observed in Run 1.1.1, Run 1.1.2 and Run 1.1.3 the experimental runs with a single triangle all showed the presence of a mixing layer along the glass wall opposite to the contraction, see Figure B.3. The assumption that this glass side wall had a negligible effect on the flow did therefore not hold. It was concluded that an experimental setup based on a line of symmetry was not fit for experimental runs in the shallow flume.

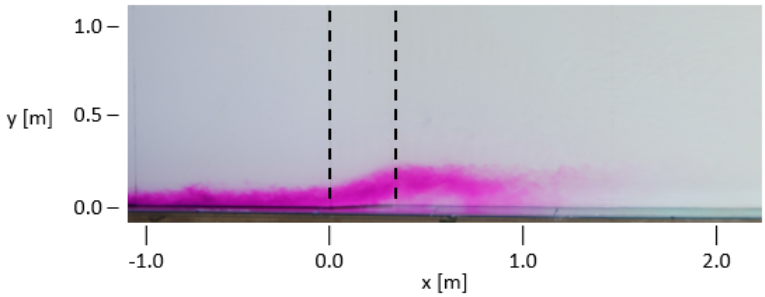

Figure B.3: Mixing layer along the glass side wall opposite to the contraction. (Run 1.2.3)

5. *Standing surface waves.* During Run 1.2.1 and Run 1.2.2 standing surface waves were observed at the location where the jet flow approached of the downward slope, as depicted in Figure B.4. To reduce the influence of the surface waves it was decided to decrease the discharge after Run 1.2.2 from 65 m^3/s to 50 m^3/s. This resulted in standing surface waves with a smaller amplitude that were expected to be of minor influence on the flow pattern.

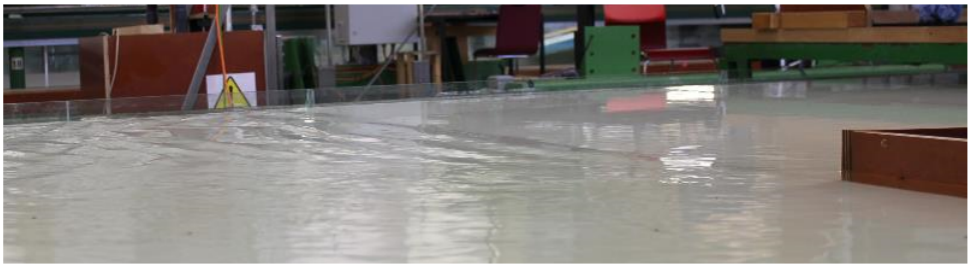

Figure B.4: Standing surface waves above the downward slope. Flow direction is from right to left. (Run 1.2.1)

6. *Growth of eddies.* Increasing the distance from the downward slope to the contraction led to larger counterclockwise rotating eddies in mixing layer between the jet flow and the large-scale recirculation zone. Furthermore, it was observed that during Run 1.2.3 and Run 1.2.4 occasionally vortex merging occurred (Figure B.5).

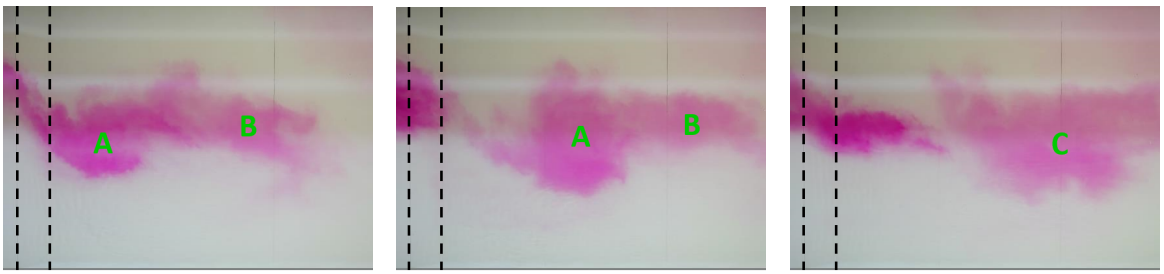

Figure B.5: Vortex merging of eddies A and B into C. Photo series with an interval of 5 seconds. (Run 1.2.4)

B.2. Flow contraction by two triangles

As the experimental runs with a single triangle did not result in the expected flow pattern it was decided to continue with a setup that contained two triangles to contract the flow. The triangles that were used had a length of 4 m and a width of 0.75 m. The discharge cross-sectional at the maximum point of contraction was thereby reduced to 50 % of the initial width. Lateral velocities at the downstream end of the contraction were smaller compared to experiment with a single triangle as the slope of the triangles was reduced to 1:5.33 .

The following hydrodynamic processes were observed during experimental runs with two triangles:

1. *Vertical flow separation.* As well as for the experiments with a single triangle, all runs with two triangles to contract the flow resulted in vertical flow separation at the location of the downward slope. Again, a lateral component was present in the vertical recirculation zone that had formed on the downward slope. This time, however, the lateral component was directed towards the central axis of the flume. In Figure B.6 it can be seen that the dye injected along the contraction is transported along the downward slope.

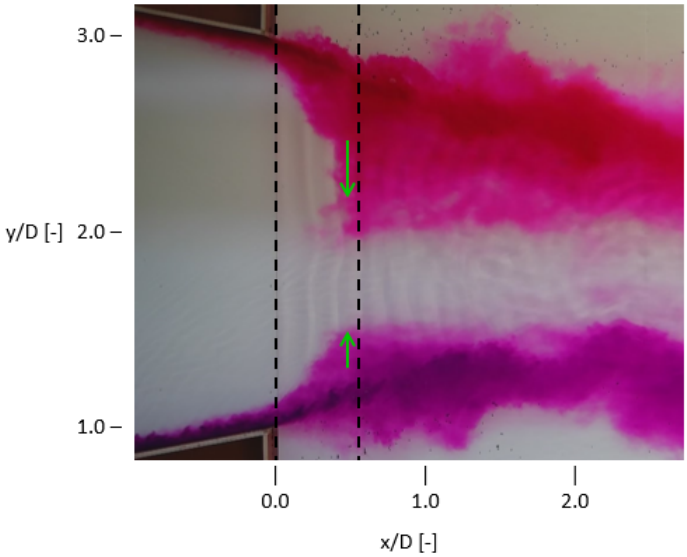

Figure B.6: The presence of a lateral component in the vertical recirculation zone on the downwards slope. (Run 1.3.1)

2. *Flow contraction at the downward slope.* Similarly to the experiments with one triangle, it was found that for this setup the jet flow contracted at the location of the downward slope. Even though the flow contained a lateral velocity component due to the geometry of the contraction, it was observed that the jet was further squeezed above the downward slope. Furthermore, eddies in the horizontal mixing layers downstream of the triangles were again deflected to the high-velocity side.

3. *Asymmetric flow pattern.* Although in this case the experimental setup was symmetric, the jet flow deflected towards one of the flume's glass side walls during each run (Figure B.7). Switching the pump of and on again could change the direction of the jet towards the other glass side wall. It was therefore assumed that the deflection of the jet flow was determined by subtle pressure differences.

4. *Horizontal recirculation zones.* Downstream of each triangle a horizontal recirculation zone formed that contained a primary and secondary gyre. The horizontal recirculation zones were unequal in size due to the deflection of the jet. The largest recirculation zone, or the dominant gyre, extended to approximately 1 m upstream of the weir. The exact location of the reattachment point of the non-dominant gyre varied for each run.

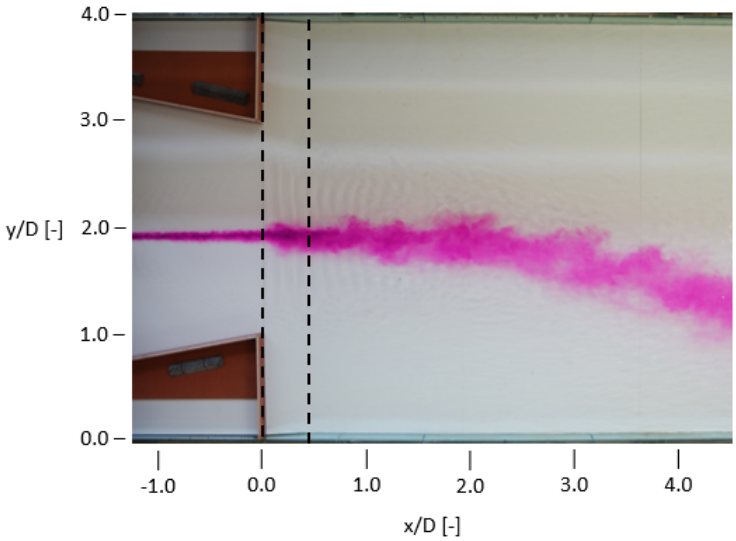

Figure B.7: Asymmetric basin flow. (Run 1.3.1)

5. *Growth of eddies.* Figure B.8 depicts the growth of eddies in the mixing layer between the jet flow and the dominant gyre for Run 1.3.2. The main difference between the eddies in the horizontal mixing layers downstream of the triangles is the direction of rotation. For this experimental setup vortex merging was not recorded on video. It is however very likely that this processes did occur.

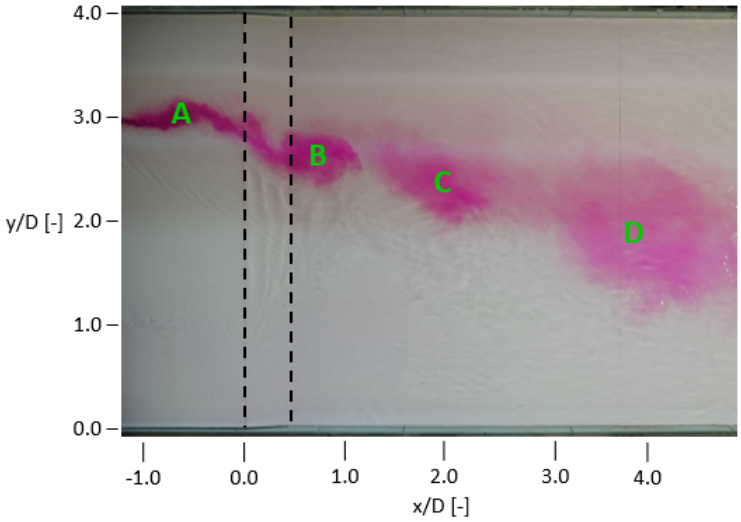

Figure B.8: Eddie growth in the mixing layer between the jet flow and the dominant gyre. (Run 1.3.2)

C

PIV measurements

C.1. General information

Particle image velocimetry (PIV) is a technique in which a set of images, taken at a constant time interval and from a fixed point of view, is used to determine the spatial displacement of so-called tracers. The tracers follow the motion of the considered fluid and can, therefore, be used to determine the local flow velocity. The PIV method enables the user to measure the mean flow conditions, turbulent flow characteristics and makes it possible to track large 2DCS in shallow water flows (Weitbrecht et al., 2002). The main steps in a PIV analysis are image pre-processing, image evaluation and post-processing.

PIV makes use of various small sub-images known as interrogation areas or interrogation windows to determine the surface velocity, see Figure C.1. The interrogations areas in consecutive pairs of images are spatially cross-correlated with a PIV algorithm. The PIV algorithm derives the most probable displacement for the group of tracers in an interrogation area and gives forth its associated velocity vector. The main advantage of PIV is that the flow field can be described by a structured set of vectors, rather than by a set of non-homogeneous distributed velocity vectors for all individual tracer particle.

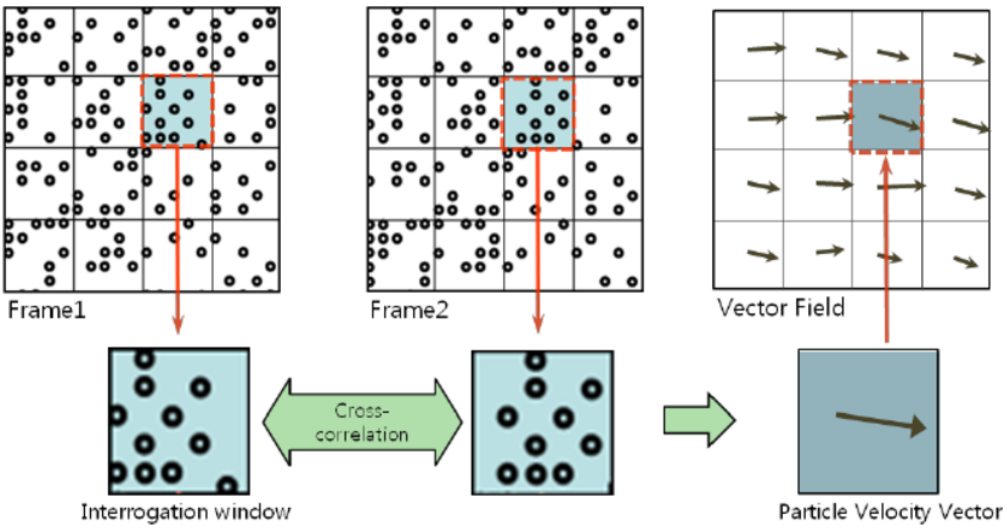

Figure C.1: The concept of cross-correlation used in PIV (Choi et al., 2011).

C.2. Correction for lens distortion

To investigate the effect of the lens distortion of the camera a calibration video with a checkerboard was recorded. In this calibration video, the checkerboard was moved through the plane of interest, i.e. the height corresponding to the water surface in the experiments. From this calibration video 18 images were extracted that were used to determine the correction for the lens distortion. The application *Camera Calibration* of MATLAB was then used to compute the corrected images. Figure C.2 depicts the lens correction for one of the calibration images. It can be seen that distorted and corrected images are nearly identical.

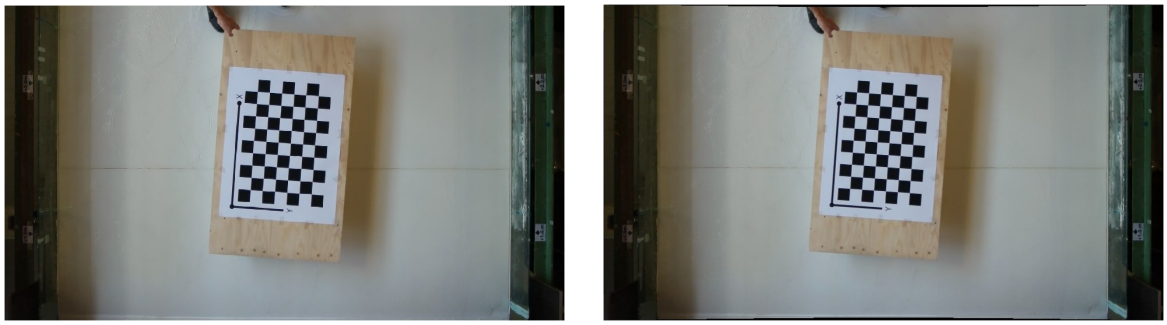

(a) (b)

Figure C.2: Correction for distortion of the camera lens. (a) Distorted image and (b) Corrected image. The small back areas at the sides of the corrected image show that the lens distortion is nearly negligible.

C.3. Data post-processing

Figure C.3 shows an example of the post-processing of the PIV data.

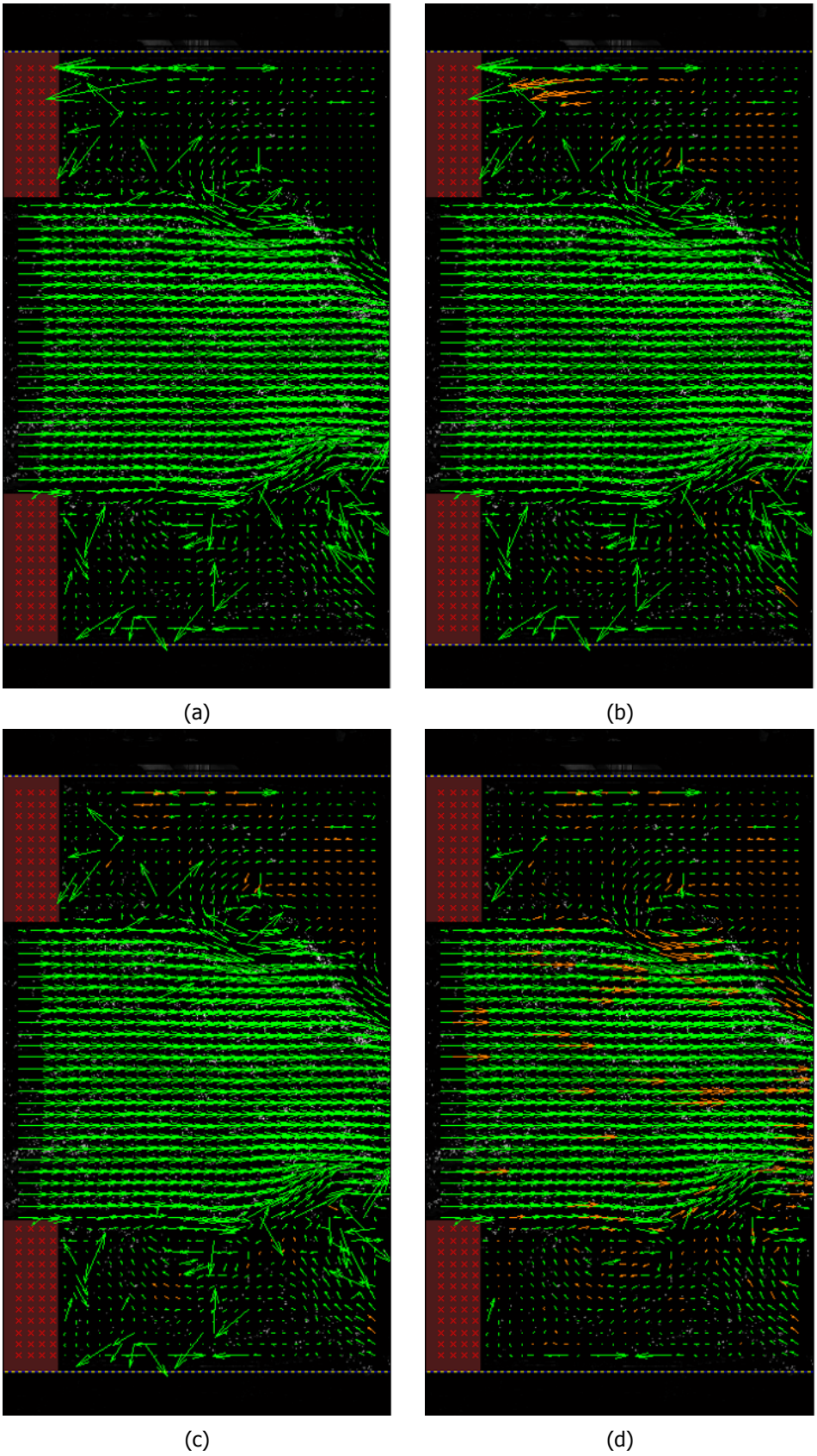

Figure C.3: Data post-processing steps: (a) Velocity vectors obtained from the PIV analysis including missing data points, (b) Two-dimensional interpolation of the missing data points, (c) First filter based on velocity thresholds and (d) Second filter based on the normalised median test (Westerweel and Scarano, 2005). The orange vectors indicate the data points that were adjusted and interpolated in each step.

D

Results

This appendix presents additional comparisons of estimations for the bed shear stresses to support the findings in section 4.4. Two additional comparisons between experiments with vertical flow separation and attachment are given in Figure D.1 and Figure D.2. Furthermore, extra comparisons of the influence of grid turbulence are shown in Figure D.3 and Figure D.4.

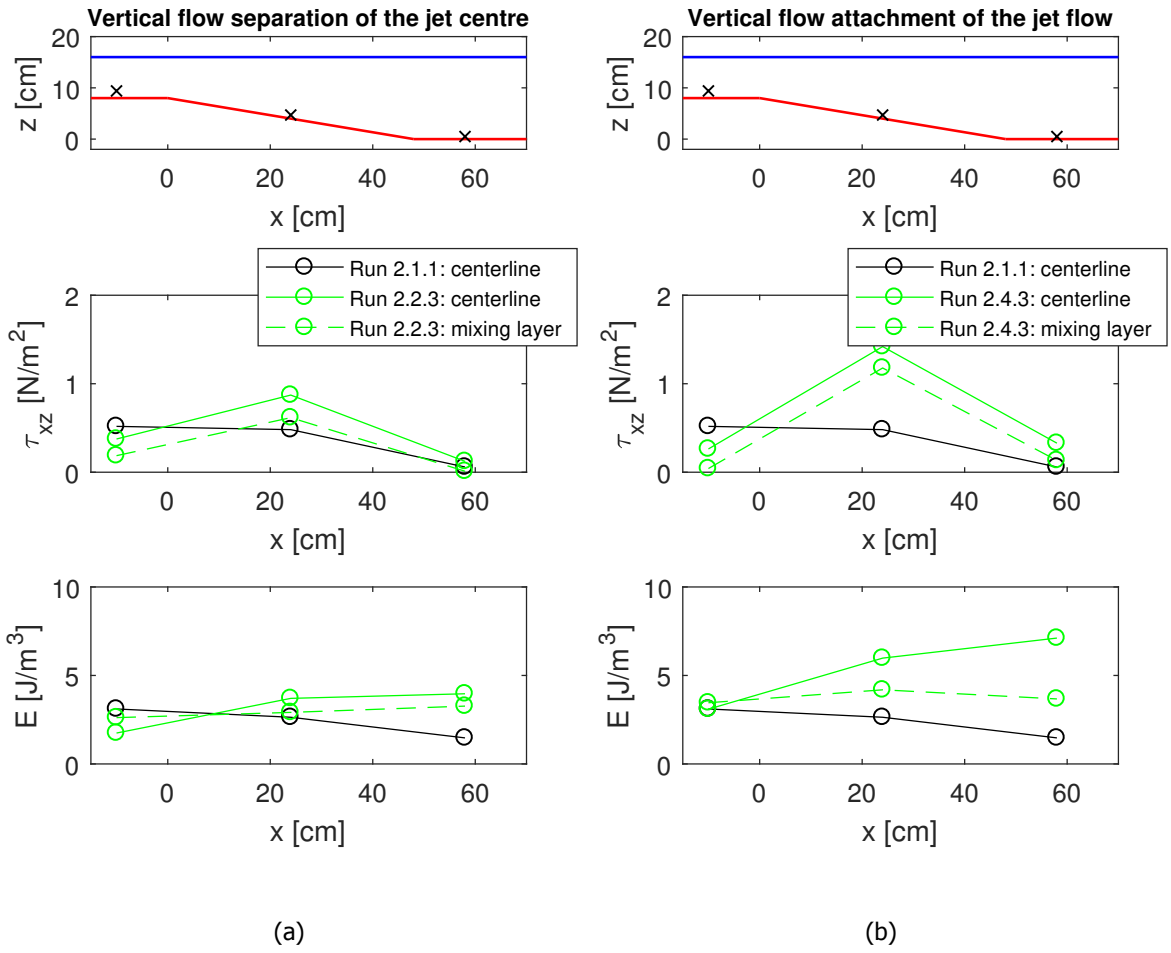

Figure D.1: The Reynolds stress τ_{xz} and the TKE for experimental runs representative for vertical flow separation of the jet centre and vertical flow attachment of the jet flow. (a) Vertical flow separation (Run 2.2.3: slope 1:6, B1=1.5 m, $L_{b,m}$=2.0 m and no grid). (b) Vertical flow attachment (Run 2.4.3: slope 1:6, B1=1.0 m, $L_{b,m}$=2.0 m and no grid).

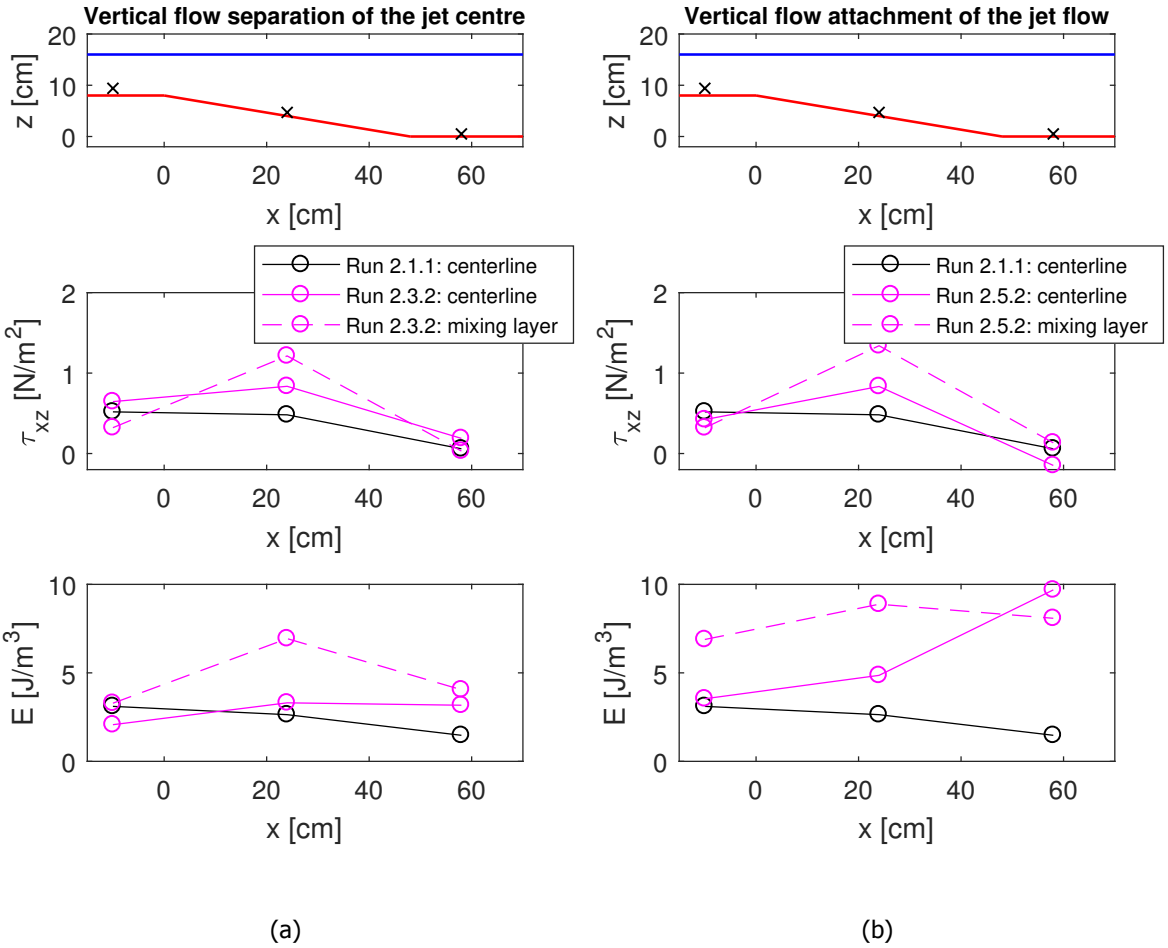

Figure D.2: The Reynolds stress τ_{xz} and the TKE for experimental runs representative for vertical flow separation of the jet centre and vertical flow attachment of the jet flow. (a) Vertical flow separation (Run 2.3.2: slope 1:6 , B1=1.5 m, $L_{b,m}$=2.0 m and with grid). (b) Vertical flow attachment (Run 2.5.2: slope 1:6 , B1=1.0 m, $L_{b,m}$=2.0 m and with grid).

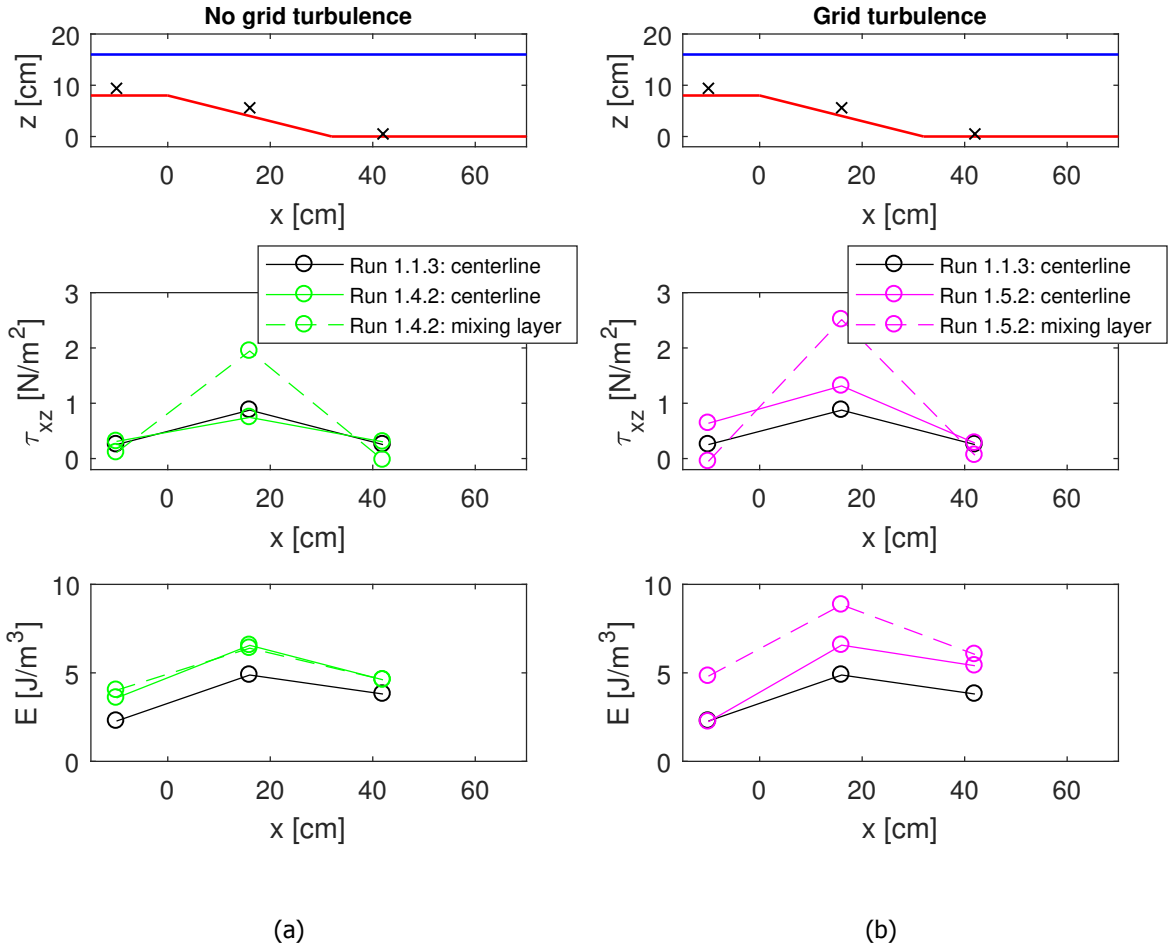

Figure D.3: Comparison of the Reynolds stress τ_{xz} and the TKE for experimental runs with and without grid turbulence. (a) Experimental run without the effect of grid turbulence (Run 1.4.2: slope 1:4 , B1=1.5 m, $L_{b,m}$=1.0 m and no grid). (b) Experimental run including grid turbulence (Run 1.5.2: slope 1:4 , B1=1.5 m, $L_{b,m}$=1.0 m and with grid).

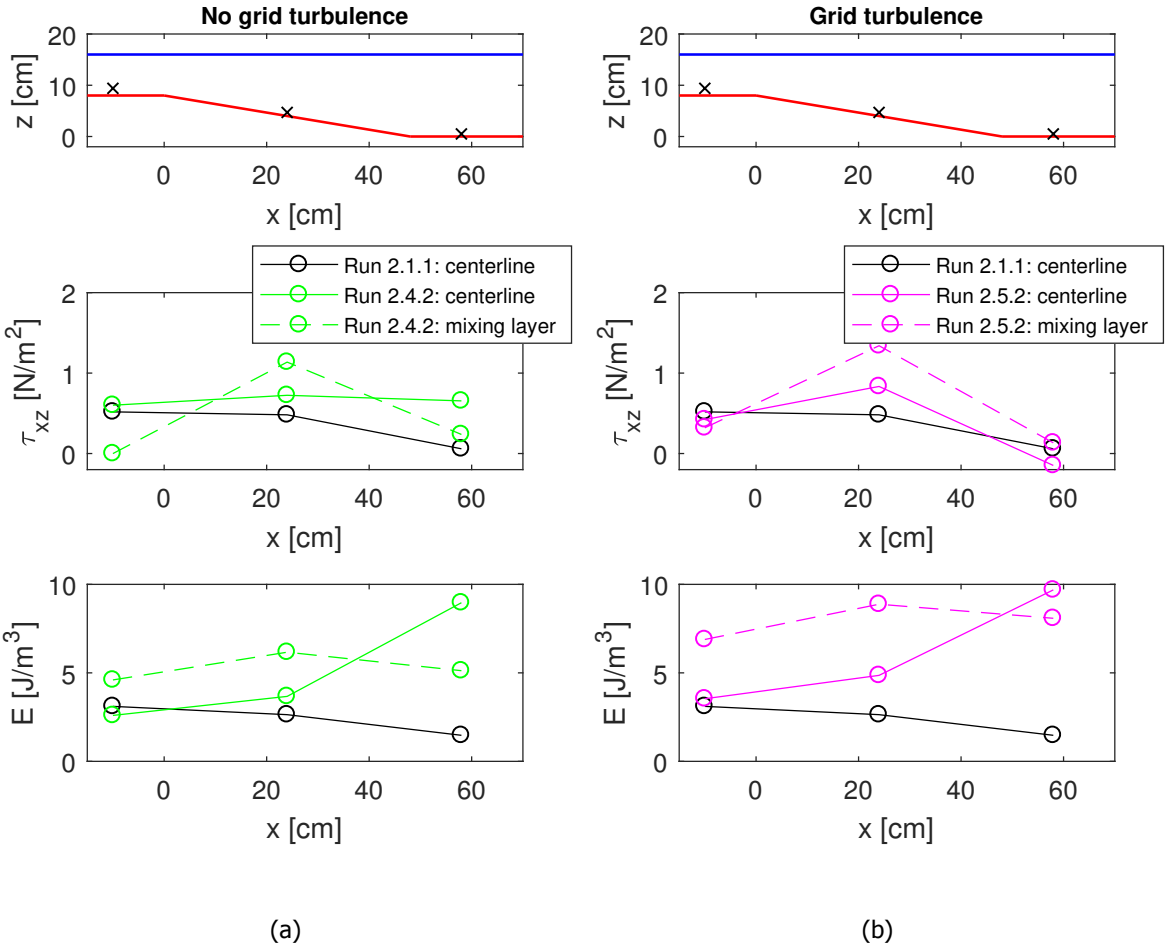

Figure D.4: Comparison of the Reynolds stress τ_{xz} and the TKE for experimental runs with and without grid turbulence. (a) Experimental run without the effect of grid turbulence (Run 2.4.2: slope 1:6 , B1=1.0 m, $L_{b,m}$=1.0 m and no grid). (b) Experimental run including grid turbulence (Run 2.5.2: slope 1:6 , B1=1.0 m, $L_{b,m}$=1.0 m and with grid).